Development of an Analytical Model for a Fiber Optic Evanescent Wave Sensor

by

Jeremy Robert Godin

A thesis
presented to the University of Waterloo
in fulfillment of the
thesis requirement for the degree of
Doctor of Philosophy
in
Mechanical Engineering (Nanotechnology)

Waterloo, Ontario, Canada, 2015

AUTHOR'S DECLARATION

I hereby declare that I am the sole author of this thesis. This is a true copy of the thesis, including any required final revisions, as accepted by my examiners.

I understand that my thesis may be made electronically available to the public.

Abstract

Spectroscopy in the near infrared range is a powerful tool for the qualitative and quantitative analysis of a variety of materials in the gas liquid or solid phases. The use of optical fibers as a means of performing cost effective in-situ spectroscopic analysis has gained a lot of attention in many fields in the past three decades. Intensity based fiber optic sensors, which rely on variations in transmission power at a fixed wavelength for the characterization of material, are relatively inexpensive to fabricate and provide an easy to read signal.

The objective of this thesis will be to present an analytical model developed for a multimode fiber optic evanescent wave sensor (FOEWS) capable of monitoring the charge cycle of a lithium-ion battery cell. The sensor is fabricated by partial removal of the cladding material surrounding the core of a multimode fiber optic. The thinned cladding section allows for transmission loss via evanescing waves which radiate power out from the core as a function of the external environment.

In contrast to FOEWS designs which use a single mode optical fiber, the use of a multimode fiber causes difficulty in numerical modeling of the system. Single mode optical fibers have core diameters which are small relative to the wavelength of light propagating within. As such, solving for the transmission response of a single mode fiber can be accomplished using a numerical solver. By using a multimode optical fiber the fiber core diameter is orders of magnitude larger than the wavelength of propagating light. Attempting to accurately mesh a multimode optical fiber requires an unmanageably large mesh which cannot be solved in a reasonable time frame. Alternative approaches for the modeling of a multimode FOEWS have been proposed in the past. However, these methods make use of effective attenuation coefficients to estimate the transmission coefficient of the sensor and thus, they do not include a direct analysis of the electromagnetic field solutions of the thin cladding region. An analytical method for accurately solving the attenuation coefficient using the transfer matrix method is presented. Adoption of the analytical method extends the theoretical description of FOEWS model allowing for more accurate prediction of the sensor behavior by directly accounting for cladding thickness without the use of empirically determined attenuation coefficients.

FOEWS fabricated using commercially available step index multimode fibers etched with buffered hydrofluoric acid were used to verify predictions of the newly modified model. Model predictions are matched with experimental tests performed using known index of refraction samples of glycerol and calibrated thermal optic oil ranging from 1.451 to 1.466. The experimentally observed intensity variations are compared to model predictions for verification. The fabricated FOEWS was determined to have a cladding thickness of $0.485 \pm 0.1\ \mu\mathrm{m}$. Comparison with direct measurement under scanning electron microscope (SEM) place the variations of the model from the experimental results within one standard deviation of the fabrication tolerances of the optical fiber.

Building on the increased capabilities of the transfer matrix method to analytically model the thin film reflection coefficient, a method is put forth to simulate the partial contact of a solid analyte with a FOEWS. A case study is presented which investigates the FOEWS response behavior to a solid lithium-ion graphite anode held in partial contact to the fiber. SEM images of lithium-ion anode materials held in sensing contact with a fabricated FOEWS are analyzed to determine the fractional contact area of the fiber optic sensing region with the solid anode. A statistical average of the fractional contact area as well as mean depth of non-contact regions is determined. The presence of partial contact between the fiber thin cladding and anode material creates a fourth thin film region which is filled with electrolyte liquid from the cell. The addition of a fourth thin film region is added to the transfer matrix method analysis of the sensing region of the FOEWS to account for the presence of liquid electrolyte between the fiber sensing region and anode bed. By splitting the model analysis of the sensing region into two separate sections representing the fractional full and fractional partial contact regions effects of partial is then studied using simulated results.

In summary, the ability to directly model thin film cladding effects using the transfer matrix method has been added to pre-existing FOEWS models. This new functionality is tested against fabricated devices using solutions of various index of refraction. The model is then used to predict the effect of partial contact of the sensor with a solid anode analyte from a lithium-ion cell.

Acknowledgements

I would like to thank my advisor Prof. Patricia Nieva, for her continuous support throughout my Ph.D. Her guidance helped bring this work to fruition. Additionally, I would like to thank the rest of my thesis committee: Prof. Amir Khajepour, Prof. Ehsan Toyserkani, and Prof. Simarjeet Saini for their insightful comments and encouragements, as well as Prof. Nick Jaeger who graciously agreed to be my external examiner.

I would like to acknowledge the funding and financial support provided to me by the Ontario Research fund (ORF), and the Auto Partnership of Canada (APC).

I am grateful to my fellow colleagues within the SimsLab group: Dr. Ali Najafi Sohi, Dr. Ryan Norris, Abdul Rahman Ghannoum, Liliana Zdravkova, and Ryan Denomme, for the many supportive conversations and coffee breaks over the past five years. I am also grateful to Prof. Ariel Edery who first introduced me to the world of research. Also I wish to thank my friends: Dr. John Dick, Soheil Barakat, Harding Nelson, and Peter Kraska, as well as soon to be Drs. Stephen McManus, and Saeid Khosravani and my sister, Jessica Godin, who all provided me with the encouragement and support that made this work possible. A special thanks goes to Amanda Piribauer who stood by me during the long five year pursuit of this endeavor, and whose love and support knew no bounds.

Finally, I would like to thank my parents Dr. Robert, and Lynda Godin who have always encouraged me to pursue my goals.

Dedication

This thesis is dedicated to my mother *Lynda Godin* for her endless love and self-sacrifice without which I would never stand here, and to my everlasting hero, my father, *Dr. Robert Godin* for all the good things I have achieved in my life by imitating him.

Table of Contents

List of Figures

List of Tables

List of Acronyms

ATR	Attenuated Total Reflection
BHFA	Buffered hydrofluoric acid
FOEWS	Fiber Optic Evanescent Wave Sensor
FTIR	Frustrated total internal reflection
GPIB	General Purpose Interface Bus
HF	Hydro Fluoric
IOR	Index of Refraction
IR	Infrared
LED	Light Emitting Diode
NA	Numerical Aperture
SEM	Scanning Electron Microscope
SPR	Surface Plasmon Resonance
TIR	Total Internal Reflection
TMM	Transfer Matrix Method

Chapter 1
Introduction

The need to monitor, measure, and understand many of the processes not easily accessible to direct observation in today's technological society, drives the development of better sensors and sensor systems. Consequently, there is always the need to improve current sensor methods. Crucial to the improvement to sensor technology is the ability to understand and model the physical phenomena governing the sensing mechanism.

The use of fiber optic as a foundation for the design of fiber optic sensors, has been the subject of active research for the past thirty years. The ease of availability of photonic components including, lasers, light emitting diode (LEDs), detectors, and optical fibers in particular has encouraged the growth and development of the fiber optic sensor field. With continued improvement in the availability and manufacturing costs of specialized optical fibers and components, the further proliferation and development of the fiber optic sensor industry will only continue to grow.

Various principles of light modulation are used to develop fiber optic sensors including intensity, wavelength, phase, polarization and spectra of the light propagating inside the fiber. A common sensor design using an intensity based measurement relies on the creation of evanescent waves that allow for interactions to take place between light propagating inside a fiber core and the outside environment. In such types of sensors, a section of cladding is thinned by means of chemical or mechanical processes from the optical fiber so that reflection losses in the thinned region modulate the transmission intensity of the sensor relative to the index of refraction of the external media.

1.1 Motivation

With the recent focus on the use of lithium-ion batteries as an alternative to fossil fuels, the estimation of charge in lithium-ion batteries has become a focus of active research. Current methods for charge estimation rely on non-direct methods such as coulomb counting. With such methods, the charge estimate is based on net energy transfer to the lithium cell. Coulomb counting is accurate at predicting charge state under low charge rates and short rest periods. However, if the lithium cell is exposed to various charge rates, temperature changes, or extended periods of inactivity, in direct methods of charge estimation lose accuracy.

One promising alternative for lithium-ion charge estimate entails direct monitoring chemical composition of the cells electrodes during use. A sensor capable of such a function would be required to be chemically inert to avoid interfering with the natural chemical processes of the cell, and immune to the electronic interferences of the cell. Fiber optics are a natural and very promising candidate for such a sensor as they are chemically inert and immune to electromagnetic interferences. In addition, fiber optic sensors are small enough to feasibly fit inside a battery cell environment without drastically modifying conventional designs. This is the first time that an intensity based optical fiber sensor is placed into a fully functional lithium ion battery cell for the purpose of monitoring the state of charge.

Intensity based fiber optic sensors require the least complex and thus inexpensive sensor design and photonic components. The design of most intensity based sensors requires the reduction of the cladding thickness within a given length of an optical fiber to allow the light propagating within the fiber to interact with an external environment. The transmission of light through the optical fiber thus becomes a function of the optical and contact properties of the external media. Sensors of this design are referred to as a FOEWS. The process of thinning a portion of the optical fiber cladding to gain access to light propagating within the fiber core results in a reduction in the diameter. In the case of single mode fibers, the core diameter is typically less than ten microns in diameter. Thinning the cladding enough to allow for environmental interactions with light within the core would result in an extremely small fiber diameter within that region. Such a small fiber cross section would make it extremely likely that the optical fiber would break while insertion into a battery cell during fabrication, or during battery operation. In contrast, multimode optical fibers have a much larger core diameter, roughly ten times that of a single mode fiber. Accessing the core in multimode fibers requires considerable less removal of the cladding and lessen reduction in structural integrity of the fiber.

Accurate theoretical formulations for FOEWS utilizing single mode fibers rely of wave-optic descriptions of light. Practical use of such a formulation can be readily carried out using numerical techniques to solve the Maxwell equations within the framework of a single mode fiber due to the optically small diameter of a single mode core. This is not the case for multimode FOEWS, where the fiber core is several orders of magnitude larger than the wavelength of light being analyzed. To ensure that the numerical solutions converge properly, the sampling distance of the mesh must be small enough to ensure proper description of the excitation wavelength. Even when powerful computers are utilized, the problem domain is too large to be solved practically. Therefore, one must resort to a geometrical optics description. General theories for multimode uncladded, step index multimode fibers have been presented under the framework of geometric optics. However, when partially, or thin cladded sensors are considered, proper description of the thin film interference effects between the fiber core, cladding, and external media cannot be accomplished with a geometric optics theory. Under the framework of geometric optics, it is assumed that light rays are interacting with structures that are large with respect to the wavelength. With the presence of a thin film cladding, the thickness of the cladding is smaller then or comparable to the wavelength of the light. When light rays pass through thin layer media, multiple reflections occurring between the entry and exit interfaces of the layer interfere and modify both the transmission and reflection properties of the layer. Additionally, geometric optics fails to describe the optical tunneling effect of rays of high incident angles on thin layers which will be discussed in more detail in Chapters 2 and 3. Attempts to account for the thin film interference effects into multimode FOEWS models are available in the literature, however, as discussed in Chapter 2, no solution has been presented which is able to fully describe this process.

This lack of a full incorporation of the thin film interference analysis into the geometric optics theory of a multimode FOEWS motivates the work of this thesis.

1.2 Objectives

In this thesis, an analytical technique for the description of the attenuated losses of light rays interacting with the thin film layered interface within the sensing region of the device is developed. This technique uses the transfer matrix method to solve for the attenuated reflection caused by the thin film interactions of light with the thinly cladded sensing region of the FOEWS. The inclusion of the method to the existing geometric optics descriptions for multimode FOEWS, maintains the speed and efficiency of the original algorithm while allowing for increased functionality within the model. The newly modified model is then used to analyze the effect of cladding thickness and sensing length on sensor performance. Additionally, under the framework of the transfer matrix method, predictions on the nature of surface contact between the fiber sensing region and a solid measurand are made by the addition of a fourth thin film to the layer stack representing areas of non-contact.

The extension to the model is tested against in-house experimental results as well as previously published competing methods. The nature of surface contact of a fiber optic FOEWS with a lithium-ion cell anode are characterized using SEM images of disassembled lithium-ion battery cell anodes fabricated to test the sensor. Mean values for surface contact ratio as well as non-contact region sizes and depth are determined from the SEM samples. Predictions on the change in transmission response of a fiber optic FOEWS due to partial contact between sensor and solid anode are made and discussed.

1.3 Organization of the thesis

The thesis is divided into four chapters. In Chapter 2 an overview on intensity based fiber optic sensors is presented along with their practical applications. A review of the different types of analysis performed on multimode fiber optic FOEWS explaining the difficulties in their modeling follows. Finally, a survey of methods used to analyze the attenuation factor caused by the thin film sensing region is given. The survey highlights the gaps in methodology present in published works that prevents a more accurate characterization of the thin film cladding effects.

In Chapter 3, the modifications to current geometric optic representations of multimode FOEWS are proposed. A full description of how the transfer matrix method is applied to analyze transmission through the sensor is given. The model is then applied to cases of sensing both liquid and solid measurands. Performance variations caused by changes in cladding thickness and sensing length for liquid measurands are discussed. Chapter 4 presents the experimental validation of the model using liquid measurands. First simulation results of the modified model under variations in sensor geometry, illumination conditions and contact nature are presented. The set up for experimental validation is described and the results are presented for several fabricated sensors with several test samples. Comparison between the experimental and predicted simulated results are made as well as comparison to alternative models found in the literature.

Chapter 5 utilizes the convenience of modeling multi-layer stack structures via the transfer matrix method. In this section, the partial contact of a solid measurand is added to the model. Partial contact is modeled by averaging the transmission predictions obtained using a three layer stack structure to represent direct contact and a four layer stack structure to represent in direct contact. The four layer stack assumes a layer of liquid between the cladding and measurand layers. The thickness of the gap layer is obtained from empirical observations of a fiber in contact with graphite that has been used as the anode of a lithium-ion battery cell. An analysis of various launching conditions onto the fiber optic face is also developed. Equations for the propagating ray angles and intensities are derived for a general Lambertian LED source incident at arbitrary distances and tilt angles. Values for surface area contact ratio and non-contact void region depths are determined and generalized mean values are found.

Finally, a mean surface contact value is used to simulate the effect of partial contact on the sensor performance.

Chapter 6 concludes the thesis by listing the main contributions and outlining the steps required to use the model as a validation tool for chemical models of battery state of charge.

Finally, Appendix A contains background theory of geometric and wave optics treatment of fiber optic sensors. While Appendix B presents the Matlab code for the extended geometric optics model develop in this thesis.

Chapter 2

Literature Review

Optical fibers based on the coaxial structure of silica and silica doped glasses have been widely available for their use as sensors. Fiber optic sensors operate by monitoring the characteristics of the light propagating within as a function of a perturbing environment. Fiber optic sensors can be divided into two basic categories: wavelength modulated and intensity modulated sensors. Wavelength modulated sensors such as fiber Bragg grating sensors operate by monitoring the wavelength of a reflected wave sent into a single mode optical fiber containing a fiber Bragg grating achieved by creating a periodic variation in the refractive index of the fiber core. This Bragg grading acts as a wavelength specific dielectric mirror which reflects light of a specific wavelength based on the perturbing environments effect on the refractive indices of the grating. Wavelength modulated sensors provide high accuracy and precision but require the use of spectrum analyzers to monitor the wavelength of the reflected signal. Intensity modulated sensors detect a change in the amount of light that is a function of a perturbing environment. The change in the amount of light can be associated with transmission, reflection, absorption, scattering or fluorescence within the optical fiber [1]. Within the field of intensity based fiber optic sensors, there exist many designs, each of which can be analyzed using several different theoretical frameworks. In this chapter the endeavor is to give a broad overview of the common sensor types, methods for their analysis, as well as some common applications for each.

2.1 Types of Intensity Based Fiber Optic Sensors

Fiber optic sensors work by modulating the properties of the light propagating through the fiber core. Various principles of light modulation are used to develop sensors, but the most common rely on the modulation of intensity or phase of the light propagating inside the fiber. Intensity based sensors detect the change in light power as a function of either the optical properties of the measurand in contact with the sensor, or the deformation of the optical fiber based on the perturbing environment. Phase based sensors detect the phase shift of light from a coherent laser light source by utilizing interferometric methods. Common interferometric methods include the Fabry-Perot, Sagnac, Mach-Zehnder, and Michelson interferometers [2]. Interferometric methods are able to attain a high level of sensitivity but are difficult to set up than intensity based sensors [2]–[4].

Regardless of the principle of modulation the measurand sample must be allowed to interact, whether extrinsically or intrinsically, with the light propagating within the optical fiber core. Extrinsic sensors modulate the light inside the fiber by indirectly allowing the measurand to interact with light within the fiber. In extrinsic sensors the fiber serves only to carry optical power and the sensing information to and from, an external region [5]. While in intrinsic sensors the light propagating in the fiber is affected directly by the measurand, and the modulation of the light is measured at the fiber output.

2.1.1 Methods for intensity based fiber optic sensing

Intensity based fiber optic sensors modulate the transmission intensity of light within the optical fiber based on the properties of the measurand. These types of fiber optic sensors have offer the advantages of ease of fabrication, robustness, and simplicity of signal processing [5].

Often referred to frustrated total internal reflection (FTIR) fiber optic sensors. Similar in set up to FTIR sensors are attenuated total internal reflection sensors. Both attenuated and frustrated sensors make use of the evanescent field created from the total internal reflections on thin media of low optical density.

2.1.2 Frustrated Total Internal Reflection

Intensity based fiber sensors offer the advantages of ease of fabrication, robustness, and simplicity of signal processing. FTIR based sensors are designed around the evanescent wave produced when a wave is incident from a high index of refraction media onto a low index material at angles higher than the critical angle. If there exists a secondary boundary to a third optically denser than the second media in close proximity to the first boundary, the evanescent field will not decay, transmitting energy into the third media Figure 1. The first interface does not fully reflect the incident light and the total internal reflection is then frustrated.

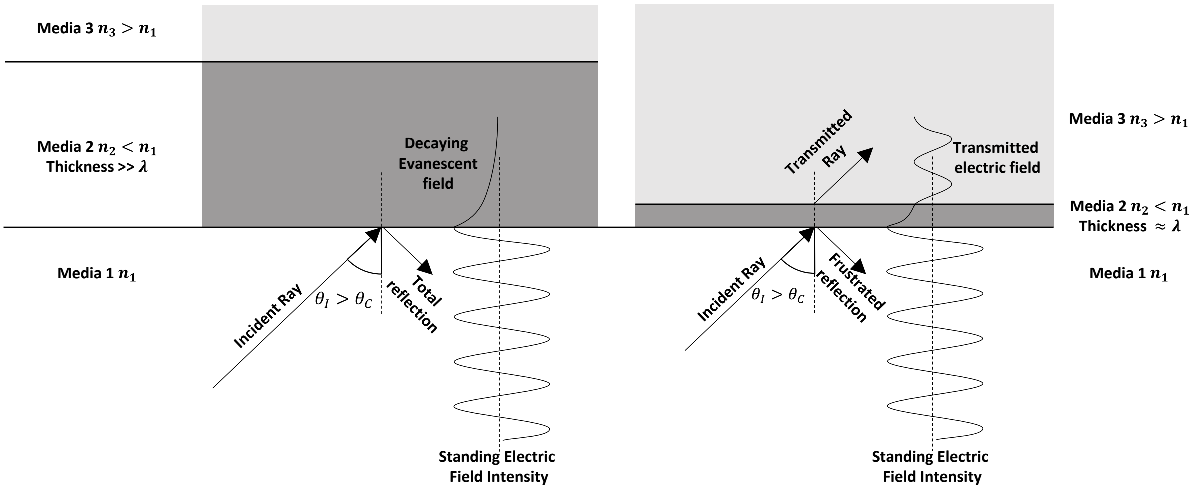

Figure 1: Representation of FTIR occurring when an optically dense medium (media 3) is brought into proximity to the interface between media 1 and media 3. When the distance between the two interfaces is on the order of the wavelength, the light tunnels through the second media via the evanescent wave resulting in a transmitted ray into media 3.

Spillman and McMahon proposed a method for measuring acoustic waves using two angular cut fibers held closely together as shown in Figure 2 [6]. They choose to polish the optical fiber faces at angles large enough to guarantee complete total internal reflection for all propagating modes. By bringing the two fiber ends in proximity to one another, light was coupled between the fibers by means of optical tunneling. The intensity of light coupled between both fibers would modulate due to vibration caused by the acoustic waves changing the distance between the adjacent fibers.

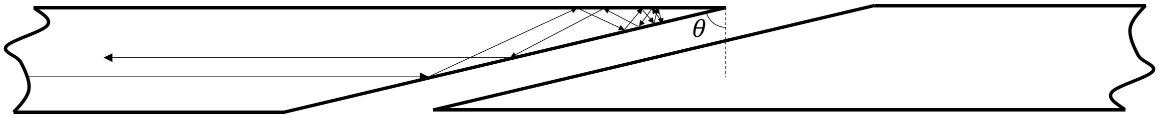

Figure 2: Angular polished optical fibers held in close proximity to one another so that light may be coupled between them via FTIR. The polish angle $\boldsymbol{\theta}$ is chosen large enough to guarantee total internal reflection for all propagating modes.

A similar edge butted fiber sensor has been used in a more direct fashion to measure refractive index changes in sample solution encompassing the fiber coupling. Rahnavardy et al. made use of a FTIR end sensors as a simple intensity modulated strain and pressure sensor [5]. Theoretical description of the frustrated reflection was accomplished by solving the Maxwell field equations explicitly for a three infinite layer stack geometry. They were able to demonstrate a close correlation between theory and experimental results.

Court and Willisen [7] applied the phenomena of FTIR to laser cavity design. Analysis of the optical tunneling effect was accomplished using Froersterling's [8] solution for the amplitude reflection coefficient of a thin film in combination with the Fresnel equations to account for the phase coefficients. The final solutions for the s polarized transmission coefficients of a thin film lossless dielectric between two semi-infinite isotropic dielectrics was given as:

$$T = \frac{1}{\alpha_s \sinh^2 y + \beta} \tag{1}$$

Where

$$y = \frac{2\pi n_1 d}{\lambda} \sqrt{N^2 \sin^2 \varphi_0 - 1}; \tag{2}$$

$$\alpha_s = \frac{(N^2 - 1)(n^2 N^2 - 1\,)}{4N^2 \cos \varphi_0 \,(N^2 \sin^2 \varphi_0 - 1)\sqrt{n^2 - \sin^2 \varphi_0}} \tag{3}$$

$$\beta_s = \frac{\left(\sqrt{n^2 - \sin^2 \varphi_0} + \cos \varphi_0\right)^2}{4 \cos \varphi_0 \sqrt{n^2 - \sin^2 \varphi_0}} \tag{4}$$

$$n = \frac{n_2}{n_0}, N = \frac{n_0}{n_1}. \tag{5}$$

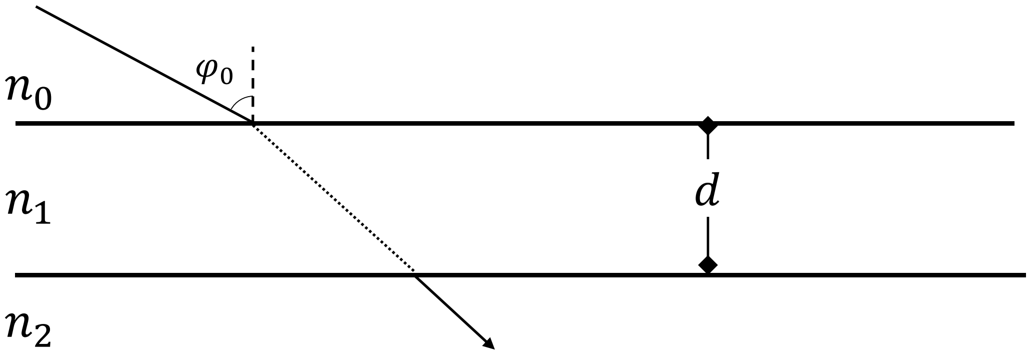

Figure 3: FTIR of an electromagnetic wave through a thin film between two half infinite spaces.

Predictions in transmission intensity as a function of the optical length of the thin film for index ratio of $N = 1.540$ for a ray incident at $\varphi_0 = \frac{\pi}{4}$ where presented for various ratios of n. Predictions indicated that the transmission intensity drops significantly for thin film thicknesses exceeding the wavelength of the electromagnetic wave regardless of the index ratio n. Results are reproduced in Figure 4 for clarity.

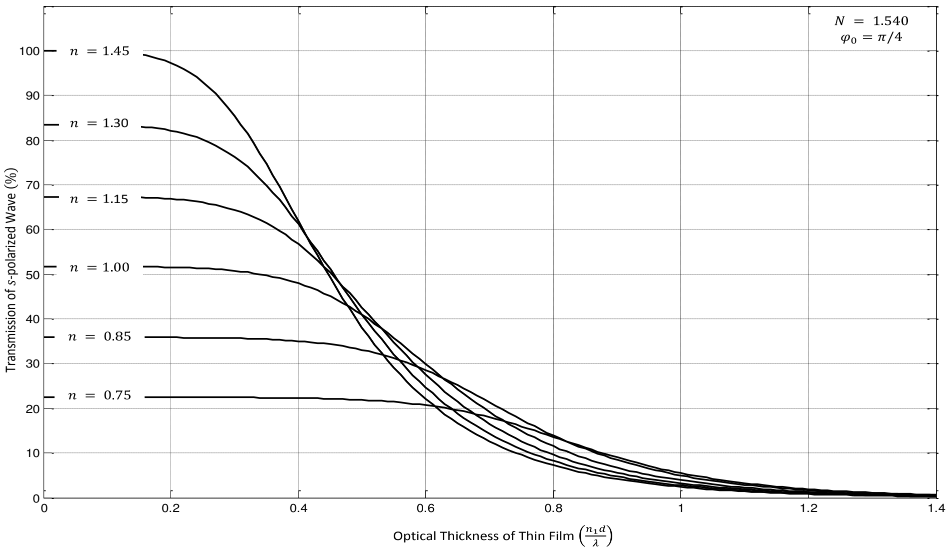

Figure 4: Transmission of the s component of an electromagnetic wave incident at $\boldsymbol{\pi/4}$ radians reproduced from [7].

The theoretical analysis accomplished by Court and Willisen [7] of FTIR of a three layer stratified media became the foundation of for several application of the phenomena FTIR analysis such as microscopy [9]

2.1.3 Reflection based sensing

More recently the work of Nash et al. [10] developed an all-fiber optic sensor for use as a liquid refractometer. The sensor was fabricated from a ply methyl methacrylate multimode fiber. The end of the fiber was polished at various radii of curvature. With such a curvature in the fiber tip, low order modes of propagating light escape the fiber tip decreasing the back reflected signal, while higher order modes for which the angle of incidence at the core-air interface exceeds the critical angle reflected light along the fiber. The back reflected light is a function of the refractive index of the sample liquid. Calibration of the sensor was accomplished using empirical correlation of the back reflected light and the refractive index of the sample. Refractive index resolution of 0.002 was achieved with an upper limit of sensing of 1.467 determined by the refractive index of the core.

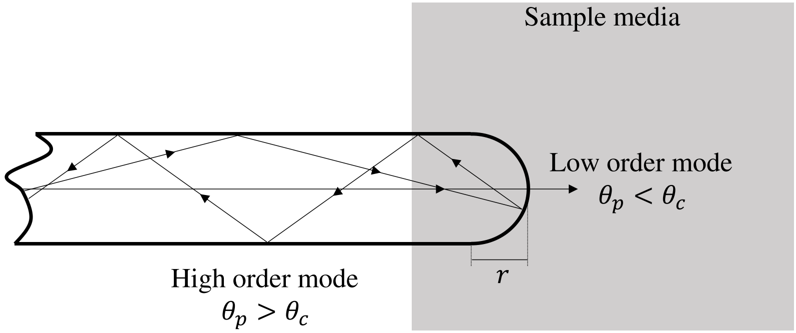

Figure 5: Schematic representation of fiber optic refractometer fabricated by polishing a multimode fiber with a radius of curvature r. The curved end face limits the transmission of high order modes with propagation angles higher than the critical angle out of the fiber.

2.1.4 Transmission based sensing

2.1.4.1 Early development of waveguide sensors

In 1986, Simhony, Kosower and Katzir demonstrated the feasibility of using infrared fibers as light conductors for total internal reflection measurements in a Fourier transform infrared spectrometer to obtain the spectra of aqueous solutions [11]. Simple uncladded waveguide fibers were fabricated by extruding silver halide crystals through a die. The resulting fiber was then placed inside a Pyrex capillary tube having a filling port. By filling the capillary tube with various samples, the spectra was measured by exciting different wavelengths of light through the fiber and measuring the resultant transmission loss.

2.1.4.2 Fiber optic based sensors

The use of commercial optical fibers as a replacement for the silver halide fiber was then demonstrated shortly after by several other authors [8][9][14]. With the use of commercial optical fibers, the presence of a cladding material on the fiber modified the mechanism of sensing in comparison to the original work of [11]. Light propagates through the core an optical fiber and is kept from interacting with the external environment due to the presence cladding surrounding the fiber core. In order to allow the light within the core to interact with the external environment, the fiber was bent to a small radius of curvature forcing the presence of evanescent modes able to interact with the external environment. DeGrandpre et al. [13] managed to excited evanescing modes capable of interacting with a liquid measurand within a region of an unmodified commercial fiber by bending portion the fiber to a small radius of curvature. While, Tai et al. [14] tapered a portion of the optical fiber by heat treatment reducing the thickness of the cladding again allowing evanescent modes to interact with an external environment.

2.2 Modeling of Intensity Based Sensors

2.2.1 Methods to use geometric optics and light rays

A general theory for the geometry optics approach to evanescent wave spectroscopy in multimode optical fibers was put forth by Messica et al. near the end of the last century [15]. The theoretical paper outlined a method to predict the transmission behavior for a fiber optic sensor designed with a completely uncladded sensing region. An arbitrary intensity angular distribution of both skew and meridional rays was taken as the illumination conditions of the input fiber face. Given the angular direction of each ray, a generalized transmission function whose form accounted for several factors was derived. The total power transmitted through the optical fiber sensor was then found as the double integral of the transmission function convoluted with the intensity distribution function over the fiber input face and solid angle.

2.2.2 Examples of attempts to include effects of partial cladding

The geometric layout of a partially cladded sensing region is represented simply by a three media layer stack. In such a configuration, two interfaces are present, each of which produce transmitted and reflected waves. As a result of reflection and transmission at each interface caused by a single incoming electromagnetic excitation, secondary and higher order rays are created by multiple internal reflections within the middle layer.

Buric et al. [12] recently published a new method for the analysis of thin cladding sensing regions with cladding thicknesses on the order of one wavelength. The fabrication of the sensing region constituted the complete removal of the silica cladding material, followed by the addition of a new thin cladding material. The resulting geometry of the sensing region of the fiber consisted of a three layer stack of media with a thin film of cladding separating the core from the external environment. The attenuation losses within the sensing region were modeled utilizing multiple reflection coefficients of the Fresnel equation.

2.2.2.1 Rigorous analytical solution to the Maxwell equations.

While studying the effects of gold nanoparticle coatings on the modal propagation constants of optical fibers. Choudhury [17] used a rigorous approach to solve a four layer stack profile of the coated optical fiber that was made of the fiber core, cladding, nanoparticle layer, and free space environment. The field solution was derived for cylindrical symmetry of the fiber geometry, and matching the solutions at the layer interfaces. Solutions within each of the four regions of the fiber cross section where considered as Bessel and modified Bessel functions of the first and second kind. Implementation of the boundary conditions at each interface yielded a system of twelve equations that were used to derive the modal propagation constants of the coated fiber. Theoretical analysis of the solutions were performed to predict the effects of nano-coating thickness on the number of propagating modes of the fiber. In a recent extension to this work, modification to the rigorous solution were applied to model the effect of stress/strain due to twisting of the optical fiber on the propagation characteristics of a fiber[18], [19].

2.2.2.2 Transmission line equivalent

A transmission line equivalent model to analyze the optical tunneling phenomena caused by a multi-layer stack thin film structure was completed by Pieper et. al.[20]. The thin film optical structure was made analogous to a transmission line using the Telegraph equations:

$$\frac{\partial I}{\partial x} = -Y_l V \ \frac{\partial V}{\partial x} = -Z_l V. \tag{6}$$

The electrical phasors are identified as I for current and V for voltage, while the complex admittance and impedance per unit length are Y_l and Z_l respectively. The translation from the electrical quantities to the optical field elements were derived in [21] and are repeated in Table 1 below for clarity.

Table 1: Translation from optical field components to electric quantities for the transmission line analogue of s and p polarized waves in multi-layer stack thin film analysis [21].

S-Wave	**P-Wave**
$(-E_y) \leftrightarrow V$	$E_x \leftrightarrow V$
$H_x \leftrightarrow I$	$H_y \leftrightarrow I$
$j\omega\epsilon \cos^2\theta = Y_l$	$j\omega\epsilon = Y_l$
$j\omega\mu_o = Z_l$	$j\omega\mu_o \cos^2\theta = Z_l$
$z \leftrightarrow x$	

Where ω is the radian frequency of the incoming wave, ϵ is the electric permittivity, μ_0 is the magnetic permeability, E_y, E_x are the electric fields, and H_x, H_y are the magnetic fields for the s and p polarized waves. The change of the coordinate axis z to x indicates that the normal direction of optical incidence $(z)$is replaced by the transmission line axis (x). The equations of Table 1 are valid under:

$$\omega\sqrt{\epsilon_i\mu_0} = \frac{\omega}{v_i} = \frac{2\pi}{\lambda_i} = \frac{2\pi n_i}{\lambda} \tag{7}$$

Where λ is the vacuum wavelength, and v_i, λ_i, n_i are the wave speed, wavelength, and index of refraction in the i^{th}layer of a thin film stack.

Within the framework of transmission line theory, the multi-layer stack geometry of Figure 6 can be represented as the series of transmission lines of Figure 7.

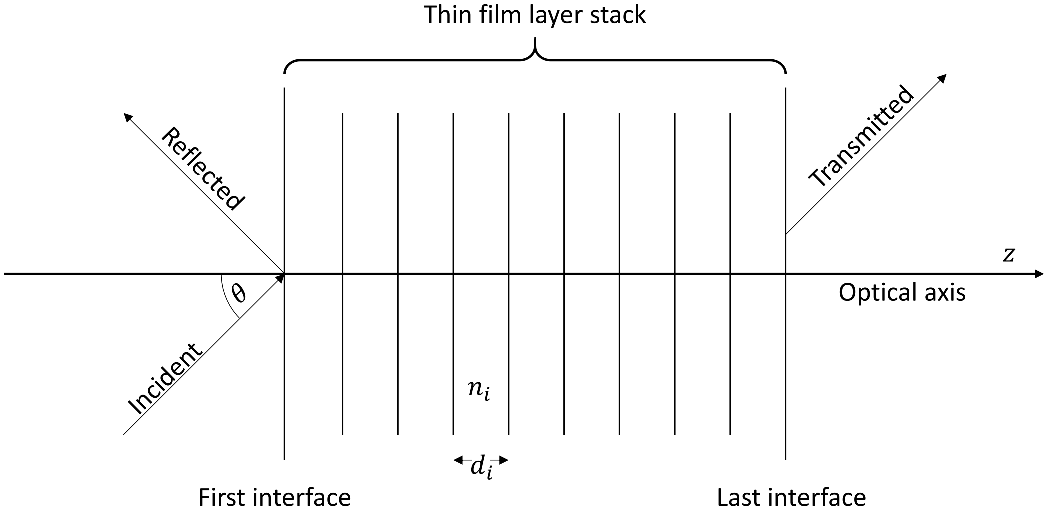

Figure 6: Schematic representation of an incident wave of a multi-layer thin film stack.

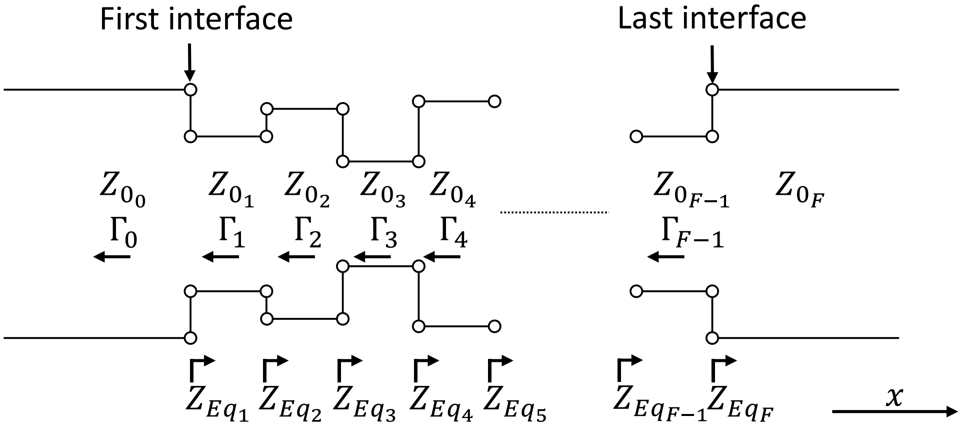

Figure 7: Transmission line equivalent model for the multi-layer stack geometry of Figure 6.

The algorithm used to compute the reflection coefficient Γ_0 of Figure 7 first requires the calculation of the propagation angles for each media in the thin film stack using Snell's law computed from the first interface to the last. Once the propagation angles for all layers are found, the algorithm then operates from the last interface on the right hand side working back through the layer stack towards the first interface. Beginning with the last interface, the reflection coefficient of the interface separating layers $F-1$ and F are found using the impedances of each layer and the reflection equation [22]:

$$\Gamma_{F-1} = \frac{Z_{0_F} - Z_{0_{F-1}}}{Z_{0_F} + Z_{0_{F-1}}}. \tag{8}$$

With the reflection coefficient of the final interface, the equivalent impedance of the $F-1$ layer is then calculated using [22]:

$$Z_{Eq_{F-1}} = Z_0\left(\frac{1+\Gamma_{F-1}e^{j2\Delta\phi_{F-1}}}{1-\Gamma_{F-1}e^{j2\Delta\phi_{F-1}}}\right). \tag{9}$$

Note that since there is no reflection after the final interface that $Z_{Eq_F} = 0$. The algorithm then reiterates moving towards the left, using the above Eq. (8) and (9) until reaching the first interface and determining the overall reflection coefficient Γ_0.

2.2.2.3 Transfer matrix method

An alternative and powerful method of analysis of multi-layer media to the transmission line equivalence method is the transfer matrix method. The transfer matrix method (TMM) relies on the continuity of the electric and magnetic fields across a boundary as defined by Maxwell's equations. A general plane wave solution is assumed to exist within each layer of a multi-layer stack as:

$$E_n(z) = E_{n+}\, e^{ikz} + E_{n-}\, e^{-ikz}. \tag{10}$$

Put into a matrix formulation, and knowing the field at the incident media, the resulting electric and magnetic fields from the multi-layer stack can be derived from simple matrix multiplication. With the multi-layer stack represented in matrix form the transmission and reflection coefficients can also be derived. The full summary and derivation of the TMM is outlined in Appendix A for reference.

The TMM has been utilized in a variety of differing fields. Sharing similarities in geometrical design as FTIR and Attenuated Total Reflection (ATR) phenomena, the resonant optical tunneling effect structure consists of two low refractive index layers sandwiched between three high refractive index layers. The transmission and reflection of light due to this extended tunneling design requires the analysis of evanescing waves through two layers of the structure, while accounting for resonance effects of the light waves due to the thickness and spacing of the three internal layers. The resonant optical tunneling effect was first proposed by Yeh in 1988 [23], and the first experimental validations for the effect were demonstrated by Hayashi in 1999 [24]. Jian and Zhang, recently published a summary on the recent development in the progress of modeling and applications of the resonant optical tunneling effect [25]. Within the summary of modeling methods, they cited the TMM as the standard analysis method to use under the optical interpretation of the phenomena, while comparing it to their newly developed potential barrier method which holds to the quantum mechanics interpretation.

The TMM has also been employed to model the reflection and transmission spectra of grating in fiber Bragg gratings. Oliveira et al. [26] used the TMM in combination with a finite element analysis to design a Bragg grating acousto-optical modulator. The finite element analysis was used to determine the strain field caused by an incident acoustic wave while the TMM was then used to obtain the spectrum corresponding to the strained grating. A similar merging of the TMM with finite element analysis for acousto-optical modulators was also accomplished in [27]–[36].

The modeling of surface plasmon resonance (SPR) type sensors, has also found success by relying on the TMM. SPR is a commonly used technique used for detecting small changes in refractive index of a media using a thin metallic layer sandwiched between dielectric and analyte layers. One standard sensor set up for SPR is the Kretschmann configuration [37] which consist of a prism directing light onto a metallic layer that is in contact with the analyte as seen in Figure 8. For use in bio-sensing applications, the surface of the metallic layer is functionalized with ligands which are chosen to bind to the target molecule present in the analyte. The binding of the target molecule with the ligand on the metallic surface changes the properties of the metallic and analyte solution interfaces, resulting in a change in the reflected light within the prism.

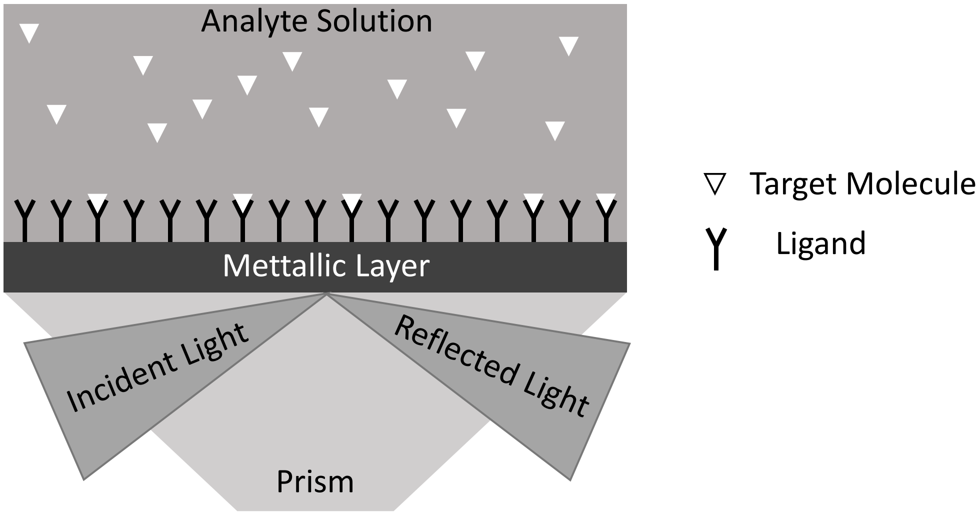

Figure 8: Kretschmann configuration for SPR based sensing.

Direct use of the TMM for the modeling of the reflected light resulting from the Krestchmann configuration has been reported by [38]–[42]. With the ever increasing need for miniaturization and integration, alternative configurations for SPR sensors are being developed. Consequently, there has been an increased interest in fiber optic based SPR sensors [43]–[46]. Kanso et al. [42] developed a numerical model for an optical fiber sensor based on SPR where the analyte/metallic layer interface was modeled using the TMM. They were able to demonstrate good agreement between experimental and simulated results which have been reproduced here for convenience in Figure 9.

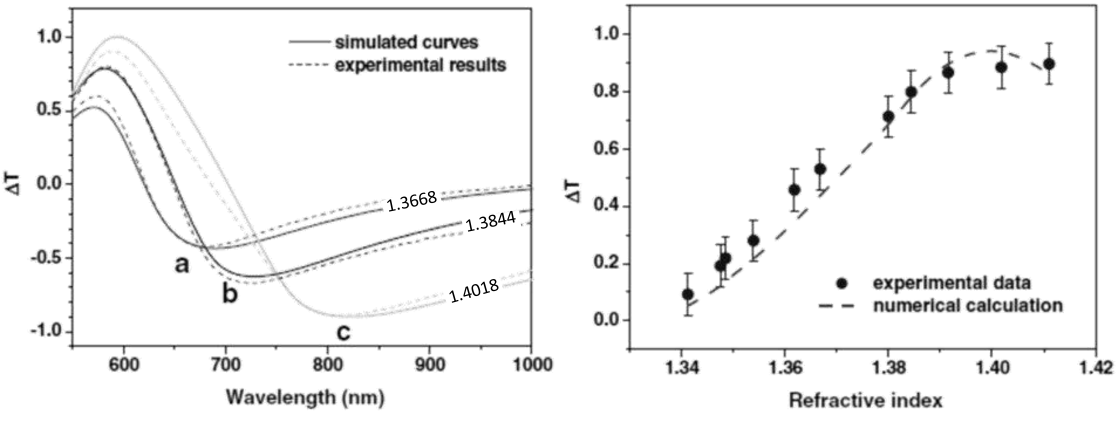

Figure 9: Comparison of experimental and simulated results modeling an optical fiber based SPR sensor. Reproduced from Kanso et al. [42].

The validation between simulated and experimental results for the transmission characteristics of the fiber optics based SPR sensor was done on a relative scale whereby, both the simulated and experimental results were normalized to the transmission intensity of a reference sample.

Ongoing research in fiber optics based SPR sensors continues to be carried out, leasing to the development of low cost SPR sensors by the authors of [47]–[51]. While competing methods of analysis to the TMM have been used including finite element through Comsol® in [51], the TMM remains a strong tool for the full description of the reflection coefficient at the SPR interface, indicated by the recent work of Liu et al. [49] which extended the work of Kanso et al [42] to include skew ray propagation in ray based models of multimode fiber optics SPR sensor.

2.2.3 Examples of empirical calibration of sensors

The transmission of light through the FOEWS has been described using a Lambert-Beer law defined by:

$$P(Z) = P(0)e^{(-NTZ)}, \tag{11}$$

where I_{in} is represents the intensity of light incident on the fiber, while, $P(Z)$ is the intensity remaining at a distance Z along the fiber with an absorbing cladding. The attenuation of the fiber is described by the coefficient N which is a function of the number of reflections a traveling ray makes with the lossy cladding interface, while T is the transmission coefficient of the light penetrating the lossy cladding [52].

This exponential decay model of the transmission of light through a FOEWS depends explicitly on the definition of the absorption coefficient T. Ruddy proposed an effective attenuation coefficient for multimode fibers in [52]. The effective absorption coefficient partially accounted for the presence of a thin lossy cladding utilizing Fresnel equations with a modified complex index of refraction to describe the absorption behavior of the lossy cladding. The disadvantage of this methods is that the modified complex portion of the index of refraction (IOR) must be determined a priori, and is not arrived at using an analytical expression. The goal of this thesis will be to develop a model that will not rely on the use of modified empirical variables to describe the transmission response of sensors.

2.2.4 Modeling of launch conditions for FOEWSs

The performance of a FOEWS relies heavily on the distribution of propagating angles of light rays within the fiber. A theoretical analysis of the variation in response due to changes in launching conditions was carried out by Messica et al.[15]. The model used to simulate an FOEWS relied on the Fresnel equations to describe the transmission loss through the sensing region of the fiber as described in the previous section. Analyzing both laser beam and blackbody illumination sources through a focusing lens, studied three separate illumination conditions. The geometry of illumination conditions is outlined in Figure 10. Three separate illumination set ups where examined: blackbody illumination source through a focal lens, in a center spot and off center spot illumination, and a laser off center spot configuration. Analysis of the three cases determined that only meridional rays are excited in a center spot illumination set up, while the off centered spot configuration with a laser source excited only skew rays. It was concluded that the off centered spot with laser illumination was superior to the other cases based on sensitivity and detection limit.

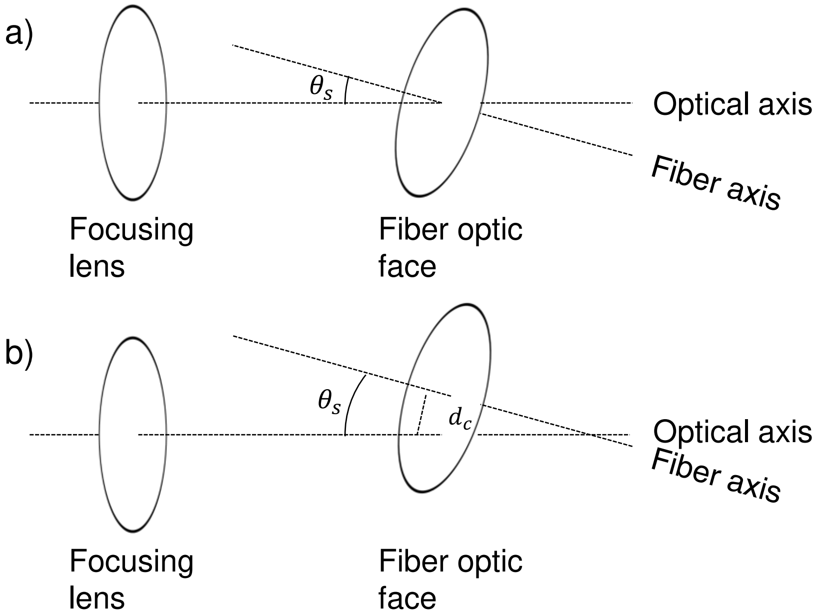

Figure 10: Description of illumination geometry as conducted by Messica et al. [15]. a) The coincidence of the optical and fiber axis at the center of the fiber optic face describes a center spot illumination set up with off center distance d_s. b) Whereas an off centered illumination spot occurs when the optical and fiber axes do not coincide at the fiber face center.

The description of light from a diffuse Lambertian light source onto a fiber face was fully developed by Love et al. in [53], using trigonometric relationships. Similar to the Messica treatment of launching conditions, the propagation of light within the fiber assumes that the optical fiber is perfectly straight and as such, the angle of incidence of rays interacting with the sensing region are determined by the initial entry angle of light from the source to the fiber entry face. Using this idealization, Love et al. conducted a theoretical analysis of the effects of spot size, and launch angle. The analysis concluded that the transmission intensity of the sensor was approximately proportional to the square of the spot radius. They also concluded that the power loss increased with increasing launch angle since higher launch angles lead to a large number of reflections within the sensing region of the fiber. The equations derived by Love et al. were subsequently utilized by McCabe for the investigation of fiber optic gas sensors [54], and by O'Keeffe, for the analysis of fluorescent evanescent wave sensors [1].

The work of Chyad at el. Assumed a collimated laser beam focused onto the fiber axis, which excited only meridional rays in the simulation [55]. The equations for the illumination by a collimated beam were taking form the work of Born and Wolf [21].

The work completed by Buric et al. [16] resulted in a ray based model again relying on the Fresnel equations to describe the absorption loss due to a modified FOEWS. Unlike the Messica model above, the description of light entering the fiber was not derived analytically but instead made to match empirical values based on reference experimental results.

2.2.5 Surface roughness

The fundamental step in the fabrication of a FOEWS is the thinning of the cladding material surrounding the fiber core. Reported methods for the modification of the cladding material include: tapering by means of heating and pulling the fiber [56]–[60], side polishing the fiber resulting in half exposure of the fiber core [61]–[65], or chemical etching of the cladding material using buffered hydrofluoric acid (BHFA) [66]–[69]. Chemical etching was used to fabricate the sensor modeled in this study.

The process of etching the fiber using BHFA can result in pitting of the fiber surface. Zhong et al. [67], [68] published results on the surface quality of BHFA etch silica optical fibers. Using various buffering concentrations of BHFA under various ultrasonic agitation strengths, average surface pitting depths and widths ranged from 3.82 μm to 8.49 μm and 0.16 μm to 2.67 μm respectively [68]. They determined that optimal surface quality of the etched surface can be obtained using BHFA of pH 5.34, under the influence of ultrasonic agitation.

The theoretical analysis of surface roughness due to complete etching of the optical fiber cladding material was presented by Zhong et al. [67] using the Lambert-Beer model for transmission of light through an evanescent wave sensor given by Eq.(11) above. In a rough surface fiber optic sensor, the propagation path of light incident on the fiber core/external media interface will vary based upon the depth and diameter of the surface pits. Zhong et al. pointed out that the presence of surface roughness will affect the incident angle of the light ray impacting on the interface between the fiber core and the medium. As such, the angle of incidence θ_i of Eq.(12) was modified and expressed as a function of average pit diameter (δ) and depth (Δ) given by:

$$\theta_i' = \theta_i - \arctan\left(\frac{2\delta}{\Delta}\right). \tag{12}$$

Using this method of inclusion of surface roughness, Zhong et al. [67] concluded that as the roughness ($2\delta/\Delta$) decreased the output transmission power of the sensor, whereas the sensitivity initially increased for small roughness before rapidly decreasing with increasing roughness.

In this thesis, the surface roughness of optical fiber sensors etched in BHFA will be mitigated by following the procedure put forth by Zhong et al. [68]. As will be seen in Chapter 4, little to no surface roughness is found on the optical fibers fabricated in this thesis. Therefore, the inclusion of surface roughness effects will not be included in the model developed here. However, a similar statistical characterization of the partial contact of a FOEWS with a solid graphite anode will be conducted in Chapter 5.

Chapter 3

Development of Hybrid Model

Simulation of FOEWS in multimode fibers using wave based optics is computationally intense because the diameter of the core of the fiber can often be orders of magnitude larger than the wavelength of light of interest. As such, ray optics is used to describe the behavior of these FOEWSs. While the core of a multimode FOEWS is optically large, the sensing region is made by thinning the cladding along a length of fiber by means of chemical etching [67], [68] and it is optically small. A general ray theory for the description of FOEWSs has been put forth in other works [15], [64]. In these cases, the analysis of the thin cladding region is usually addressed using effective refractive index values that approximate the optical behavior of a thin cladding sandwiched between the core and external media. A method for the analysis of the thin cladding region that relies on the thin film interference transfer matrix method to determine the reflection loss at the thin cladded interface is presented. This approach solves the full three layer thin film stack without use of effective parameters providing a more rigorous method of analysis. Using the modified theoretical model, the effects of cladding thickness on the power transmission of an FOEWS are investigated.

As a ray optics simulation of an FOEWS is dependent on the distribution of rays propagating within the fiber, it is assumed that the fiber is illumination from a Lambertian LED held at various distances and angles to the fiber face. The generalized angular and intensity distributions for light rays from this set up are then derived. By modifying both the distance of the LED to the fiber face as well as the angle between the fiber axis and LED fiber face axis, the effects of launching conditions on the performance of the FOEWS are studied.

3.1 Description of an FOEWS

The FOEWS studied in this work is designed from a multimode optical fiber with a modified cladded region that acts as the sensing region of the fiber. The full schematic of the modified optical fiber, illumination source and photo detector are depicted in the schematic of Figure 11. The LED illumination sources is considered to be a perfect Lambertian source with a narrow half angle of intensity, that directly illuminates the fiber end face. Section 3.2.3 gives a full description of the light coupling into the optical fiber along with a derivation of the analytical equations governing the light distribution onto the fiber face. The transition of light from the external of the entry face to the interior of the fiber core is subject to Fresnel reflection losses as well as to Snell refraction upon entering the core which will modified the angular distribution within the optical fiber. The light from the LED source is guided along the multimode fiber subject only to Lambert-Beer losses until reaching the sensing region of the fiber. Losses attributed to transmission along the fiber are accounted for in the model and described in Section 3.2.1 below.

The portion of fiber subject to a reduced cladding thickness is called the sensing region of the fiber. It is within this region that the light within the fiber core can tunnel out through the thinned cladding based on the optical properties of the material exterior to the fiber cladding. Light that tunnels out through the sensing region of the fiber results in a transmission intensity loss that can be measured at the output of the fiber. Section 3.2.2 gives a full description of the tunneling phenomena, along with an analytical derivation of the reflection coefficient of light rays incident of the sensing region boundary using the transfer matrix method. The description of light loss within the sensing region of the FOEWS is the most crucial component of the model. As mentioned in the literature review of Chapter 2, many attempts to describe the reflection of light within the sensing region rely on effective parameters and simplifications in geometry that are not capable of fully describing the optical tunneling effect.

After passing through the sensing region of the fiber, the remaining light propagates again through an unmodified multimode fiber until it reaches the exit end face. Again once exiting the fiber end face the light rays are subjected Fresnel reflections further contributing the loss of the transmitted intensity. Within the proceeding model, the Fresnel reflections at fiber end faces are taken into account while computing the transmission power of the FOEWS. The analytical equations describing this loss are summarized in Section 3.2.1 below.

Once the light exits the optical fiber from the end face, the intensity is measured using a photo detector capable of measuring the wavelength of light emitted from the LED source. The photo detector converts the optical signal into a voltage that can then be easily read by an oscilloscope or alternative read out device.

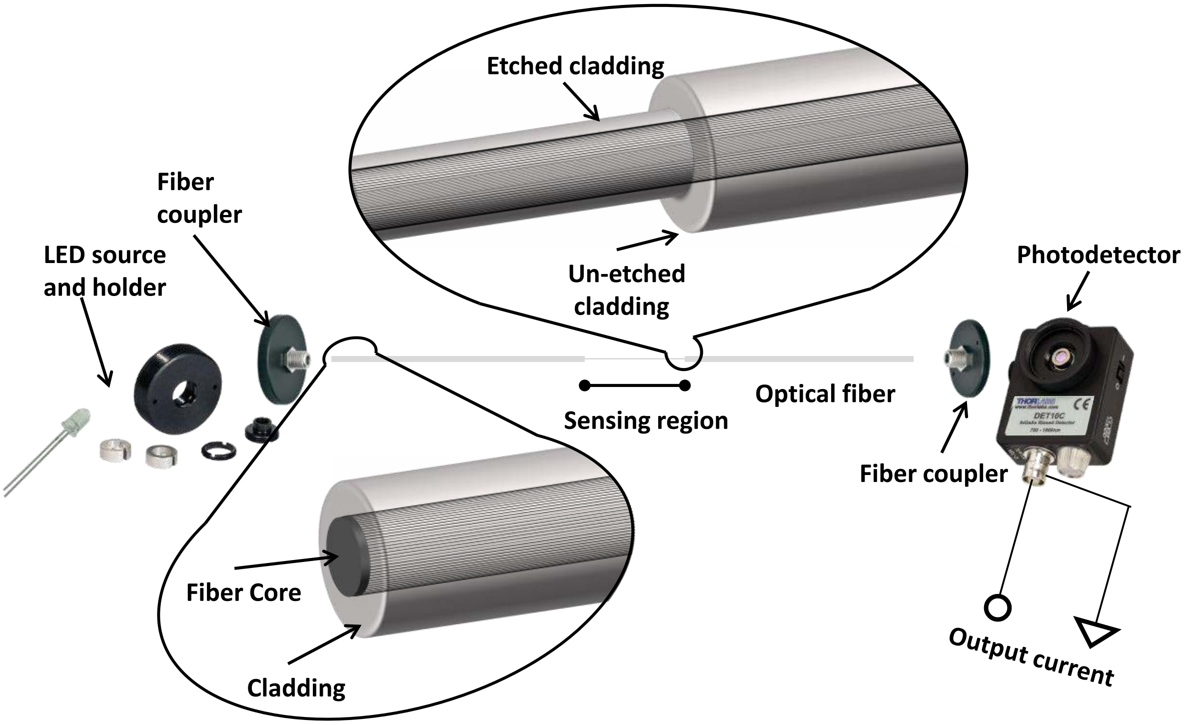

Figure 11: Overview of the FOEWS as studied in this thesis.

3.2 Overview of model structure

Modeling the transmission response of the FOEWS will be accomplished using a hybrid analysis which will exploit the computational simplicity of ray tracing through the optically large domains of the system such as the multimode fiber core, and LED illumination conditions. While utilizing the thin film transfer matrix to accurately model the optically small region corresponding to the light reflection with the thinly cladded sensing region of the system. The output power of the FOEWS will be determined as a two-dimensional integral over the surface of the face of the fiber core given by:

$$P_{out} = \int_S T\big(\theta_I(r,\varphi)\big) \cdot I(r,\varphi)\, dS. \tag{13}$$

The integrand terms T and I represent the transmission and intensity functions of the overall system, while the variables r, and φ, and the polar coordinates on the face of the fiber core. The transmission function models the fiber optic attenuation behavior based on the dimensions of the FOEWS, as a function of the ray propagating through the fiber. The intensity function computes the angular distribution of rays entering the fiber based upon the illumination conditions of the LED onto the fiber face. The integral of Eq. (13), will be done numerically using a double sum where each of the discretization of the surface will represent a guided ray through the FOEWS.

The following sections give full derivations to the various components that make up the integrand functions T and I. The full explicit formulations of the transmission and intensity functions will be given at the end of the chapter before simulation results are presented.

3.2.1 Geometric Optics and Ray Tracing in Multimode Fibers

For multimode optical fibers the core diameter is large relative to the optical wavelength of light. From a modeling approach having an optically large fiber core allows the propagation of light within the fiber to be modeled using a ray based approach.

Step index multimode optical fibers transmit light on the basis of the principle of total internal reflection (TIR) of rays incident on the core cladding interface, as a result of this phenomenon, light rays are guided along the fiber core and propagate with very little loss to the surrounding environment. The basic structure of an optical fiber consists of a central core medium of refractive index n_{core} surrounded by a second medium called the cladding of index of refraction n_{clad}. To ensure TIR at the core cladding interface the IOR of the cladding is chosen to be less than that of the core $(n_{\text{core}} > n_{\text{clad}})$. With the appropriate chose of core and cladding, light propagating within the fiber core will do so while the angle of incidence at the core cladding boundary is greater than the critical angle defined by Snell's law:

$$\theta_c = \arcsin\left(\frac{n_{\text{clad}}}{n_{\text{core}}}\right). \tag{14}$$

Two types of rays can propagate within a multimode fiber while satisfying Snell's law at the core cladding interface. Meridional rays consist of the family of rays that propagate along the fiber while intersecting the fiber axis between each successive reflections off the fiber walls. By passing through the fiber axis between each successive reflection, meridional rays are confined to travel within a single family of planes of the fiber defined which contain the fiber axis. A schematic representation of a meridional ray propagating within a fiber core is given in Figure 12. From the schematic of Figure 12, the ray path is easily followed along the length of the fiber core.

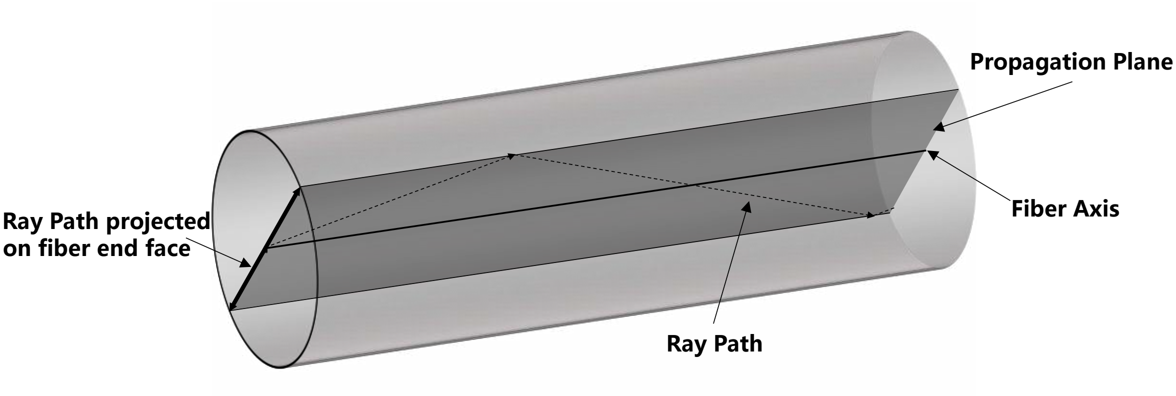

Figure 12: Ray optics representation of a meridional ray propagating through an optical fiber. For clarity, only the fiber core is drawn. Meridional rays propagate along the same propagation plane after each successful reflection.

Analysis of a meridional ray path within the fiber core can be simply analyze using the propagation plane which confines the path of the ray. In Figure 13 the cross section view of meridional ray propagation through an ideal step index optical fiber is shown. Because the meridional ray propagates through the fiber axis, the perpendicular distance travelled by a ray between successive reflections is given simply by the core diameter. In addition to a simple expression for the perpendicular distance travelled by meridional rays, the calculation for the angle of incidence of meridional rays on the core cladding interface is simply computed using the single angle of propagation within the meridional plane.

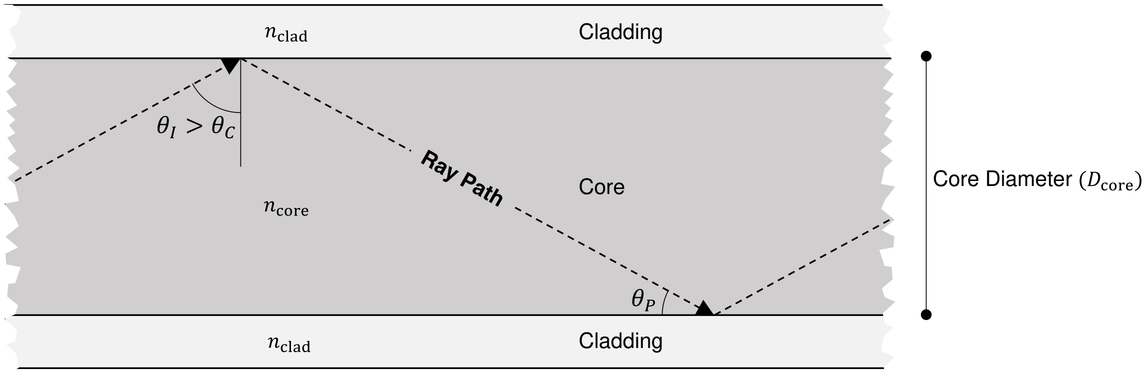

Figure 13: Meridional ray planar propagation through a step index multimode fiber. Propagation of the meridional ray is dependent upon the condition that the angle of incidence $\boldsymbol{\theta_I}$ is greater than the critical angle for TIR of meridional rays defined in Eq.(14).

In comparison, skew rays, travel along the fiber without intersecting the fiber axis. As such, a single propagating skew ray propagates along an optical fiber following a helical path as shown in Figure 14.

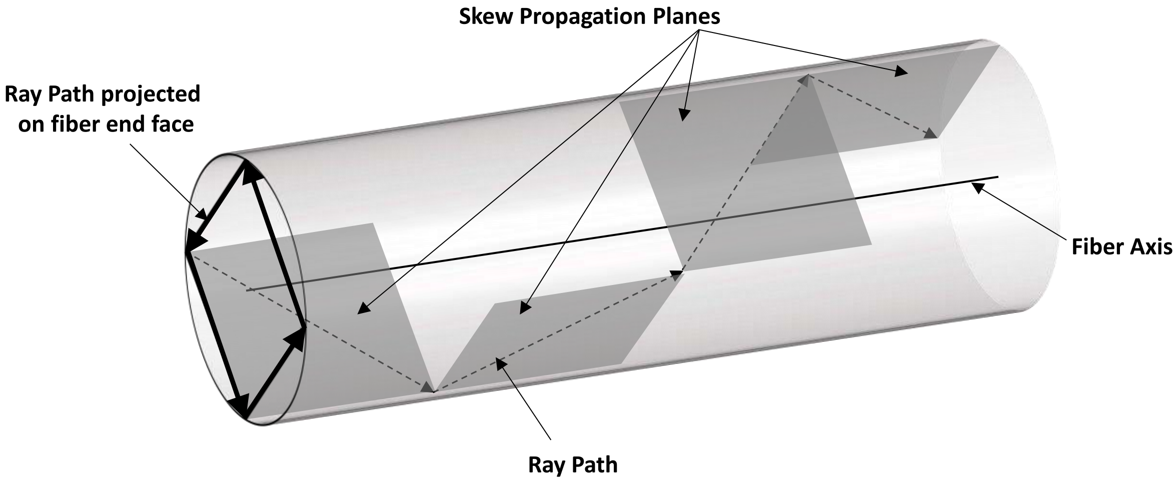

Figure 14: Ray optics representation of a skew ray propagating through an optical fiber. For clarity, only the fiber core is drawn. Skew rays propagate along different propagation planes after each reflection. However, each plane has the same skew angle as defined in Figure 15.

As a result of following a helical path through the fiber core, skew rays are not contained within a unique propagation plane after each successive reflection from the cladding interface. Instead, rays propagate along a family of propagation planes that are defined by a specific skew angle. The skew angle of the plane is defined by the angle that the propagating plane makes with a radial line of the fiber core as illustrated in Figure 15. This angle remains constant for a skew ray as it propagates along the fiber core. As a result of the constant skew angle, the minimum distance that the skew ray attains from the fiber axis is constant between successive reflections with the cladding interface.

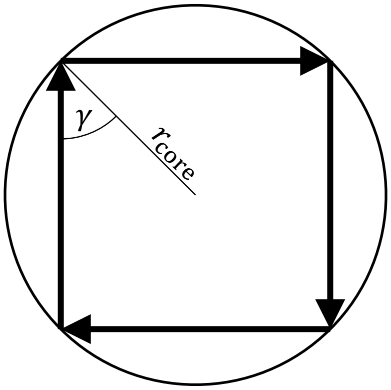

Figure 15: Schematic representation of the angle of the skew propagation plane of a skew ray.

Propagating rays which do not intersect with the optical axis of the fiber slightly modified cross sectional projection from that of meridional rays described in Figure 13. Because skew rays propagate away from the fiber axis, they travel a smaller distance between successive reflections than meridional rays. While the propagation plane between successive reflections of skew rays changes, the symmetry of constant skew angles can be used to create an equivalent two-dimensional schematic of skew rays similar to that meridional rays shown in Figure 13. Figure 16 shows the equivalent two-dimensional propagation of skew rays within a fiber core. As mentioned, the family of propagation planes maintain a symmetry that can be utilized the visualize the ray propagation along a single place so long as the appropriate modifications to the TIR angle and perpendicular distance are met. Within the skew plane, the perpendicular distance between the successive reflections at the cladding interface is reduced by the cosine of the skew angle.

The presence of a skew angle to rays propagating within a fiber core adds complexity to the analysis of reflection of the ray at the core cladding interface. Recall that the angle of incidence of meridional rays at the core cladding interface is only influenced by the angle of entry of the ray from the fiber end face. In contrast, the angle of incidence at the core cladding interface of skew rays is a function of both the angle of entry of the ray into the fiber end face and the skew angle of the ray. In Section 3.2.3 below, it is shown that the skew angle is directly determined by the position on the fiber face that the ray strikes from the light source.

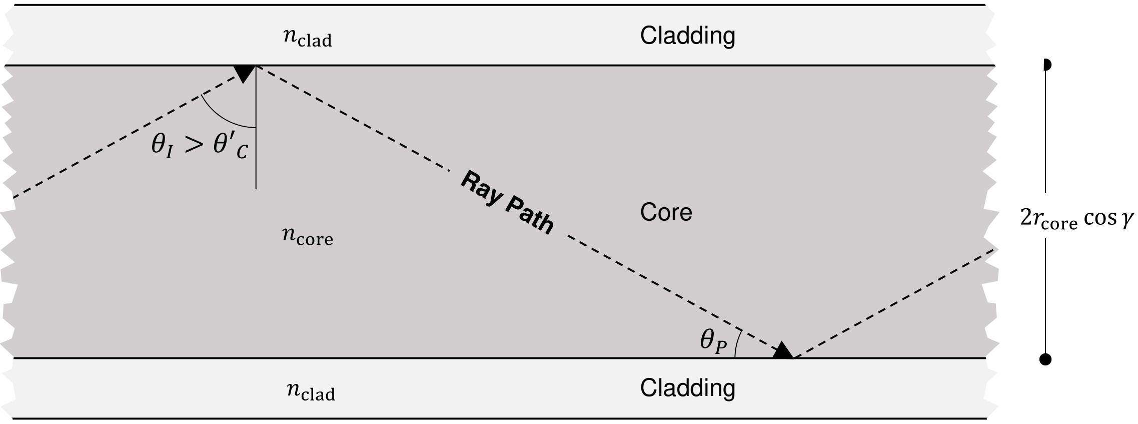

Figure 16: Skew ray planar propagation through a step index multimode fiber. Propagation of the meridional ray is dependent upon the condition that the angle of incidence $\boldsymbol{\theta_I}$ is greater than the critical angle for TIR of skew rays defined in Eq.(15).

Having the angle of incidence of skew rays depend on the skew angle of the ray, requires a modification to the critical angle equations for light rays bound to the fiber core. In order for the skew rays of the two-dimensional schematic in Figure 16 to remain within the fiber core, the critical angle necessary for TIR must depend on the skew angle of the ray. As such, the modified critical angle necessary for TIR which includes the description of skew rays is given by [15]:

$$\theta'_c = \arcsin\left\{\frac{n_{\text{clad}}}{n_{\text{core}}\cos\gamma}\right\}. \tag{15}$$

This new TIR equation reverts to the original of Eq.(14) when the skew angle of the ray is set to zero. Also note that the presence of the skew angle in the modified TIR equation changes the planar crictial angle (θ'_C). Such that the in plane angle of incidence (θ_I) of a skew ray required for maintaining TIR increases with increasing skew angle. Thus, skew rays are forced to propagate along the fiber with smaller in plane propagation angles (θ_P) than are allowed for meridional rays.

3.2.1.1 Acceptance angle of a fiber

As mentioned in the previous section, rays propagating within an optical fiber core are confined to propagate at angles that ensure TIR at the core cladding interface is met. A result of this condition is that optical fiber are only capable of receiving incoming light from a source at certain angles. Considering an optical fiber with core and cladding indices n_{core}, n_{clad} respectively, the propagation angle of a ray within the fiber must be $\theta_P < (90 - \theta_C)$ to ensure that the ray remains bound to the fiber core as a consequence of Eq.(15).

Given light entering the optical fiber through the fiber face at an angle θ_{ext} from an external environment of refractive index n_{ext}, the refracted ray entering the fiber will have a propagation angle given by:

$$\theta_P = \arcsin\left\{\frac{\sin\theta_{ext}\, n_{\text{ext}}}{n_{\text{core}}}\right\}. \tag{16}$$

Eq.(16) holds in the case of a meridional ray. The more general case involving skew rays will be tackled in Section 3.2.3. From the conditions on the propagation angle given by Eq.(15) and the angle of the refracted ray defined by Eq.(16) the boundary conditions on the external incident angle θ_{ext} are determined as:

$$\max(\theta_{ext}) = \text{asin}\frac{\left(n_{core}^2 - n_{clad}^2\right)^{1/2}}{n_{ext}}. \tag{17}$$

Therefore, those rays which are incident at the fiber face with an angle less than $\max\theta_{ext}$ will totally internally reflect at the core cladding interface. Considering the case where the external environment is air, then $n_{ext} = 1$ and Eq.(17) can be used to define the numerical aperture (NA) of a step index fiber for meridional rays as:

$$NA = \sin(\max(\theta_{ext})) = \left(n_{core}^2 - n_{clad}^2\right)^{1/2} \simeq n_{core}\sqrt{2\Delta} \tag{18}$$

Where $\Delta = \frac{n_{clad} - n_{core}}{n_{core}}$, is the index difference. The NA is a dimensionless quantity less than 1, which typical values ranging from 0.14 to 0.5. Since the NA is related to the maximum acceptance angle of the fiber, it is commonly utilized to describe the light gathering capability of a fiber and to calculate the source-to-fiber optical power coupling efficiencies [70].

3.2.1.2 Waveguide conditions on rays

The propagation of light within an optical fiber is dependent upon satisfying the conditions for TIR defined within the previous section. Under the guidelines of maintaining TIR at the core cladding boundary it would appear that any rays propagating along the fiber with incident angles greater than the critical angle θ_C for meridional rays, and θ'_C for skew rays. However, simply considering the reflection conditions of rays neglects the effects of phase of the plane wave associated with the individual ray. Accounting for the phase of the ray and the resulting interference that can occur after multiple reflections, it is seen that only rays at certain discrete propagation angles less than or equal to the critical angle are capable of propagating along the fiber without succumbing to destructive interference.

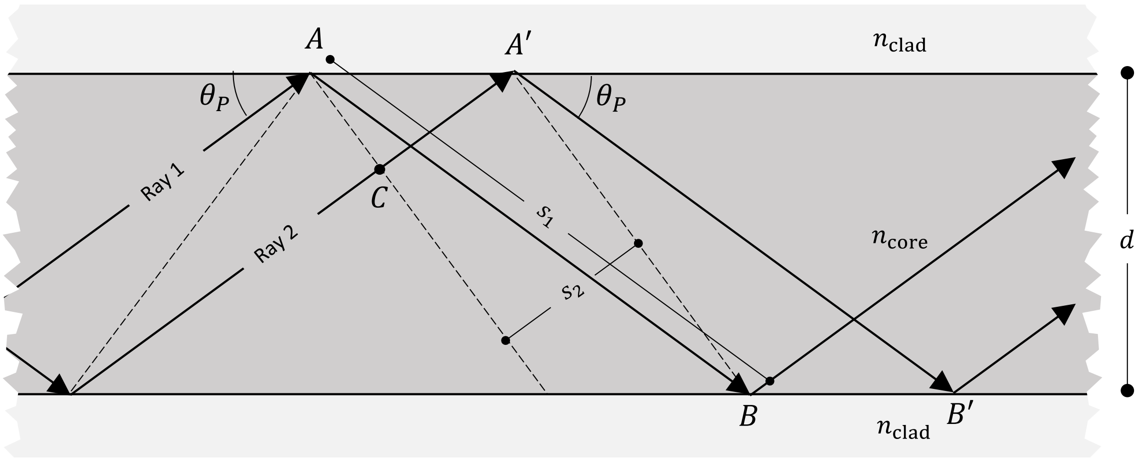

Figure 17: Light rays propagating within a fiber core. In order for propagation to occur, the angle of propagation (θ_P) must ensure that the distances s_1 and s_2 are phase matched.

In order to understand the effect of self-interference that can occur for a light ray propagating within a fiber core, the simple geometry outlined in Figure 17 is considered. The two rays incident at point A and A' are defined by the time varying wave function:

$$A(\vec{x},t) = \hat{e}_i A_0 e^{j(\omega t - \vec{k}\cdot\vec{x})}. \tag{19}$$

Where, $\vec{x} = x\hat{e}_x + y\hat{e}_y + z\hat{e}_z$ is the position vector, $\vec{k} = k_x\hat{e}_x + k_y\hat{e}_y + k_z\hat{e}_z$ is the wavenumber, and ω is the angular frequency of the light. As a light ray propagates within the fiber core, it undergoes a phase shift δ defined by:

$$\delta = \frac{n_{core} 2\pi s}{\lambda} \tag{20}$$

Where, s, and λ, are the distance travelled by and wavelength of the ray. In addition to the phase change resulting from the propagation of the ray, when light is totally internally reflected, it also undergoes a phase change. The phase change is a function of the angle of incidence of the ray, the polarization, and the relative refractive indices of the two interfacing media given by:

$$\delta_N = 2\,\mathrm{atan}\left(\frac{\sqrt{n^2\cos^2\theta_P - 1}}{n\sin\theta_P}\right), \tag{21}$$

$$\delta_P = 2\,\mathrm{atan}\left(\frac{n\sqrt{n^2\cos^2\theta_P - 1}}{\sin\theta_P}\right). \tag{22}$$

Where, $n = n_{core}/n_{clad}$ is the ratio of the core and cladding refractive indices, and the subscripts N, P represent the appropriate polarization. Given this understanding of the phase progression of a light ray propagating within a fiber core, and the schematic of Figure 17 the conditions on the propagation angle θ_P can be found. From the rays in Figure 17, the point A, before a reflection, and the point C share the same wave front and thus are in phase. Similarly, the point A' before reflection is in phase with the point B after reflection. Defining the distances s_1 and s_2, note that ray 1 travels the distance s_1 from point A to point B, while ray 2 travels a distance s_2 from point C to point A'. As mentioned since points A and C share the same wave front as do points A' and B, the distances s_1 and s_2 must differ but an integer number of 2π to ensure that the rays do not destructively interfere as they move along the fiber core.

The distances s_1 and s_2 is defined using:

$$s_1 = \frac{d}{\sin\theta_P} \tag{23}$$

$$s_2 = \frac{(\cos^2\theta_P - \sin^2\theta_P)d}{\sin\theta}. \tag{24}$$

Note that the expressions for s_1 and s_2 are completely independent of the distance AA', and remain solely a function of the core diameter and the propagation angle θ_P. Knowing that the phase change undergone by ray 1 as it reflects at point A and B, while travel from A to B, is given by:

$$\varphi_{s_1} = \frac{n_{core}2\pi s_1}{\lambda} + 2\delta_{N,P}. \tag{25}$$

Similarly, the phase change corresponding to ray 2 traveling from point C to A' without undergoing a reflection is:

$$\varphi_{s_2} = \frac{n_{core} 2\pi s_2}{\lambda}. \tag{26}$$

Therefore, by imposing that φ_{s_1} and φ_{s_2} must differ by an integer of 2π, so that:

$$\varphi_{s_1} - \varphi_{s_2} = 2m\pi \ m \in \mathbb{Z}. \tag{27}$$

Using Eqs. (20) to (26)and simplifying gives us a final condition on the propagation angle of rays within the core of:

$$\frac{2\pi n_{core} d \sin\theta_P}{\lambda} + \delta_{N,P} = \pi m \ m \in \mathbb{Z}. \tag{28}$$

The implications of Eq.(28) are that the acceptable propagation angles for an optical fiber with a core diameter d, core index n_{core}, for a ray of wavelength λ, do not form a continuous set angles within the NA of the fiber. Instead, the allowed propagation angles within the fiber form concentric cones within the NA cone of the fiber. The ensemble of rays entering at a specific angle from the axis of the fiber gives discrete optical intensity distributions. These are called the modes of an optical fiber. Note that when the diameter of the core is large relative to the wavelength, the number of values of m that satisfies Eq. 17 increases. In the case where the diameter is orders of magnitude larger than the wavelength the discretization of the propagation angles becomes dense enough so that the allowed propagation angles can be considered a continuum when modelling the illumination conditions of the fiber. This fact will be exploited in Section 3.2.3.

In order to gain insight into the number of modes which are allowed to propagate in the optical fiber which will be used in the construction of the FOEWS, we solve for the integer solutions of Eq. (28) and present the results in Figure 18 below.

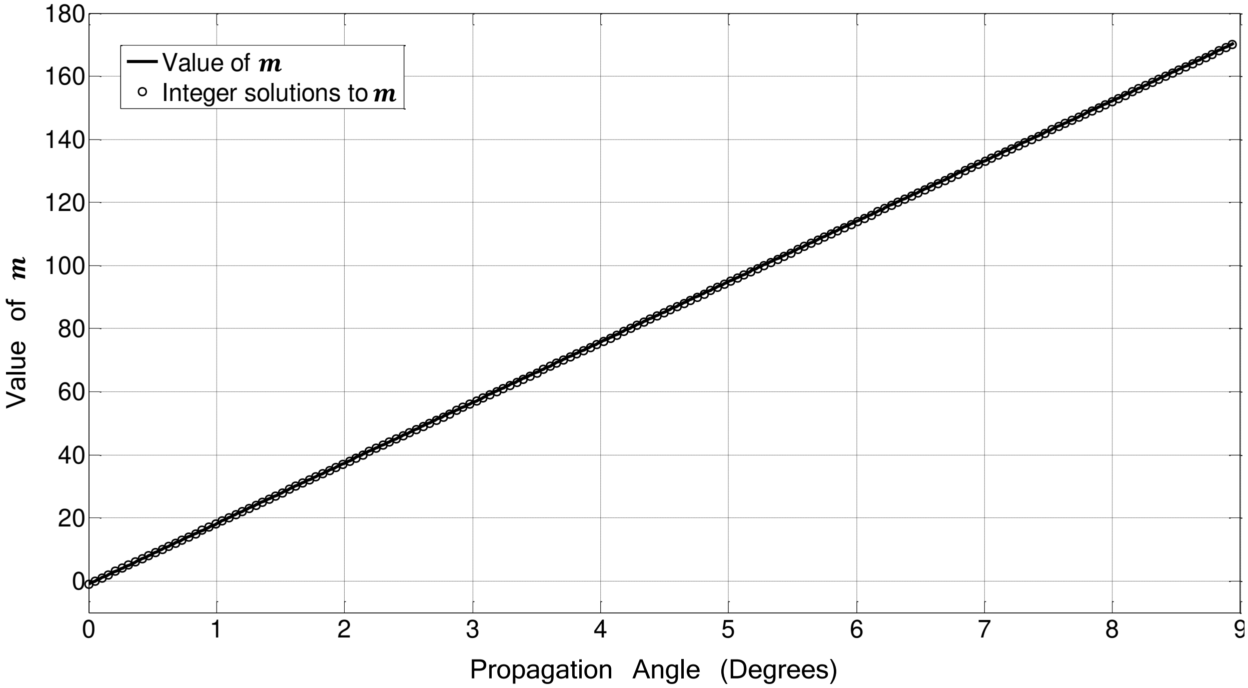

Figure 18: Plot showing the solutions to the mode condition of Eq. (28) for an optical fiber of numerical aperture 0.22, diameter of 105 μm, with a propagating wavelength of 0.85 nm. The solid line describes the value of m found while solving Eq. (28) while the circles highlight the solutions where $m \in \mathbb{Z}$ which correspond to allowable propagating modes. The optical fiber here allows for 172 propagating modes according to Eq. (28).

From Figure 18 we note that the optical fiber is capable of supporting 172 propagating angles or modes for a free space wavelength of 0.85 μm. Given that the propagating modes span less than 9°, on average a mode exists every 0.052°.

3.2.1.3 Fresnel reflection at the fiber end face

Section 3.2.1.1 showed that light incident on the fiber face is refracted into the fiber core following Snell's law. As with any ray incidence a portion of the ray power is transmitted through the refracted ray, while the remaining power is reflected back from the interface. In modeling the power transfer from an illumination source through a FOEWS onto a photo detector as illustrated in Figure 11, losses associated with fiber face reflections while minor can be considered.

Consider an incident ray from the illumination source incident onto the fiber end face as simple refraction between two semi-infinite media as illustrated in Figure 19.

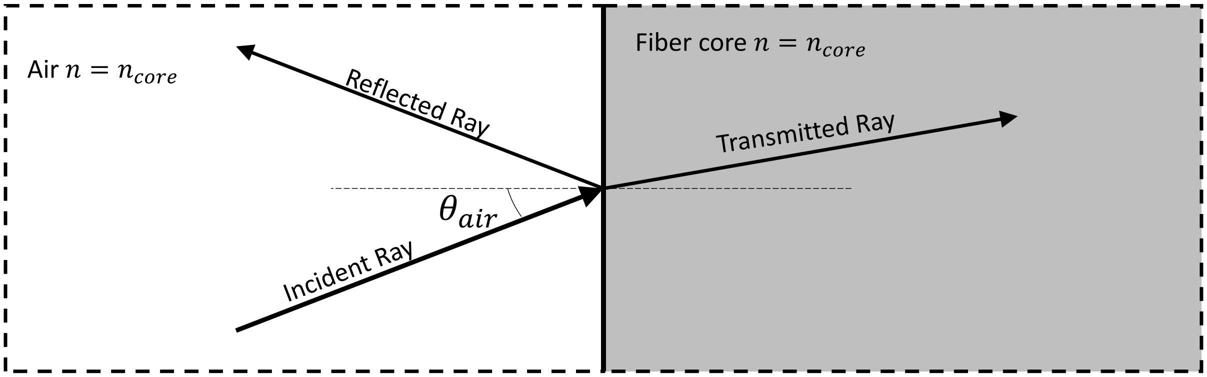

Figure 19: Schematic representation of a ray's transmission and reflection at the fiber end face governed by the Fresnel equations.

The angle of incidence (θ_{air}) is determined by the ray path from the light source onto the fiber face and will be discussed thoroughly in Section 3.2.3. Make note that at this point the resulting skew angle that the transmitted ray will have while propagating within the fiber core has no effect on the computation of the transmission at the fiber face. The transmission of the refracted ray into the fiber is calculated using the well know Fresnel equations given by:

$$t_p^2 = \frac{4n_{core}\cos(\theta_{air})\left(n_{air}^2 - n_{core}^2\sin^2(\theta_{air})\right)^{\frac{1}{2}}}{\left(n_{core}\cos(\theta_{air}) + \left(n_{air}^2 - n_{core}^2\sin^2(\theta_{air})\right)^{\frac{1}{2}}\right)^2}, \tag{29}$$

$$t_s^2 = \frac{4n_{core}n_{air}\cos(\theta_{air})\left(n_{air}^2 - n_{core}^2\sin^2(\theta_{air})\right)^{\frac{1}{2}}}{\left(n_{air}^2\cos(\theta_{air}) + n_{core}\left(n_{air}^2 - n_{core}^2\sin^2(\theta_{air})\right)^{\frac{1}{2}}\right)^2}. \tag{30}$$

Here the transmission equations for both polarization directions of the ray on the fiber face are written. Given that the resulting average of all rays incident on the fiber face will have an equally weighted polarization distribution and following the assumption of [15] the resulting estimation of the transmission coefficient of rays refracted into the fiber face will be given by:

$$t^2 = \left(t_p^2 + t_s^2\right). \tag{31}$$

3.2.1.4 Bulk attenuation loss

Although in principle optical fibers are designed to transmit light with little to no power loss, in practice, every optical fiber is less than one hundred percent efficient at transmitting light. Attenuation losses within an optical fiber are attributed to a combination of factors. Scattering losses due to imperfections of the fiber as well as bending losses cannot be completely modeled. Additionally, the inherent absorption coefficient of the core material combine to attenuate the power transport through the fiber that can be treated as a bulk attenuation coefficient. General specifications for a commercial optical fiber provide an attenuation coefficient which is meant to describe the general power loss associated to the fiber. The attenuation of an optical fiber is defined as the ratio of overall input to output transmitted power. The ratio of power loss is usually expressed as a logarithmic expression given by:

$$\alpha_{atten} = \left(\frac{10}{L_p}\right)\log_{10}\left(\frac{P_{in}}{P_{out}}\right). \tag{32}$$

Where L_p, is the total effective path length of a light ray propagating through the, while P_{in}, P_{out}, are the input and output power of the fiber respectively. For commercial optical fibers, the attenuation is expressed as decibels per kilometer (dB/km), as over smaller lengths, the attenuation can be very small.

The total effective path length of a light ray propagating through a fiber is a function of both the propagation and skew angles of the ray as defined above along with the radius and length of the fiber. In general, a ray traveling through an optical fiber of radius a, and length L, with a propagation angle θ_p and skew angle γ as illustrated previously in Figure 14 will have make a total number of reflections on the core cladding interface defined by [15]:

$$N = \frac{L\tan\theta_p}{2a\cos\gamma}. \tag{33}$$

The distance, L_i, travelled between successive reflections along a fixed skew plane is found to be:

$$L_i = \frac{2a\cos\gamma}{\sin\theta_P}. \tag{34}$$

With these two equations, total effective path length travelled by a ray propagating along the fiber is found to be:

$$L_p = NL_i = \frac{L}{\cos\theta_P}. \tag{35}$$

Note here that the total effective path length travelled is independent of the skew angle γ.

Two types of absorption dominate attenuation loss in an optical fiber. There are two types of absorption causes in a fiber, extrinsic and intrinsic. Intrinsic absorption is due to the material properties of the fiber materials. Silica glass fibers are the predominant type of optical fibers used. While silica glass has excellent optical transport properties, it does have a limited absorption characteristic depending on the wavelength of light. That is to say that given a pure sample of silica glass with no impurities or physical imperfections, light propagating through it would still experience a level of loss due to the inherent absorption properties of the material. The intrinsic absorption of a material define the transparency window over a specified spectral region. Intrinsic absorption results from electronic absorption bands in the ultra-violet region and from atomic vibration bands in the near infrared region [70].

Extrinsic absorption in optical fibers are caused by the presence of atomic impurities within the glass. The presence of OH (water) ion impurities in fabricated optical fibers are one cause extrinsic absorption. Water impurity concentrations of less than a few parts per billion are required it the attenuation is to be less than 20 dB/Km [70].

As mentioned the attenuation properties of an optical fiber both extrinsic and intrinsic, are provided within a specification datasheet from the manufacturer. For example, optical fiber which will be used in Chapter 4 is a high OH, step index multimode fiber product number SFS105/125Y obtained from ThorLabs. Within the datasheet a performance plot describing the attenuation behavior of the optical fiber with wavelength is provided.

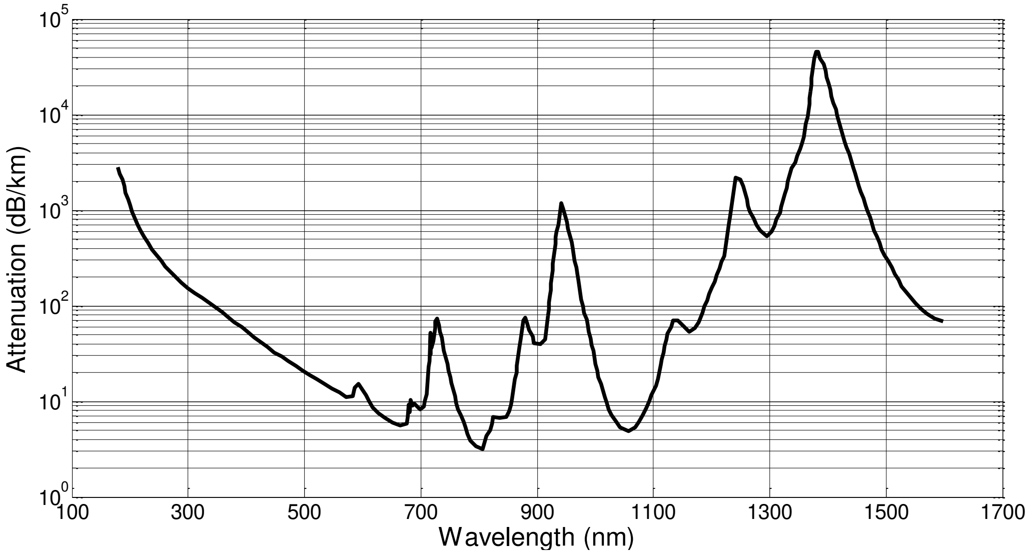

Figure 20: Performance plot for ThorLabs step index multimode fiber SFS105/125Y used in experimental results of Chapter 4 reproduced from [71]. The presence of the high absorption peaks at 1400, 950, and 725 nm, are a result of the high OH impurities present within the silica.

Figure 20 shows the attenuation performance for the ThorLabs step index multimode fiber SFS105/125Y reproduced from [71]. This fiber has a high presence of OH impurities and as such has large absorption peaks occurring at 1400, 950, and 725 nm. These are the first, second, and third overtones, respectively, of the fundamental absorption peak of water near 2.7µm [70]. The attenuation curve for the multimode optical fiber is incorporated directly into the model database and is used to evaluate the wavelength dependent bulk attenuation properties of the fiber.

In determining the power loss resulting from the attenuation properties of the optical fiber, Eq.(32) is re-written as:

$$\frac{P_{out}}{P_{in}} = e^{\alpha_{atten} L_p}. \tag{36}$$

Where, α_{atten} is the attenuation coefficient obtained from Figure 20 and expressed as a natural logarithm base.

3.2.1.5 Return internal reflection losses

As each ray propagates from the fiber input to output faces, it is subject to reflections at each interface. As a result a process of multiple reflections at the end faces occurs causing a loss in transmitted power. Intuitively, the loss of transmitted power by this phenomena is minimal and hardly effects the total transmitted power. However, its effects are included within the model for completeness.

The work of Messica et al. [15], derived an expression for multiple successive reflections at the fiber end faces by considering the simple illustration of Figure 21.

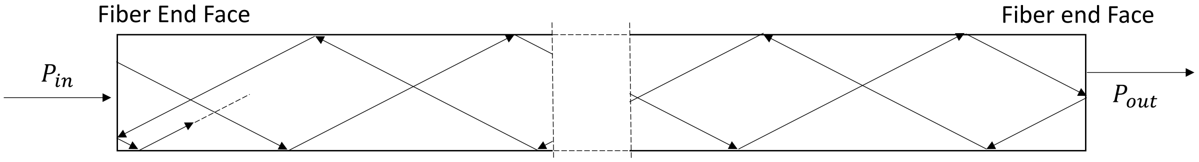

Figure 21: Schematic representation of multiple Fresnel reflections at the fiber end face as considered by Messica et al.[15].

Each ray propagating within the fiber undergoes bulk attenuation, as well as losses associated with attenuated reflections within the sensing region. Considering successive reflections on the fiber end faces, the resulting total power loss is given by [15]:

$$M(\theta,\gamma) = 1 - \left[r^4 (r_{sens}^2)^N e^{(\alpha_{atten} L_p)}\right]^2. \tag{37}$$

Here, r is the power reflected from both fiber end faces given by the reflection coefficients of the Fresnel equations given as:

$$r_p = \frac{n_{air}^2 \sin(\psi) - n_{core}\left(n_{air}^2 - n_{core}^2 \cos^2(\psi)\right)^{\frac{1}{2}}}{n_{air}^2 \sin(\psi) + n_{core}\left(n_{air}^2 - n_{core}^2 \cos^2(\psi)\right)^{\frac{1}{2}}} \tag{38}$$

$$r_s = \frac{n_{core} \sin(\psi) - \left(n_{air}^2 - n_{core}^2 \cos^2(\psi)\right)^{\frac{1}{2}}}{n_{core} \sin(\psi) + \left(n_{air}^2 - n_{core}^2 \cos^2(\psi)\right)^{\frac{1}{2}}} \tag{39}$$

For convenience ψ is used to denote the expressions:

$$\begin{gathered} \cos\psi = \sin(\theta)\cos(\gamma)\ ; \\ \sin\psi = (1 - \cos^2(\psi))^{1/2}. \end{gathered} \tag{40}$$

Where θ, and γ are the propagation and skew angles define above in Section 3.2.1. Again working with the assumption that $r^2 = \left(r_p^2 + r_s^2\right)$. The terms L_p and r_{sens} are the path length of the ray travelled through the fiber and the reflection coefficient within the sensing region of the fiber. Both of these terms will be defined in in the following sections.

3.2.2 Optical Tunneling in Thin Film Stratified Media

As will be discussed in Chapter 4, a FOEWS is fabricated through the partial removal of the cladding within a given length of an optical fiber. The partial removal of the cladding along a given length of the fiber reduces the thickness of the cladding material to less than the wavelength of the light propagating within the fiber.

When light is incident from a medium of high refractive index to a medium of lower refractive index, there exists an angle of incidence for which no light is able to transmit into the second media. This is the well-known phenomenon of TIR.

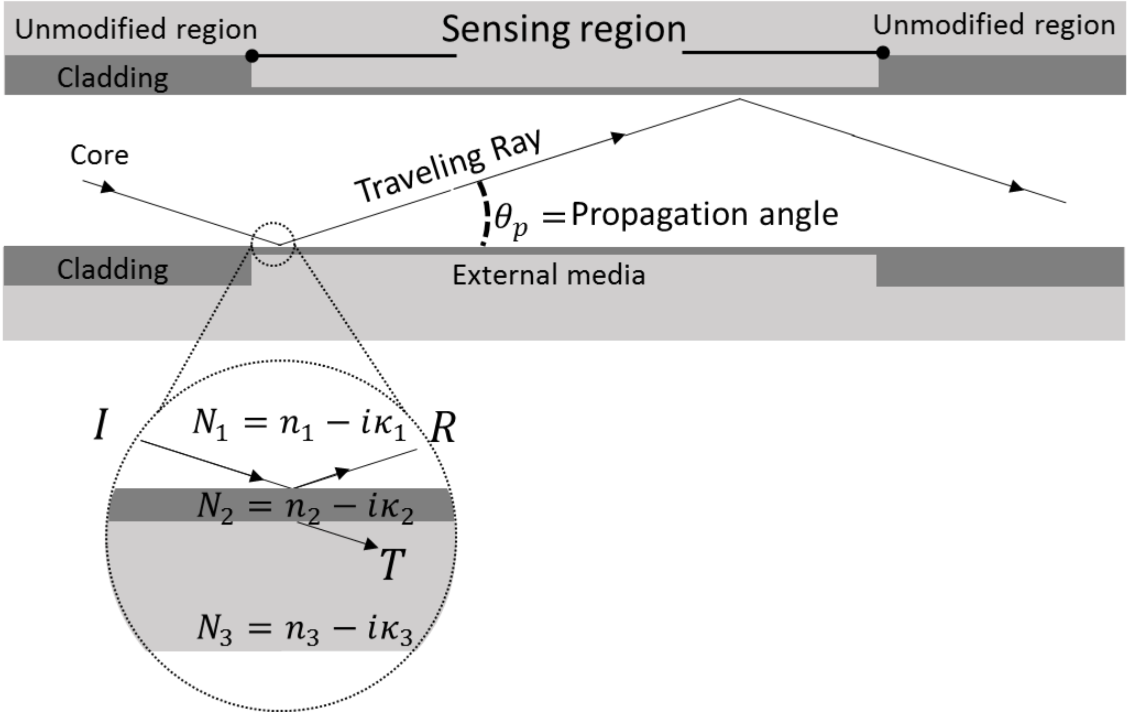

Figure 22: Schematic of the three layer stack present within the sensing region of the FOEWS.

3.2.2.1 Theoretical description of a three layer stack problem.

Under the framework of geometric optics, the analysis of a light ray incident at an interface between two media is analyzed considering only one interface regardless on the thickness of each layer. In other words, in a multi-layer stack geometry, each refraction calculation in geometric optics is considered as an independent phenomenon regardless of the geometry of the overall problem. This approach remains accurate so long as the thicknesses of the individual layers comprising the multi-layer stack is *optically large*. A dimension is considered optically large in relation to the wavelength of the light being analyze in the problem. In general, a distance that is an order of magnitude larger than the wavelength of interest, $(d > 10\lambda)$, is consider to be optically large.

In the case of a three layer stack problem where the second layer in the stack is on the order of or lower than that of the wavelength of interest, analysis using geometric optics fails to properly describe the physics of the problem. Consider the geometry of Figure 23 which illustrates the path a single incident ray travels through a three layer two interface geometry. Incident light onto interface a separating media one and two will both transmit through into the second media and reflect back into the first media following the Fresnel equations. The transmitted light continues through medium two and is eventually incident with media three at interface b. Whereupon the ray splits again partially transmitting into media three and reflecting back through media two. When the reflected light from interface b travels backwards towards interface a, it again reflects and transmits. This process continues infinitely, resulting in a need to compute an infinite sum of rays to determine the complete transmission of the initial ray through into medium three.

It is possible to solve for the reflection and transmission of the incident wave onto the two interphase media, by summing over the infinite series. This type of analysis was performed by recently by Buric et al. [16]. Wherein attempts to determine the reflection coefficient of a three layer stack in the sensing region of a fiber optic sensor were done utilizing the Fresnel equations

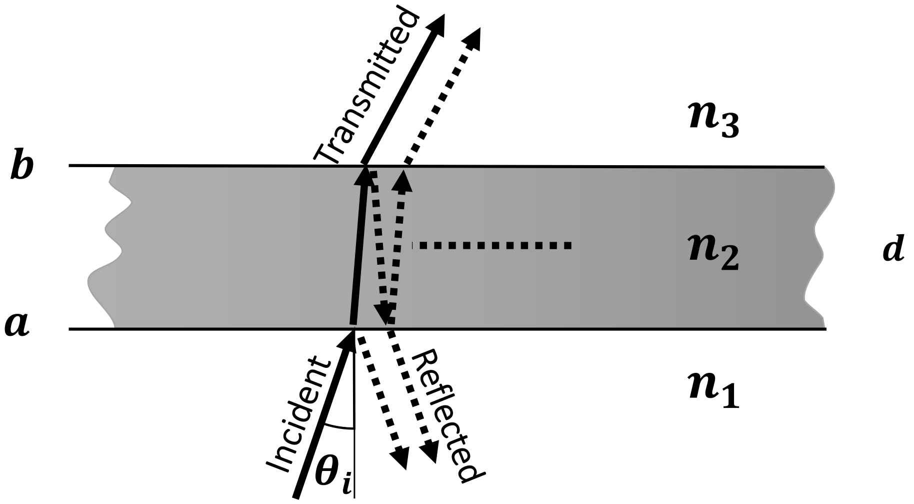

Figure 23: Infinite internal reflection of a two interface three layer system.

In Section 2.2 the use of alternative solutions to the two interphase system where discussed, which included the transmission line equivalency, as well as the transfer matrix method which was fully derived in Appendix A. Both the transmission line equivalency and the transfer matrix method provide a more efficient method for solving the transmission, and reflection of an incident electromagnetic field incident on a thin film stack.

3.2.2.2 Derivation of the reflection coefficient due to partial cladding

Figure 22 shows an overview of the geometry (not to scale) and analysis that is used to model a typical FOEWS. In the unmodified region of the sensor, both the core and cladding media are several wavelength thick. As such, the core cladding interface here can be considered as an interface between two half infinite spaces and the reflection coefficient can be found using the standard Fresnel equations without approximation. Because the IOR of the core is larger than that of the cladding, light rays propagating through the unmodified regions of the optical fiber experience TIR at the core cladding interface and remain unaltered by the external media.

In contrast, to the unmodified region, within the thin cladding region the thickness of the cladding is typically reduced to the order of one wavelength. With such a thin film separating the core from the external media the core cladding interface can no longer be accurately described by two half infinite spaces, but rather must be investigated as a thin film sandwiched between two infinite half spaces as shown in the circled region of Figure 22.

With the cladding thickness now on the order of one wavelength, light rays incident at the core cladding interface no longer undergo TIR, but instead some of the energy of the ray is allowed to "tunnel" through the thin cladding region resulting in a non-zero transmission coefficient in the external media. This kind of reflection at an interface is known as frustrated total internal reflection. The determination of the reflection coefficient in this kind of geometry can no longer be analyzed using the Fresnel equations, but instead the analysis is done by solving the Maxwell equations in each region and matching the boundary conditions at each interface.

While it is possible to explicitly solve the Maxwell equations for geometry present in Figure 23, a much more elegant and efficient method is the transfer matrix method. This method determines the transmission and reflection coefficient for any number of stratified layers by representing each layer of a stratified media as a matrix which is used to maintain the continuity conditions for the electric field across boundaries from one layer to the next. The full derivation of the transfer matrix method is given in Appendix A. Here the final resulting expression of the reflection coefficient at the core cladding interface, with cladding thickness t_{clad} and refractive indices n_{core}, n_{clad} and n_{media} for the core, cladding, and external media respectively with incident angle $\theta_I = 90 - \theta_P$ and free space wavelength λ is presented as [72]:

$$R = \left(\frac{\eta_{core}B - C}{\eta_{core}B + C}\right)\left(\frac{\eta_{core}B - C}{\eta_{core}B + C}\right)^{*}. \tag{41}$$

The asterisk, $*$, denotes the complex conjugate operation, while η_{core} is the wave tilted optical admittance defined as $\eta_{0_s} = n_{core}\sqrt{\frac{\epsilon_0}{\mu_0}}\cos\theta_i$ and $\eta_{0_p} = \frac{n_{core}\sqrt{\frac{\epsilon_0}{\mu_0}}}{\cos\theta_i}$ for s and p polarizations. The expressions for the coefficients B and C are given by:

$$B = \cos\delta + i\left(\frac{n_{media}}{n_{clad}}\right)\sin\delta \tag{42}$$

$$C = in_{clad}\sin\delta + n_{media}\cos\delta. \tag{43}$$

Finally, the variable δ is a function of the free space wavelength , λ_0, the incident angle $\theta_i = \frac{\pi}{2} - \theta_P$ and the thickness d of the cladding layer given by [73]:

$$\delta = \frac{2\pi}{\lambda_0} n_{clad} d \cos\theta_i. \tag{44}$$

Eq. (41) is the core expression that allows the overall model to account directly for both the thickness of the thin cladding layer and the optical properties of each of the three layers. It is this expression alone which is responsible for the change in optical response of the FOEWS due to the properties of the analyte media. Note that the expression is arrived at analytically, and does not assume any simplifications on the multiple internal reflections present in the cladding layer. The power of the TMM is that the full boundary value solution to the Maxwell equations for an incident plane wave on a multi-layer structure are solved simply with an iterative algorithm that can easily be translated to an efficient computer algorithm.

Methods and equations used to govern to transmission of light through a FOEWS based on the propagation and skew angles of the light ray entering the fiber face were derived. In the proceding section, the mathematical expressions required to establish the angular distribution and intensity of light rays entering a FOEWS from a typical LED illumination scheme will be given. Once the angular and intensity distributions are found, the full expression predicting the power output of a FOEWS is presented and used to analyze the effects of various input parameters on this power.

3.2.3 Illumination Conditions

The predicted response of a FOEWS using a ray based model relies heavily upon the angular distribution of rays propagating within the fiber. As demonstrated in Section 3.2.1, the propagation and skew angle of a ray within the fiber core characterizes the path a ray travels and the loss it experiences while traveling through the sensor. This model assumes that the optical fiber is perfectly straight so that variations in the propagation angle of rays due to bends in the fiber are not considered. The entirety of the angular distribution of rays propagating within the fiber model are determined by the launching conditions of light from the source onto the fiber face. As a result of this fact the predicted response of a FOEWS by the model relies as heavily on the appropriate description of the light incident onto the fiber face. The inherent dependence on the launching conditions on the predicted response of geometric optics based ray models of multimode optical fiber sensors is a known factor and has been studied by various authors namely [[15], [54], [1], [55], [74]]. Intuitively, it is known that larger propagation angle within the fiber core will result in more loss occurring at reflections within the sensing region of the fiber. The presence of more skew rays within a fiber core will also change the modeled response. Skew rays propagate near the exterior of the fiber core and as such, will experience a higher number of reflections within a given fiber length than a meridional ray. As a result, by increasing the proportion of skew rays in a modeled angular distribution an increase in sensitivity in the sensor performance due to the higher number of reflections within the sensing region would be expected.

The work of Gupta et al. [74], provided a general analysis of the effects of launching conditions on the evanescent absorption of a FOEWS utilizing a collimated He-Ne laser directly incident onto the optical fiber face. By varying the illumination angle of the laser beam onto the fiber face they investigated the in optical response of the sensor. They found an increase in the absorption efficiency occurred as the incident angle of the laser beam onto the fiber face increased. The increase in efficiency continued until the laser angle reached approximately 24° when the efficiency began to drop with increase angle. While the fiber used in the analysis had a numerical aperture of 9.8°, it was concluded that because the fiber has an overall short length (approximately 15 cm) it was able to still guide rays outside the NA of the fiber over that length. Upon reaching a launch angle higher than 24°, the loss due to poorly guided rays overcame the increase in efficiency of the high absorption of the rays within the sensing region leasing to a decrease in efficiency.

A more theoretical approach to the analysis of angular distribution of rays in a FOEWS was carried out by Messica et al. in [15]. The modeled the response of the FOEWS using some simplified launching geometries. Their geometry consisted of a parallel light source focus through a focusing lens onto the fiber optic end face at various tilt angles as illustrated in Figure 10. They also consider the illumination using a laser beam shoot directly at the fiber face. They concluded from these geometries that off centered spot illumination of the fiber face using a laser source excited only skew rays within the fiber.

The power outputs from a FOEWS of core cross sectional area can then be found by the power out integral defined at the onset of this chapter and repeated here for clarity as:

$$P_{out} = \int_S T\big(\theta_I(r,\varphi)\big) \cdot I(r,\varphi)\, dS. \tag{13}$$

Where the transmission $T\big(\theta_I(r,\varphi)\big)$ is the transmission loss function for a single ray passing through the FOEWS that was created from the combinations of Sections 3.2.1.1 to 3.2.2.2. While, $I(r,\varphi)$ represents the intensity of the light ray incident on the fiber face as a function of the source illumination conditions. The variables r, φ are the polar coordinate representation of the location on the fiber face as described in Figure 24.

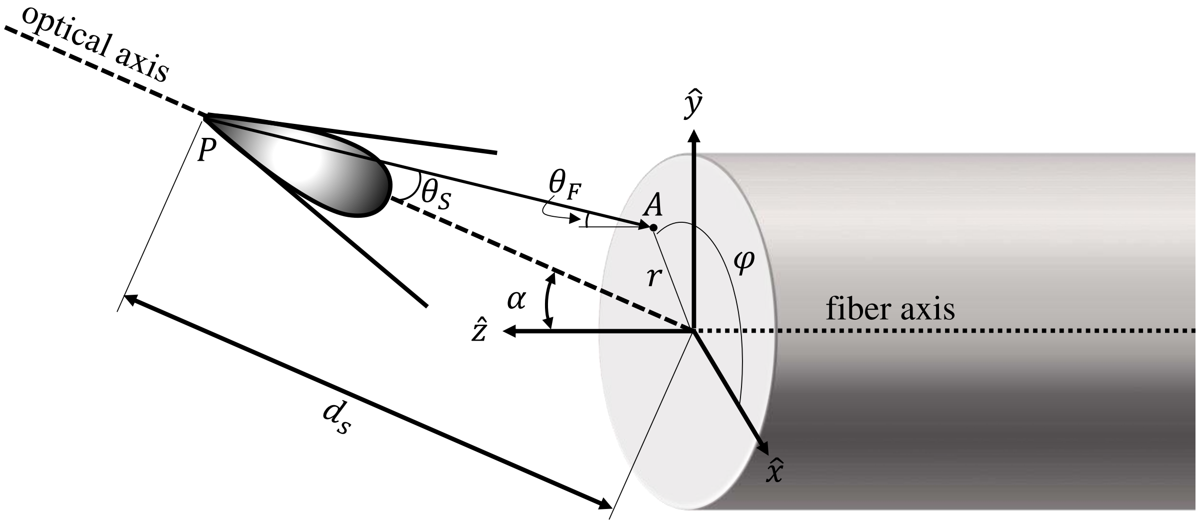

Figure 24: Schematic of the general launching conditions of a Lambertian LED source onto an optical fiber face at a tilt angle $\boldsymbol{\alpha}$.

Because the intensity and angular distributions of light rays is crucial in determining the power output for an FOEWS, it is assumed that the LED illumination scenario illustrated in Figure 24 is valid. As illustrated, a Lambertian LED source is placed a distance d_s away from the center of the fiber face so that the optical axis of the LED is at a fixed angle α with the fiber axis of the FOEWS. At a point (r, φ) on the fiber face the equations governing both the relative intensity of a ray striking the face as well as the angle of incidence between the striking ray and the fiber face are derived.

Without loss of generality, the tilt angle of the LED optical axis to the fiber axis in chosen to fall within the yz-plane. Variation in the tilt angle α and the source distance d_s represent all possible locations for the LED source. The choice of having the optical and fiber axes intersect at the fiber face, simplifies the computation of the intensity distribution of rays but has no bearing on the propagation or skew angle calculations.

The angular distribution of rays on the fiber face can be determined by calculating the angle between a ray along the vector $\overline{PA}$ to the normal vector $\hat{z}$ of the fiber face. The angle of a ray incident on the fiber source at a point (r, φ) is found to be [72]:

$$\theta_F(r,\varphi,\alpha) = \arccos\left[\frac{d_s\cos\alpha}{\sqrt{r^2 + d_s^2 - 2rd_s\sin\alpha\sin\varphi}}\right] \tag{45}$$

From Eq. (45) a description of the incident angle a ray traveling from a source makes with a given point on the fiber face as a function of the launching angle α is given. With the incident angle given at any point on the fiber face, the resulting propagation angle through the FOEWS can then be computed using Snell's law so that:

$$\sin\theta_P = \frac{n_{air}}{n_{core}}\sin\theta_F\ . \tag{46}$$

The propagation angle defined in Eq. (46) as a function of the IOR of the air and core, is the complementary angle to the incident angle that a ray propagating within the fiber core makes with the core cladding interface within the sensing region of the fiber. It is thus, the complementary angle $90 - \theta_P$ which is used to compute the reflection coefficient.

As mentioned previously, the skew angle of a ray propagating through the fiber core depends on the launching conditions of the light source. In the case where the LED source is placed on the z-axis, coinciding with $\alpha = 0$, there is no possibility for the excitation of skew rays through the fiber. When the tilt angle is increased certain rays propagating through the fiber core will have an associated skew angle.

The derivation of the skew angle of a ray incident from an LED source onto the fiber face is derived considering the projection of the ray's path in Figure 24 onto the fiber face surface. An illustration of the projection onto the fiber face is given in Figure 25. The skew angle γ of a ray emanating from an LED source at a point $P = (0, d_s\sin\alpha, d_s\cos\alpha)$, incident at any point $A = (r, \varphi, 0)$ on the fiber face, can be derived in general for an optical fiber with a core radius of r_c.

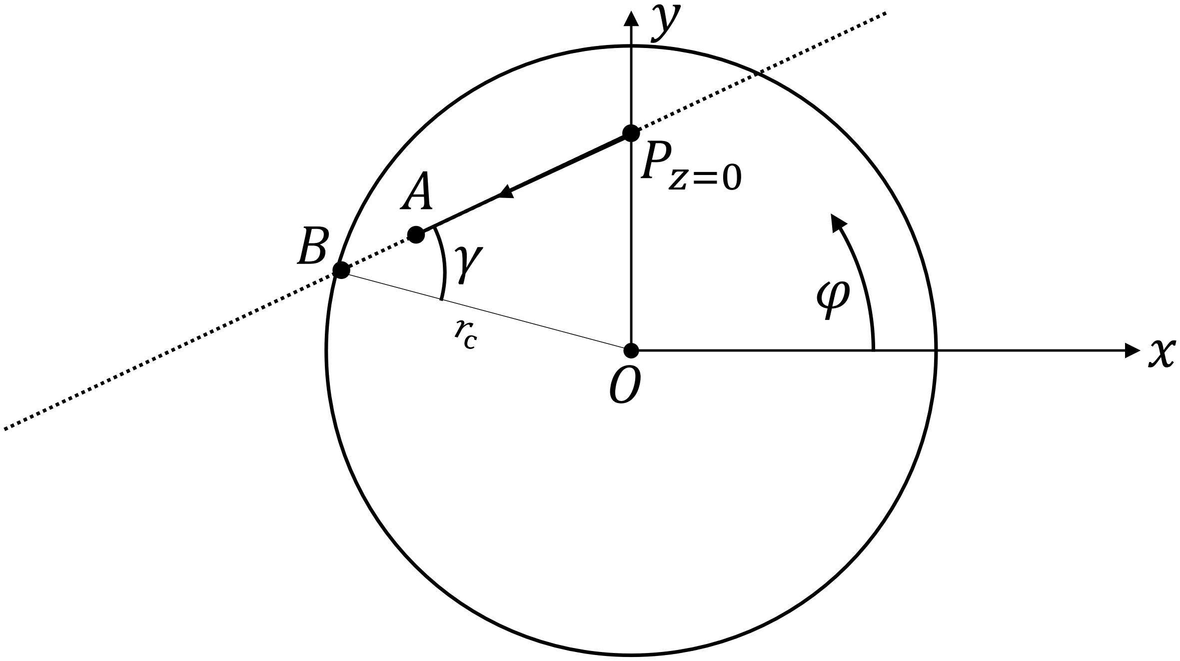

Figure 25: Schematic illustrating the projection along the z-axis of points of an incoming ray from an LED point source as in Figure 24, onto the fiber face. The incident skew angle is calculated as the angle between the lines through the points $B, A, P_{z=0}$, and a radial line of the fiber.

The vector defined by the points A and $P_{z=0}$, is given by:

$$\overrightarrow{AP_{z=0}} = (r\cos\varphi\,, r\sin\varphi - d_s\sin\alpha\,, 0). \tag{47}$$

Making use of the dot product, the angle made by the points, $A, P_{z=0}$, and the origin, is defined by:

$$\angle AP_{z=0}O = \arccos\left[\frac{\overrightarrow{AP_{z=0}} \cdot \overrightarrow{OP_{z=0}}}{\left\|\overrightarrow{AP_{z=0}}\right\|\left\|\overrightarrow{OP_{z=0}}\right\|}\right] \tag{48}$$

Finally, the incident skew angle γ is found by use of the sine law as:

$$\gamma = \arcsin\left[\left\|\overrightarrow{OP_{z=0}}\right\|\sin\frac{(\angle AP_{z=0}O)}{r_C}\right] \tag{49}$$

Unlike the incident angle θ_F which undergoes refraction upon entering the fiber core from the external environment; the skew angle γ is measured perpendicular to the plane of incidence and as such does not change when the ray enters the fiber core.

In addition to knowing the propagation and skew angles of any ray striking the fiber face from an illumination source, the intensity of that ray also plays a role in computing the response of the FOEWS. For an LED illumination source the intensity of light emitted depends on the angle from the emission axis. A standard LED will emit light as a Lambertian source. This means that the normalized angular intensity pattern of the LED follows the formula given by:

$$I(\theta_S) = \cos\theta_S. \tag{50}$$

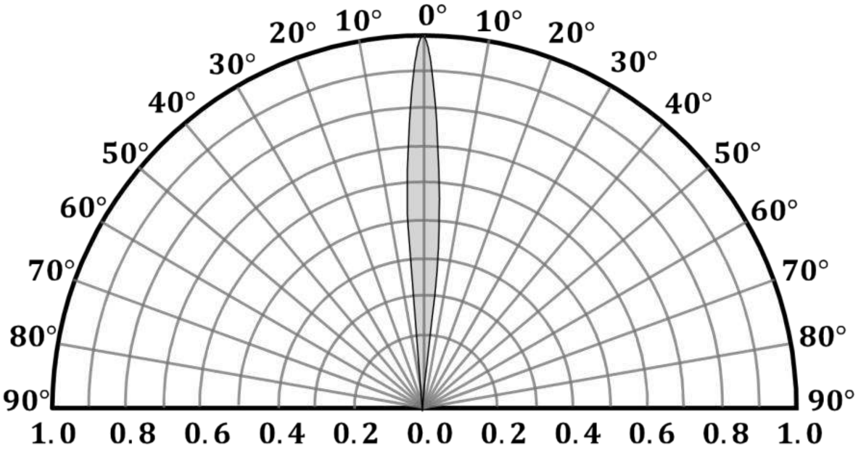

Figure 26: Angular intensity distribution of a Lambertian LED source with an emission width of 5°.

Where θ_S is the angle from the emission axis illustrated in Figure 24. For the applications of illuminating a fiber optic face with an LED in close proximity, having such a broad angular emission pattern results in the waste of power due to the small angular area of the fiber face. A better approach is to use a more directed LED emission pattern which directs light over a smaller angular range. By confining the LED emission to a limited angular range, a higher portion of the power from the LED strikes the fiber face. The angular emission pattern for a Lambertian LED with a 5° emission width is given in Figure 26. The normalized intensity formula for an LED with a 5° emission width is given by:

$$I(\theta_S) = \begin{cases} \cos(18\theta_S) \text{ for } 0 \geq \ \theta_S \geq 5 \\ 0 \text{ otherwise} \end{cases}. \tag{51}$$

3.2.4 Relative intensity of modes

With the setup for the FOEWS model complete, it is now possible to predict the relative loss for experienced for each propagating angle corresponding to the individual modes allowed to propagate within the FOEWS. Determining the relative loss of each mode in the FOEWS will allow us to determine which modes contribute the most to the power loss in the FOEWS. From Figure 18, we know that the optical fiber used to fabricate the FOEWS is capable of supporting 172 separate modes. In order to determine which modes are most important for sensing characteristics, we compute the relative transmission coefficient of each mode travelling through a FOEWS. For the purposes of this simulation, the FOEWS is assumed to have a sensing length of 1.5 cm with a cladding thickness of 0.2 μm. The simulation will assume that the analyte material has a refractive index of 1.7. The results for this simulation are presented below in Figure 27.

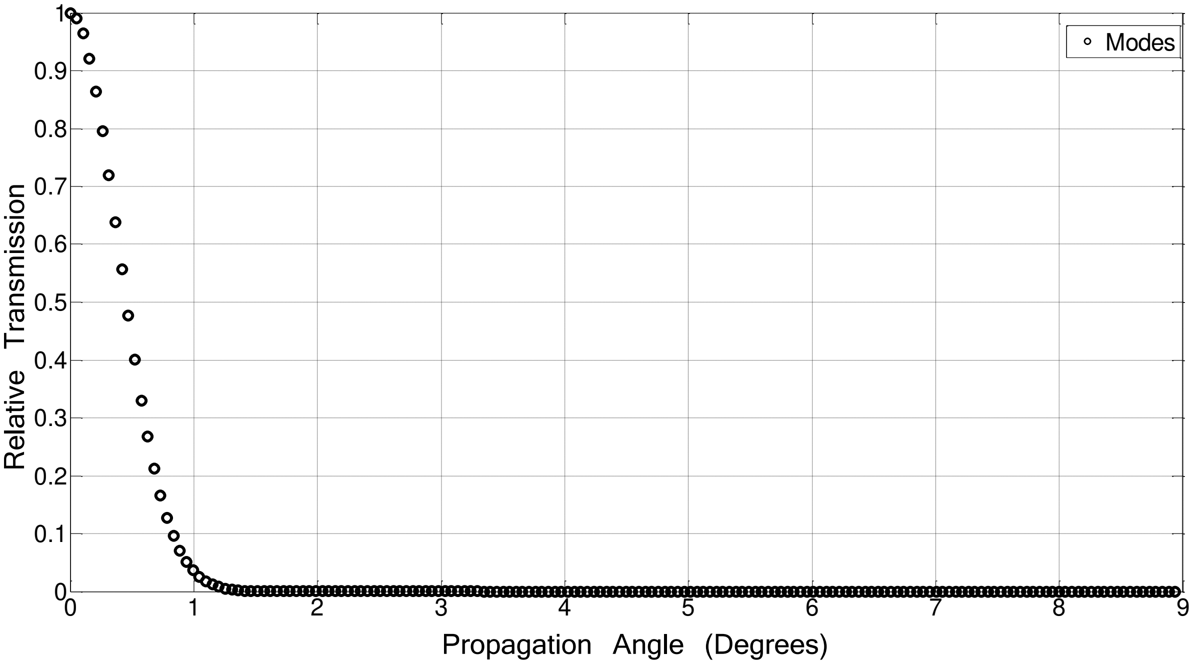

Figure 27: Plot of the relative transmission of each of the allowable propagation angles (172 modes) for a FOEWS of sensing length 1.5 cm, cladding thickness of 0.2 μm and in contact with an analyte of refractive index 1.7.

The results of Figure 27 clearly show that propagating angles greater than 1.2° are greatly attenuated while passing through the FOEWS. These higher order modes or propagating angles experience a greater number of reflections at the sensing interface making them the larger contributors to the signal loss. For completion the results of Figure 27 are represented using a log scale below in Figure 28.

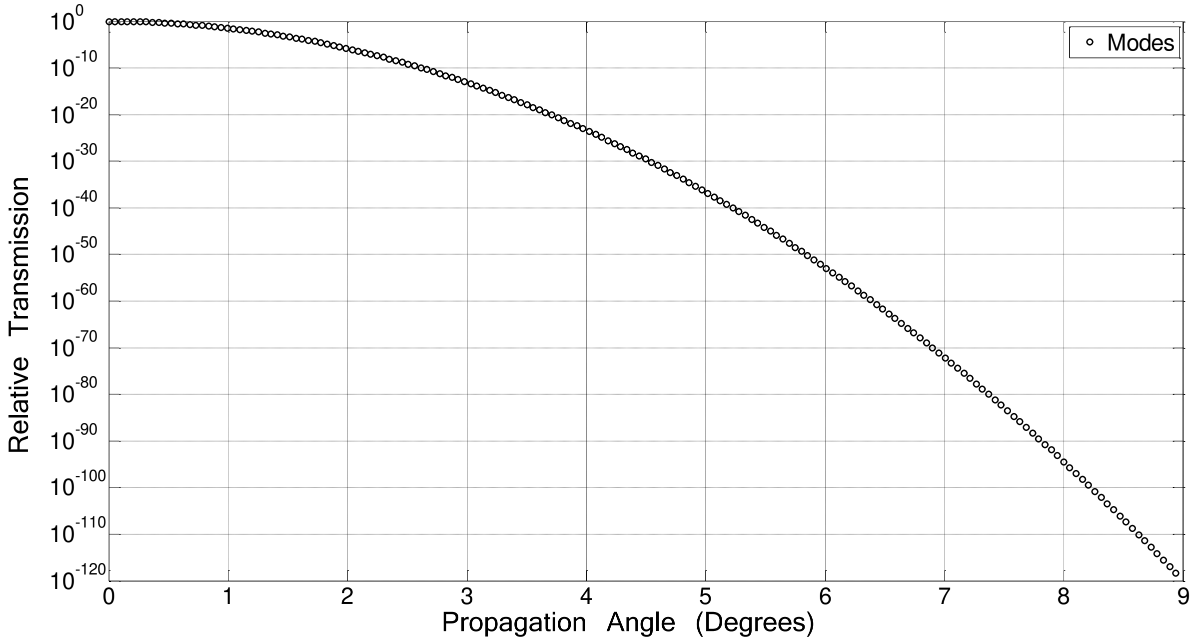

Figure 28: A second plot of Figure 27 using log scale.

Looking at the relative transmission coefficients in Figure 28 we note that propagation angles above 1.5° are effectively transmitting no power through the FOEWS having lost all power through sensing region. Given that the FOEWS works based on the power loss high loss modes are important. However, for the purposes of monitoring the change in refractive index of the external media, the change in output power from the FOEWS must be measured. Therefore, propagating modes must experience a high enough loss while passing through the FOEWS as a result of interacting with the external analyte while maintaining a high enough transmission coefficient in order to deliver enough signal to show variations in loss intensity based for different refractive indices of the analyte material. Also of importance is the number of rays which are sent through the FOEWS for each of the allowable modes. Based on the illumination conditions, not all modes will be equally populated with the same number of rays. The effects of illumination conditions of the FOEWS transmission response will be investigated later in Section 3.3.

3.2.5 Summary of FOEWS model

Within this chapter all the relevant equations used in predicting the response of a FOEWS were derived. As previously mentioned the final power output of the FOEWS is described by Eq. (13). To conclude the theoretical description of the model, the explicit forms of both the intensity and transmission functions are summarized.

The transmission function is explicitly defined by:

$$T(r,\varphi) = \frac{t^4 (R)^N e^{\alpha_{atten} L_p}}{M}. \tag{52}$$

Where t is defined as the loss associated with Fresnel reflections at the fiber end faces in Eq.(31), while R is the reflection coefficient at the sensing region thin film stack defined in Eq.(41). The expression $e^{\alpha_{atten} L_p}$ accounts for attenuation losses of a ray travelling along the fiber of attenuation α_{atten}, defined Section 3.2.1.4 with a total effective path length L_p derived in Eq. (35). Finally, the coefficient M accounts for the return internal reflection losses, and is defined in Eq. (37).

The intensity function $I(r,\varphi)$is given directly by Eq.(51), and like the transmission function relies on the input variables r and φ. As mentioned the power out integral defined in Eq. (13), is solved by discretizing the surface domain and replacing the integral with a double summation as:

$$P_{out} = \sum_i \sum_j \left\{ T\left(\theta_I\big(r(i),\varphi(j)\big), \gamma\big(r(i),\varphi(j)\big)\right) \cdot I\big(r(i),\varphi(j)\big) \right\} \Delta r_i \Delta \varphi_j. \tag{53}$$

The meshing of the fiber face surface is done in polar coordinates as illustrated in Figure 29. Each index pair (r_i, φ_j), corresponds to the simulation of a single ray being sent though the FOEWS.

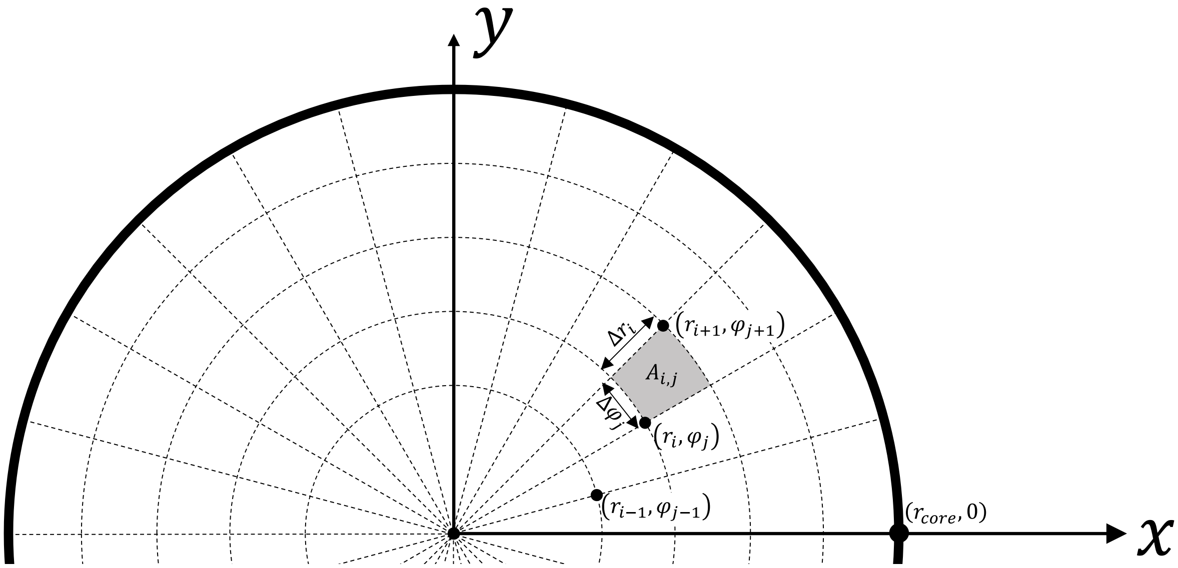

Figure 29: Polar meshing of the FOEWS illumination face used to discretize the surface of the fiber. Each node corresponds the simulation of a single rays passing through the FOEWS.

For a ray impacting at a point (r_i, φ_j) on the fiber surface there is an associated intensity described by the intensity function, $I(r, \varphi)$. In order to compute a power from the intensity function it must be multiplied by an area exposed to the intensity. In discretizing the fiber face domain, a finite number of rays are impacting the surface determined by the number of nodes of the mesh covering only one dimensional points on the surface. In order to assign an incident power to each ray, a two-dimensional surface element is associated to each ray. By assuming that the intensity of the ray at point (r_i, φ_j) uniformly covers a surface $A_{i,j}$ an incident power on the surface element is given by:

$$P_{i,j} = I(r_i, \varphi_j)A_{i,j}. \qquad (54)$$

The surface element $A_{i,j}$ corresponding to a node (r_i, φ_j) is defined as the surface with vertices (r_i, φ_j), (r_{i+1}, φ_j), (r_{i+1}, φ_{j+1}) and (r_i, φ_{j+1}) as illustrated in Figure 29. In general, the area of the surface $A_{i,j}$ is given by:

$$area(A_{i,j}) = \Delta r_i \Delta\varphi_j = r\Delta r\Delta\varphi. \qquad (55)$$

Meshing of the fiber face is done so with fixed division length of radius, Δr, and fixed angular division $\Delta\varphi$. The result of this fixed division meshing is that a larger number of rays are sent through the center region of the fiber face than at the edge of the face. However, care is taken to make sure that a large enough number of rays are simulated so that there is a high resolution meshing at the outer region of the fiber face to maintain accurate representation of the variance in intensity and angular distributions. For the simulation presented in the next section, the division length Δr and $\Delta\varphi$ are chosen as $1\ \mu\text{m}$ and 0.1 rad. This results in the simulation of $6\ 597$ rays onto the fiber face with a maximum element surface area $area\left(A_{i,j}\right) = 10.4\ \mu\text{m}^2$ which corresponds to $0.03\ \%$ of the entire fiber face size.

3.3 Response Predictions

Using the model described above, it is possible to theoretically investigate the expected change in response of a FOEWS under variations in cladding thickness, illumination conditions, and refractive index of the analyte material. By running several simulations under variations in these parameters, the following section attempts to draw conclusions about the significance each has on the expected optical response. The transmission response behavior of the FOEWS is given as a normalized power ratio instead of the absolute power output of the model. The signal is normalized to a reference power chosen as the output power of the FOEWS when exposed to air. From theory it is known that at analyte IOR values below the IOR of the core, no power is lost along the sensing region of the FOEWS and the output transmission is at a maximum. Normalization to the simulated transmission value at for air also provides a method for comparison with experimental results that will be useful in the following chapter. Under experimental conditions, determining the power transfer into the optical fiber from the LED source is not easily determined. In contrast, normalizing to the power output in air or any other analyte with a known IOR below that of the core is a simple and accurate baseline to take.

The following response predictions are conducted using certain assumptions for the input parameters of the model. The LED source is taken to be an ideal Lambertian emitter with an angular width of 5° that is incident directly on the fiber face without the use of focusing lenses. The optical fiber is assumed to have a core IOR of 1.455 with a NA of 0.22.

3.3.1 Cladding thickness

The thickness of the cladding within the sensing region of the fiber strongly effects the response behavior of a FOEWS. Figure 30 presents the change in relative power transmission for various cladding thickness ranging from 0.1 to $1.4\ \mu\text{m}$ on the sensing response to sample media with IOR ranging from 1.42 to 1.6 where the LED distance from the source is held at 1 mm with no tilt angle and a fixed sensing length of 1.5 cm. Only real IOR values for the analyte are chosen to investigate the behavior of the sensor to changes in the sensor response. The model is capable of simulating the effects of an absorbing analyte on the sensor response, but for the purposes of analyzing the effects of cladding thickness on sensor behavior, only non-absorbing analytes are considered.

Notice that for IOR values of the external media below that of the core, the relative power transmitted through the FOEWS remains constant. This is expected as tunneling through the thin cladding region requires the external analyte to have an IOR which would not support TIR within the core.

When the IOR of the external media is lower than that of the core, an evanescent field is produced from the incidence of rays at the core cladding interface. The evanescent field attenuates exponentially in amplitude away from the fiber core through the cladding and external media without carrying energy away from the core. When the IOR of the external analyte equals or is larger that of the core, the evanescent field within the cladding generates a propagating wave at the cladding external analyte interface which allows energy from the core to tunnel through the thin cladding and carry energy away from the fiber core. This phenomenon is sometimes referred to as optical tunneling and has been discussed extensively in the literature as mentioned in the literature review.

As the cladding thickness is increased the minimum relative power transmission. This is expected, since the evanescent wave attenuates less as the cladding thickness decreases, allowing less energy to be radiated from the core. Also of importance is the shape of the relative power curve with external IOR values. As the cladding thickness decreases, there is an increase in the transmission range of the FOEWS response. However, as the transmission range increases the transmission itself decreases, and for IOR of the analyte near minimum transmission the signal can become difficult to measure.

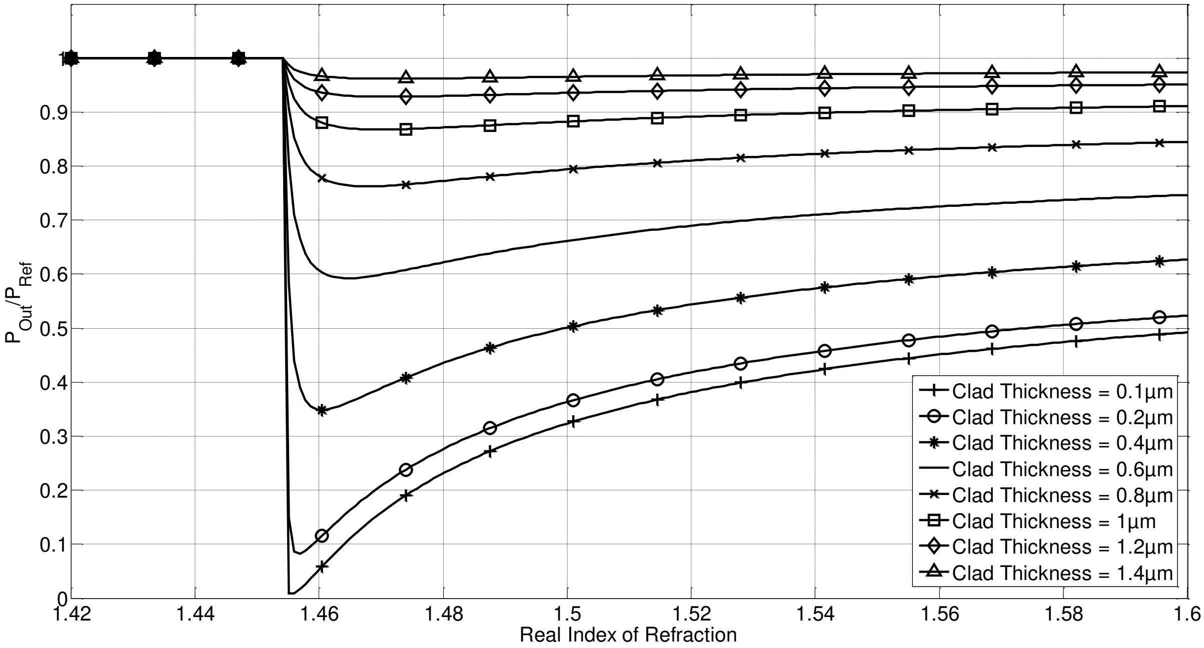

Figure 30: Predicted normalized power loss for sensors with cladding thicknesses from 0.2-1.6 µm in response to external media with IOR values from 1.42 to 1.6. LED illumination distance was held at 1 mm with zero tilt angle and a fixed sensing length of 1.5 cm.

The change in transmission range of the FOEWS as a function of cladding thickness is given by Figure 31. The transmission range is given as the measure of the drop in transmission signal from the reference power to the lowest transmitted power observed over the range of analyte IOR values. From the graph of Figure 31, the transmission range of the FOEWS as a function of cladding thickness demonstrate exponential behavior, and is reminiscent of the FTIR transmission through a thin film shown in Figure 4. The similarities between these graphs are due to the strong dependence of the FOEWS's transmission response on the reflection coefficient occurring within the sensing region of the fiber.

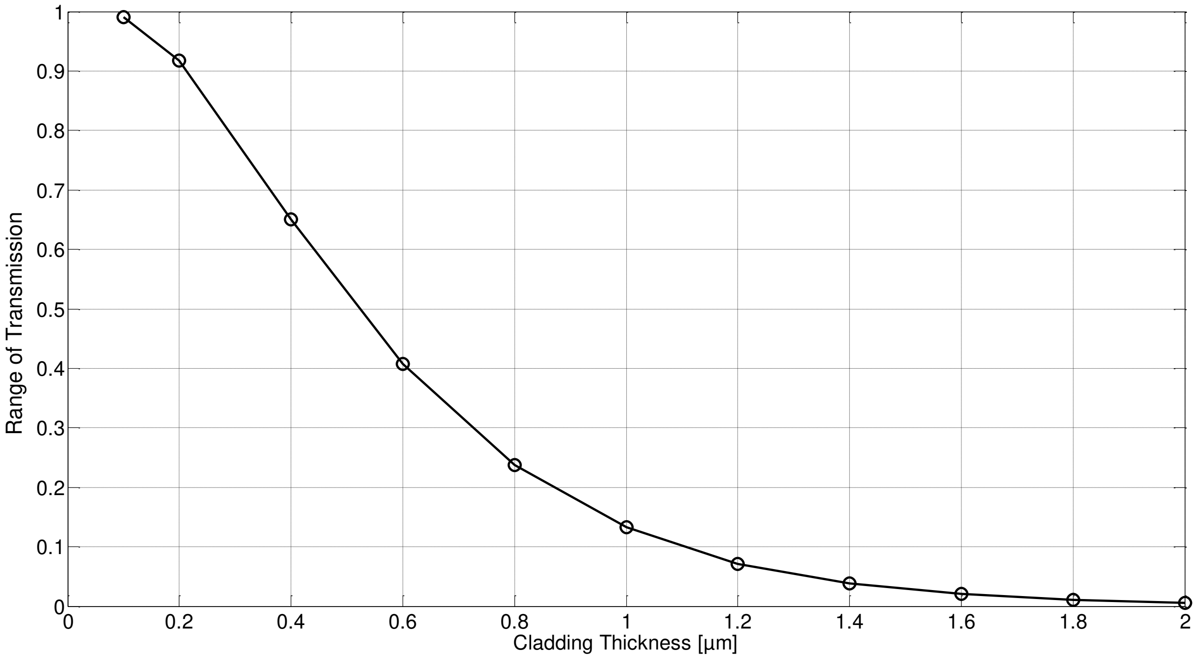

Figure 31: Prediction of the change in transmission range of the FOEWS response as a function of cladding thickness.

Also of note is the behavior of the IOR corresponding to the minimum transmission value of the FOEWS response. Figure 32 shows the predicted change in the corresponding IOR of minimum transmission as a function of the cladding thickness of the FOEWS. The IOR corresponding to the point of minimum transmission varies exponentially with cladding thickness. The shift in minimum transmission through the FOEWS is a consequence of the behavior of the reflection coefficient off a simple thin film as illustrated in Figure 23 with an incident angle of 1 degree. For clarity the shift of IOR corresponding to minimum reflection off a thin film as a function of film thickness is plotted alongside the IOR shift of minimum transmission of a FOEWS as a function of cladding thickness. The close agreement of the two scenarios is a result of the strong dependence of the FOEWS model on the reflection coefficient of the thin cladding interface.

This behavior can be exploited to more accurately determine the cladding thickness of fabricated sensors since it provides a relationship between cladding thickness and optical response without relying on the absolute transmission intensity of the fiber. The minimum transmission IOR of a sensor can easily be determined using calibrated thermo-optic liquids as will be seen in Chapter 4, where this behavior will be exploited to fit experimental results to simulated responses.

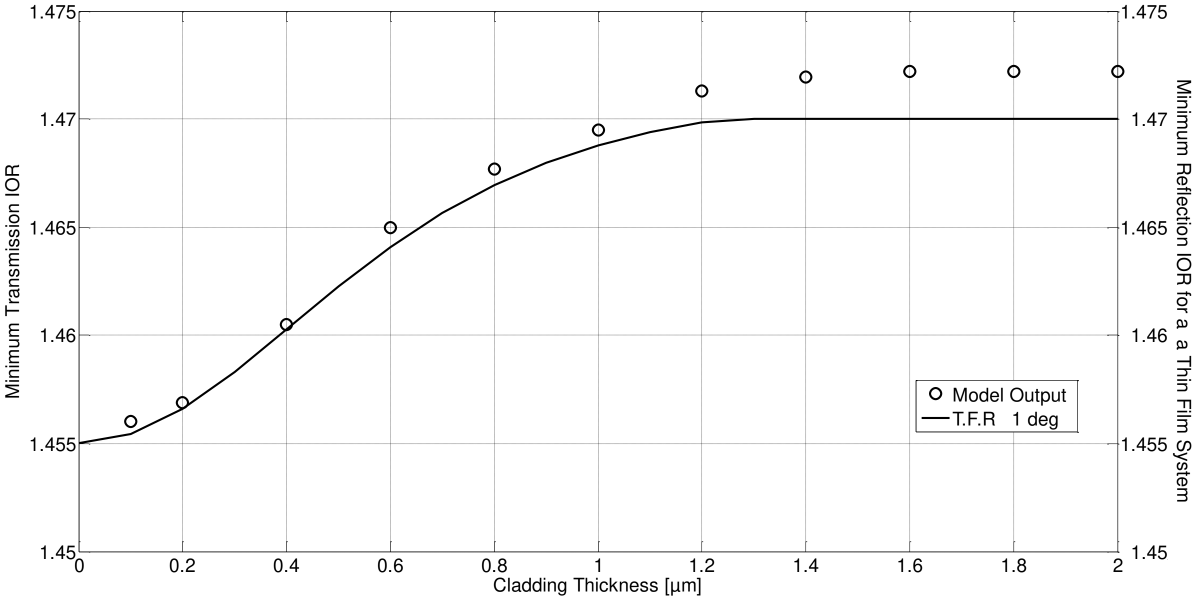

Figure 32: Prediction of the change in the minimum transmission index for various cladding thicknesses. Model results are compared to the shift in IOR corresponding to minimum reflection of a thin film structure, as in Figure 23, with an incidence angle of 1°.

3.3.2 Length of sensing region

In addition to cladding thickness as a fabrication design parameter, the length of the sensing region of the FOEWS can be adjusted depending upon the desired response characteristics. From the general formulation of the power output in Eq. (52) it is seen that the sensing length presents itself in the exponent term N. As such, the expected change in FOEWS response to a change in sensing length should follow a logarithmic behavior.

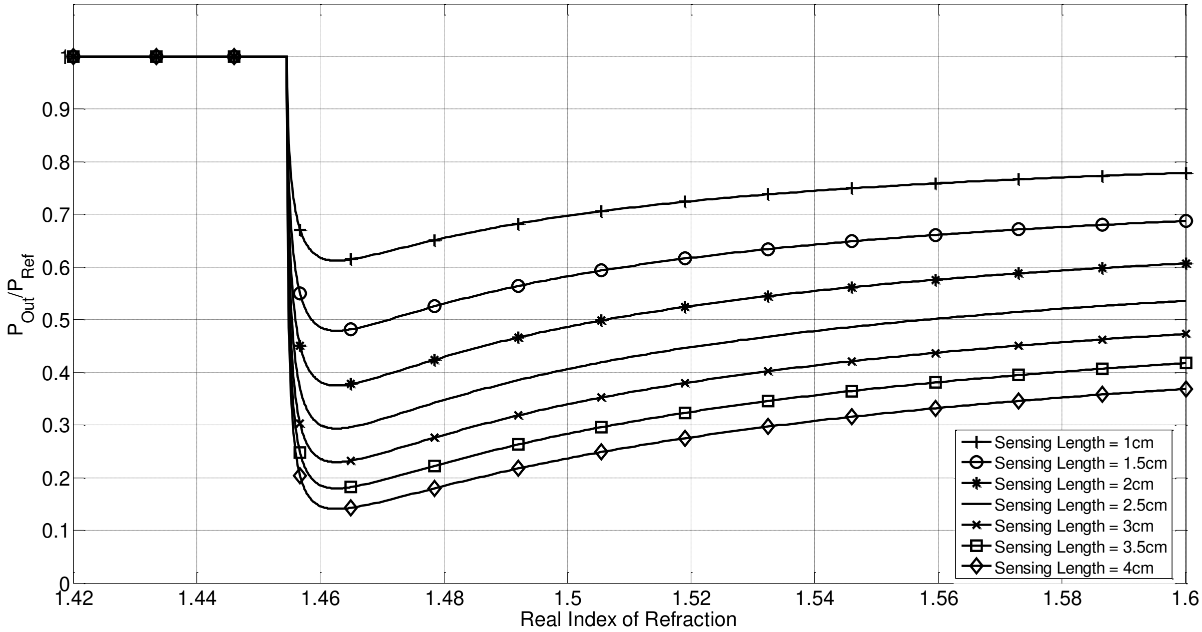

Figure 33: Predicted normalized power loss for sensors with change in sensing length from 1 to 4 cm in response to external media with IOR values from 1.42 to 1.6. Cladding thickness was held at 0.5 µm with zero tilt angle, and an LED launch distance of 1 mm.

Figure 33 shows simulation results for variations in sensing length ranging from 1 to 4 cm long. In these simulations, the cladding thickness was kept at 0.5 µm while the LED was held 1 mm with zero tilt angle. From the simulation results, increasing the sensing length results in an increase in transmission range as expected from the form of Eq. (52). Figure 34 shows the logarithm correlation between the sensing length and transmission range.

While changing the sensing length of the fiber increases the transmission range similarly to a decrease cladding thickness, the index of minimum transmission does not exhibit the same change in behavior. Figure 35 shows how the index of minimum transmission remains constant as a function of the sensing length of the FOEWS. Because of this behavior it is possible to adjust the transmission range of the FOEWS without changing the index of minimum transmission.

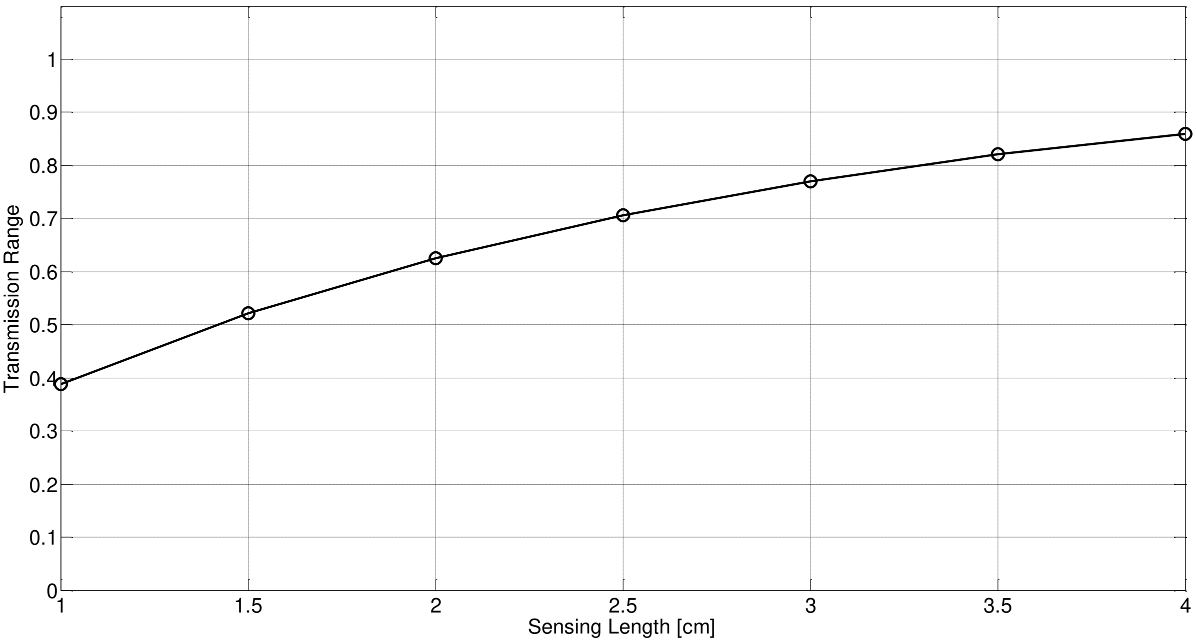

Figure 34: Predicted behavior of the transmission range measured in the fiber as a function of sensing length.

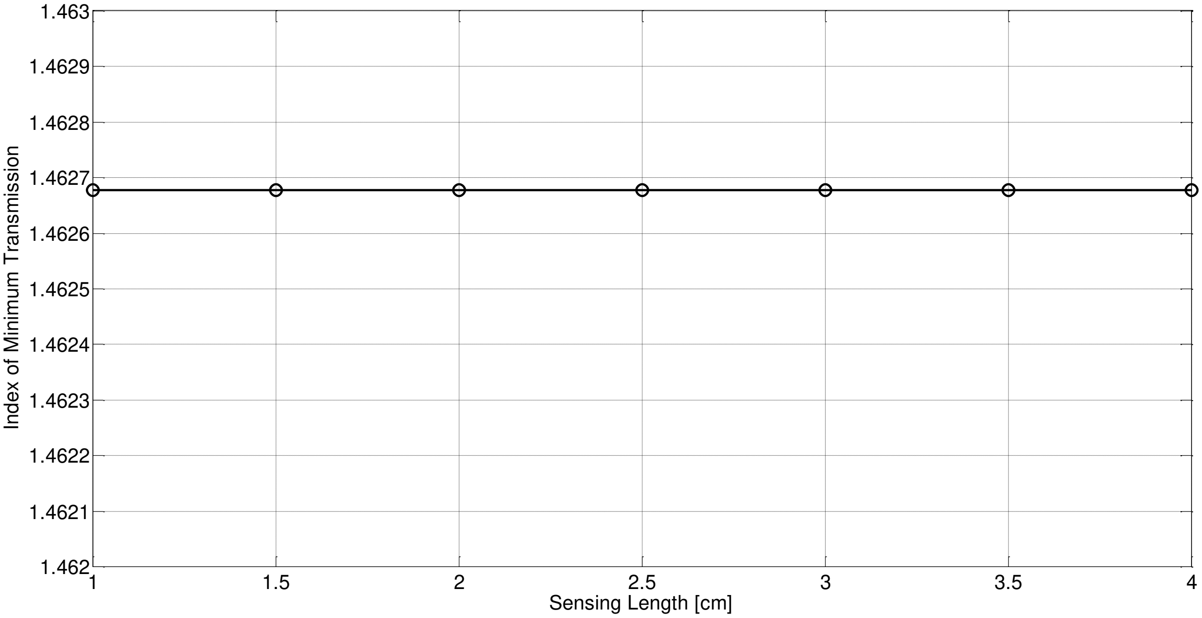

Figure 35: Predicted behavior of the change in the minimum transmission index as a function of sensing length. Unlike the phenomena seen with variation in cladding thickness, sensing length does not affect the minimum transmission index value.

3.3.3 Distance of LED to fiber face

In the preceding two sections the change in transmission response of a FOEWS predicted by the model as a function of the cladding thickness and sensing length of the fabricated fiber was investigated. Both of these parameters are functions of the etching process and remain fixed once the FOEWS is fabricated. In this and the following sections, effects of the launching conditions of the LED on the transmission response of the FOEWS are investigated. Unlike cladding thickness and sensing length, launching conditions can be changed after sensor fabrication. The launching conditions are modeled using the illumination equations derived in Section 3.2.3.

Figure 36 presents the change in relative power transmission for LED illumination distances ranging from 1 to 5 mm on the sensing response to sample external media with IOR ranging from 1.42 to 1.6 for a constant cladding thickness of 0.5 µm and no tilt angle. The predicted power transmission for the FOEWS maintains the same general shape as those shown in Figure 30. The increase in LED distance decreases the transmission power contrast for external media IOR values below and above the core IOR, so that for a launching distance very little signal variation with external media IOR is seen.

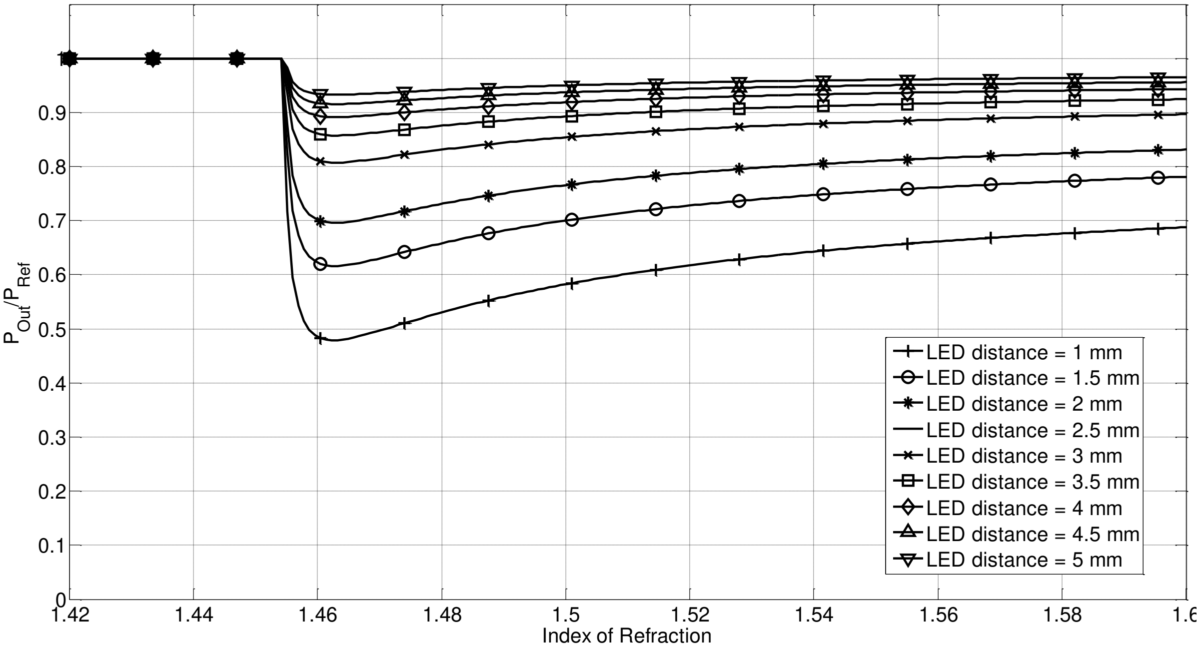

Figure 36: Predicted normalized power loss for sensors with distance of LED to fiber face from 1 to 5 mm in response to external media with IOR values from 1.42 to 1.6. Cladding thickness was held at 0.5 µm with zero tilt angle.

The LED source is assumed to emit light rays from a single point source in a Lambertian emission profile. Consequently, as the LED is place further from the fiber face, light rays incident of the fiber face impact at a smaller angles so that light rays travelling along the fiber core have a larger propagation angle. Light rays travelling at larger propagation angle are less frequently incident of the core cladding interface and additionally the reflection coefficient from high angle incidences is closer to unity. Therefore, less power is lost to the external media by the high propagation angle rays, reducing the transmission range for far distance illumination. The correlation between the launch distance and the transmission range is given in Figure 37. The transmission range decreases exponentially as the LED distance is increased.

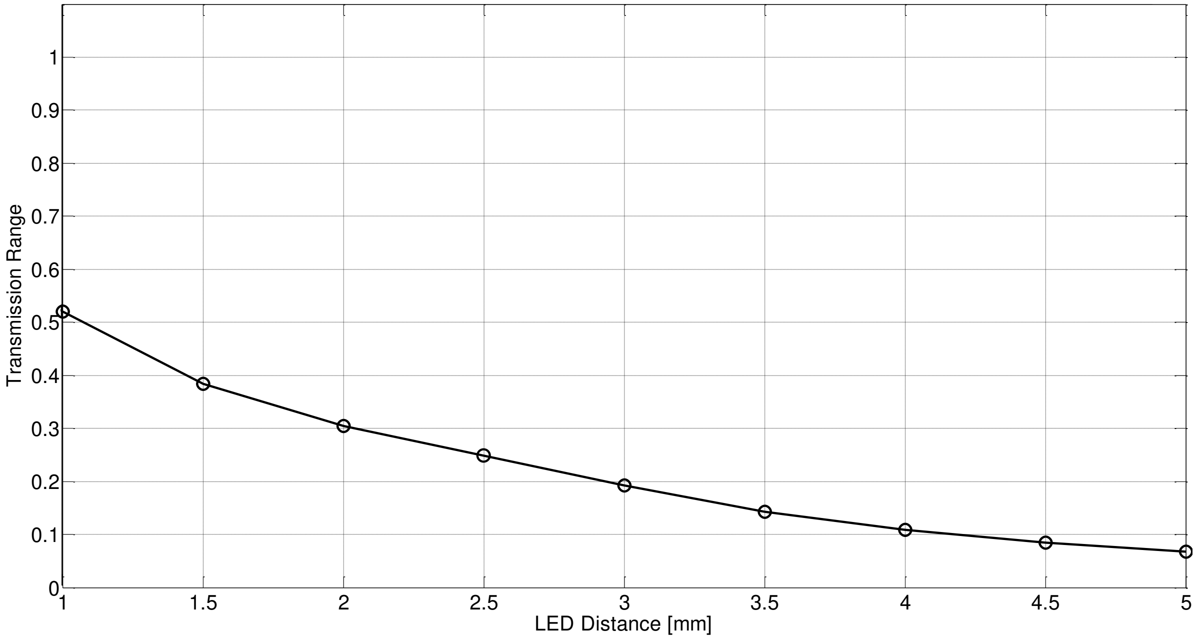

Figure 37: Predicted behavior of the transmission range measured in the fiber for various LED source distances.

Similar to the change in sensing length, increasing the LED launching distance does not affect the index of minimum transmission of the FOEWS. Predictions from the model for indices of minimum transmission as a function of launch distance are given in Figure 38. A constant index of minimum transmission index is expected from the illumination condition equations of Section 3.2.3. Since the LED is modeled as a Lambertian source with a small angular emission width, the variation in propagation angles of ray on the fiber face vary only slightly when the LED distance is held at distances above 1 mm. With such small variations in propagation angle, the resulting reflection coefficients and number of reflections along the sensing region are held constant.

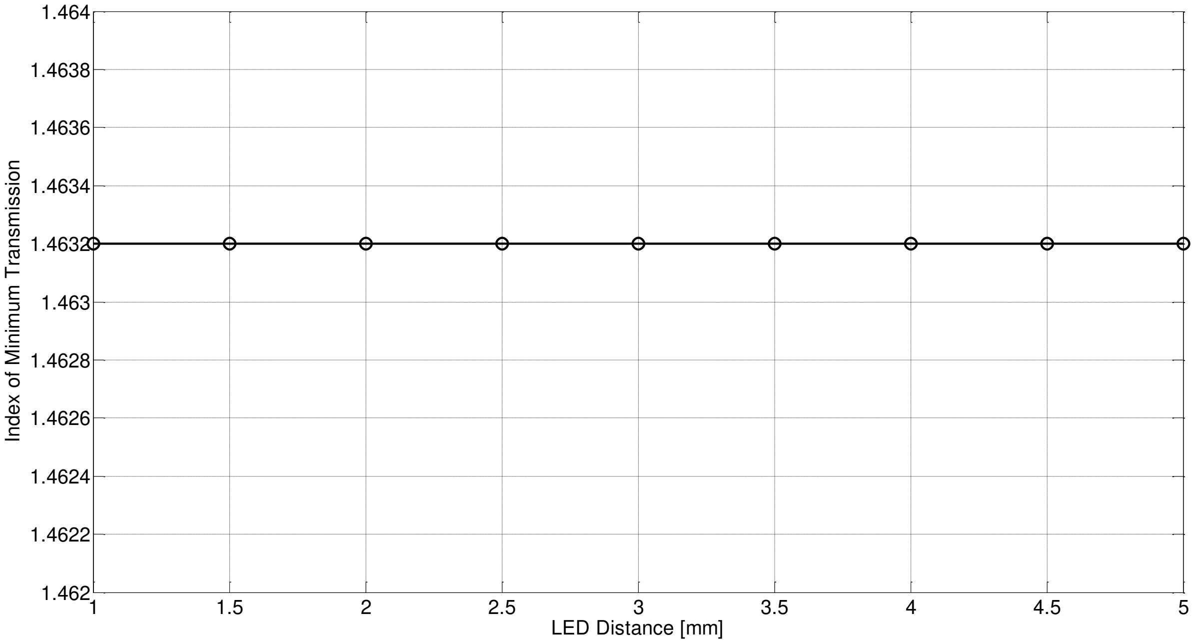

Figure 38: Predicted behavior of the change in the minimum transmission index for various LED source distances. Unlike the phenomena seen with variation in cladding thickness, the distance of LED illumination shows no change in the index of minimum transmission value.

3.3.4 Title angle of LED to fiber face

In addition to the LED distance to the fiber face, the tilt angle that the LED makes to the optical axis as described in Figure 24 can be varied to elicit a change in the transmission response of the FOEWS

Figure 39 presents the change in relative power transmission for changes in the tilt angle between the optical and fiber axes of 0 to 5°, on the sensing response to sample external media with IOR ranging from 1.42 to 1.6 for a sensor with a fixed cladding thickness of 0.5 μm and LED illumination distance fixed at 1 mm.

When the tilt angle is increased beyond 5° the fiber no longer allows for rays to enter at such high incident angles and light no longer enters the FOEWS. The range of acceptable incident light ray angles is determined by the NA of the fiber and is a function of the IOR of the core and cladding defined by Eq. (18). For the values of the core and cladding IOR assumed here the NA is approximately 0.22

corresponding to an acceptance angle of 12.5°. Note that the model shows little to no relative power transmission for external media IOR values above the core IOR for tilt angles of 4 and 5°.

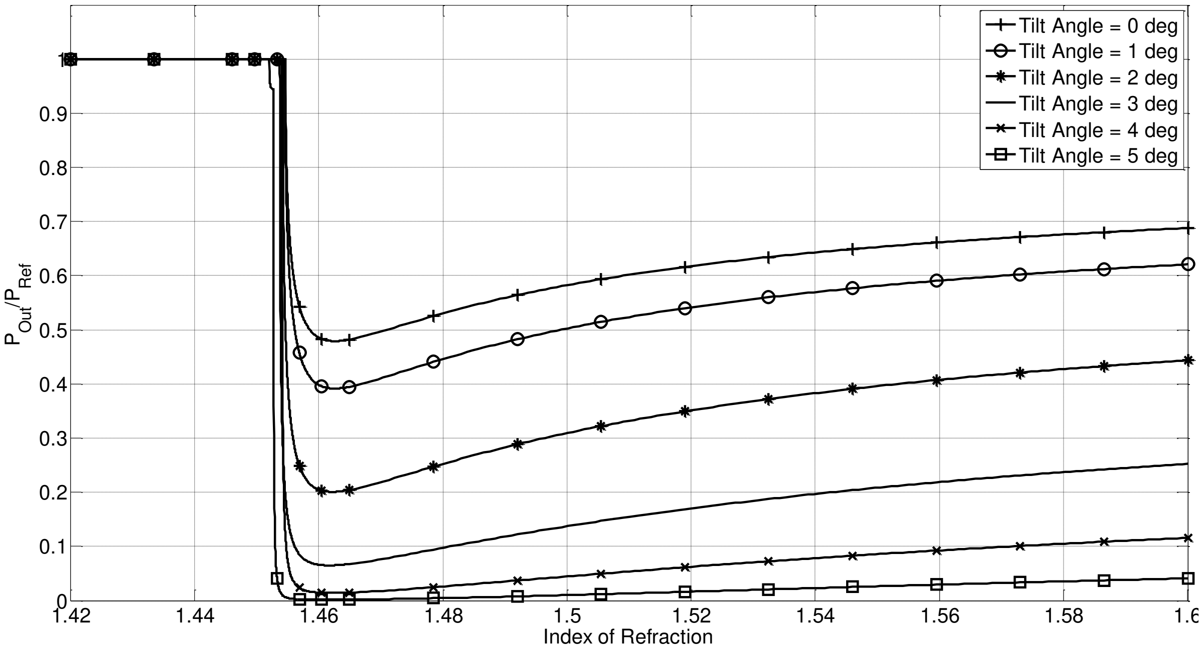

Figure 39: Predicted normalized power loss for sensors with tilt angle between the optical and fiber axes ranging from 0-5° in response to external media with IOR values from 1.42 to 1.6. Cladding thickness was held at 0.5 µm an LED illumination distance of 1 mm.

In Figure 40 the transmission range as a function of the tilt angle is summarized. As the tilt angle increases the drop in relative power transmission is increased. In a similar reasoning to the effects of LED distance on relative power transmission, as the tilt angle is increased, rays propagate inside the fiber with a larger propagation angle. Since rays propagating at larger propagation angles have smaller reflection coefficients and interact more with the core cladding interface, they lose more power to the external media.

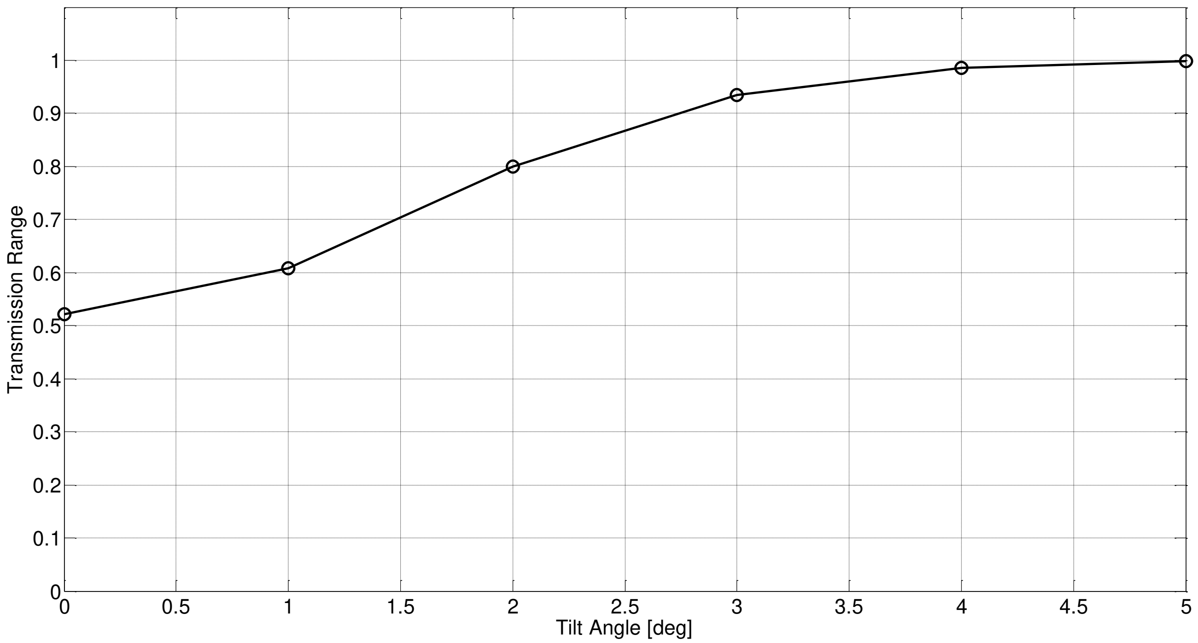

Figure 40: Predicted behavior of the transmission range measured in the fiber for various angles of tilt of the source LED.

Unlike the LED distance, tilt angle greatly affects the propagation angle of rays within the fiber, and as a result the angle of incidence for reflections at the sensing region. However, this change in incidence angle should have no effect on the index of minimum transmission. Figure 41 summarizes the change in minimum transmission index as a function of the tilt angle as predicted by the model and compared to the behavior of the same reflection coefficient off a thin film structure used in Section 3.3.1. The index of minimum reflection off a thin film structure does not change as a function of the incident angle. In comparison, the model predictions remain relatively constant but due show slight variation with tilt angle. These variations are a result of the numerical inaccuracy for the calculation of the relative power output of the FOEWS. As the tilt angle increases, the calculated absolute power output of the FOEWS becomes extremely small so that imprecisions in numerical calculations result in a slight variance in the index of minimum transmission. Compared to the variance in index observed with change in cladding thickness, the variance observed here are minor enough to be considered constant.

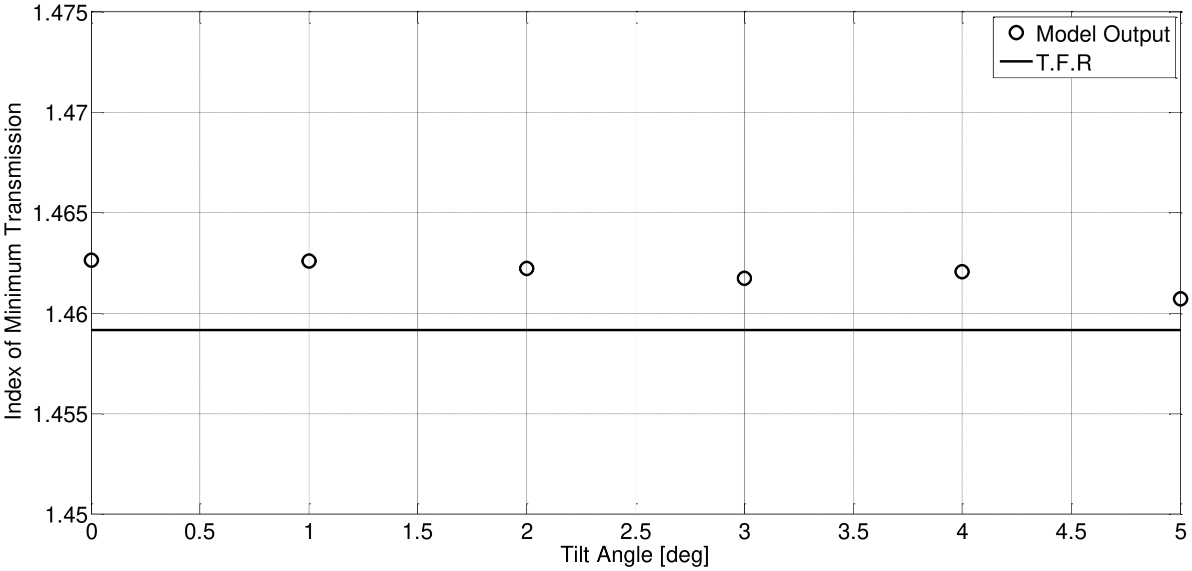

Figure 41: Predicted behavior of the change in the minimum transmission index for various angles of tilt of the source LED for the model compared to the same thin film reflection calculation of Figure 32. A slight change in the index of minimum transmission is seen with tilt angle as a result of numerical imprecision due to low output power at higher angles.

Chapter 4

Experimental Validation and Results

This chapter presents the experimental results conducted on a fabricated FOEWS to verify the proposed model. The response of the sensor was measured against exposure to several liquid samples. The thermo-optic properties of the liquids were utilized to obtain a response curve over a range of IOR values. For precise control of the temperature of the liquid an aluminum thermal test bed was setup and its details are presented here. The design of the test bed ensures proper submersion of the sensing region within the liquid analyte while keeping it away from the aluminum side walls. Real-time monitoring of temperature ramping of the liquid and optical response of the FOEWS is used to map the measured response to the calculated IOR of the sample. Once the IOR optical response relation for the tested FOEWS is produced, the observed response is compared to the theoretical response predicted by the FOEWS model presented in the previous chapter. Due to difficulties in direct measurement of the cladding thickness of etched FOEWS, fitting of the experimental results to the theoretical model is used to estimate the cladding thickness of the fiber. The quality of fit between the experimental results and the theoretical predictions is then used to validate the precision of the model.

4.1 Experimental Setup

In order to accurately characterize the response of a FOEWS, accurate control of the IOR of the analyte material is required. The method described below makes use of thermo-optic liquids which are calibrated to give precise IOR values over a specified range of temperatures. To fully take advantage of the precision of the calibrated liquids, a custom designed thermal test bed was developed for the purpose of accurately and reliably monitoring the temperature of the sample liquids while keeping ensuring full suspension of the FOEWS sensing region within the sample liquid. The schematic of Figure 42 outlines the proposed design for the thermal test bed. The main test bed is milled from a solid $1.3 \times 5 \times 10$ cm block of aluminum chosen for its high heat conduction and dimensioned large enough to provide a stable uniform temperature across the well. The fiber optic cable is guided and held in place within the well using modified syringe needles that have been retro-fitted with bare fiber terminators obtained from ThorLabs (Product name BFTU-Universal Bare Fiber Terminator) [75]. The syringe needles are bent at two points in order to position the sensing region of the fiber in the center of the test well and to avoid kinks in the fiber. The BFTUs act as clamps on the fiber locking the sensing region of the FOEWS within the well while maintaining a constant tension in the fiber which keeps the sensing region from touching the aluminum edges of the well. The optical fiber guides are secured to the aluminum test bed with Teflon strips which are bolted to the top surface of the test bed. The Teflon strips provide sufficient pressure on the optical fiber guide while distorting enough to avoid collapsing the syringe needle.

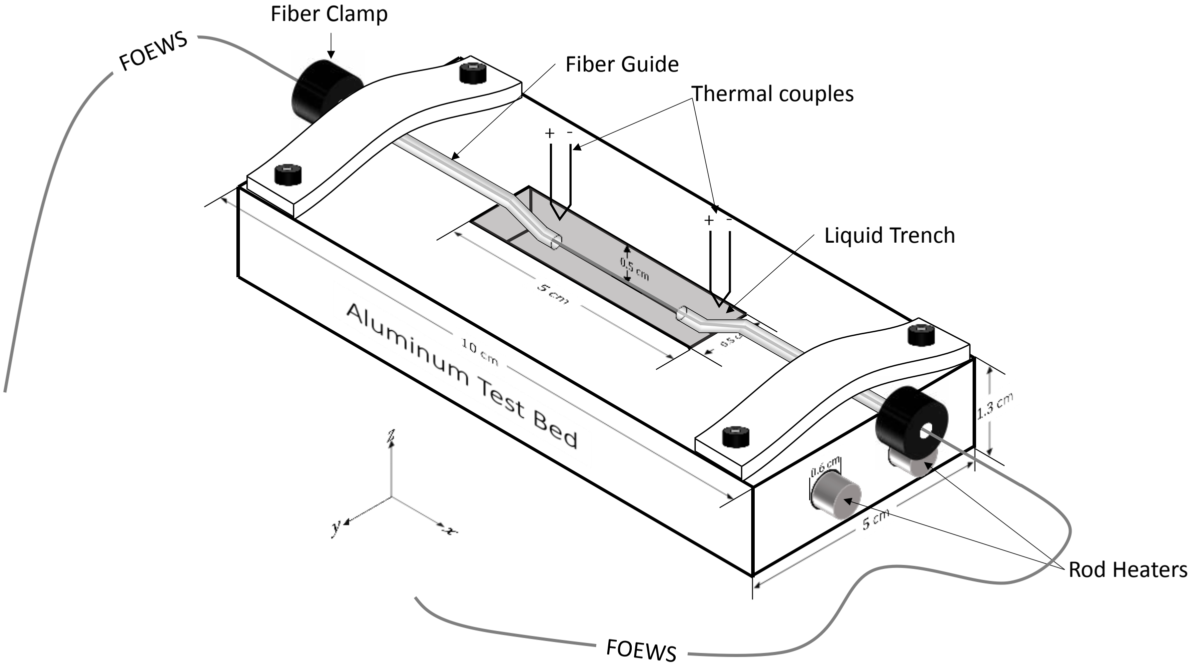

Figure 42: Schematic of the oil reservoir test bed used for the temperature sensitive oil test of the FOEWS.

Temperature control of the sample well is accomplished with the use of two rod heaters inserted longitudinally into the aluminum bed on either side of the well. Quarter inch FIREROD® heaters from Watlow were chosen as the heat sources [76]. The rod heaters were controlled using a Watlow mini control console model number K5R1-0000 [77]. The control console monitors the temperature of the test well using a K-type thermocouple which is placed at one end of the test well. Accuracy in the control console temperature reading is $\pm 0.1\%$ of span. To ensure a constant temperature in the test bed, a second sensing K-type thermocouple is placed at the opposite end of the test well. Experimental testing of the variation in the temperature between each end of the test well was found to be within $0.1°\mathrm{C}$ for well temperatures up to $100°\mathrm{C}$.

The sensing thermocouple is read monitored and recorded in real-time every second using an NI USB-TC01 thermocouple measurement device from national instruments product number 781314-01 [78]. The temperature was recorded with equal time resolution as the optical response of the sensor for accurate correlation.

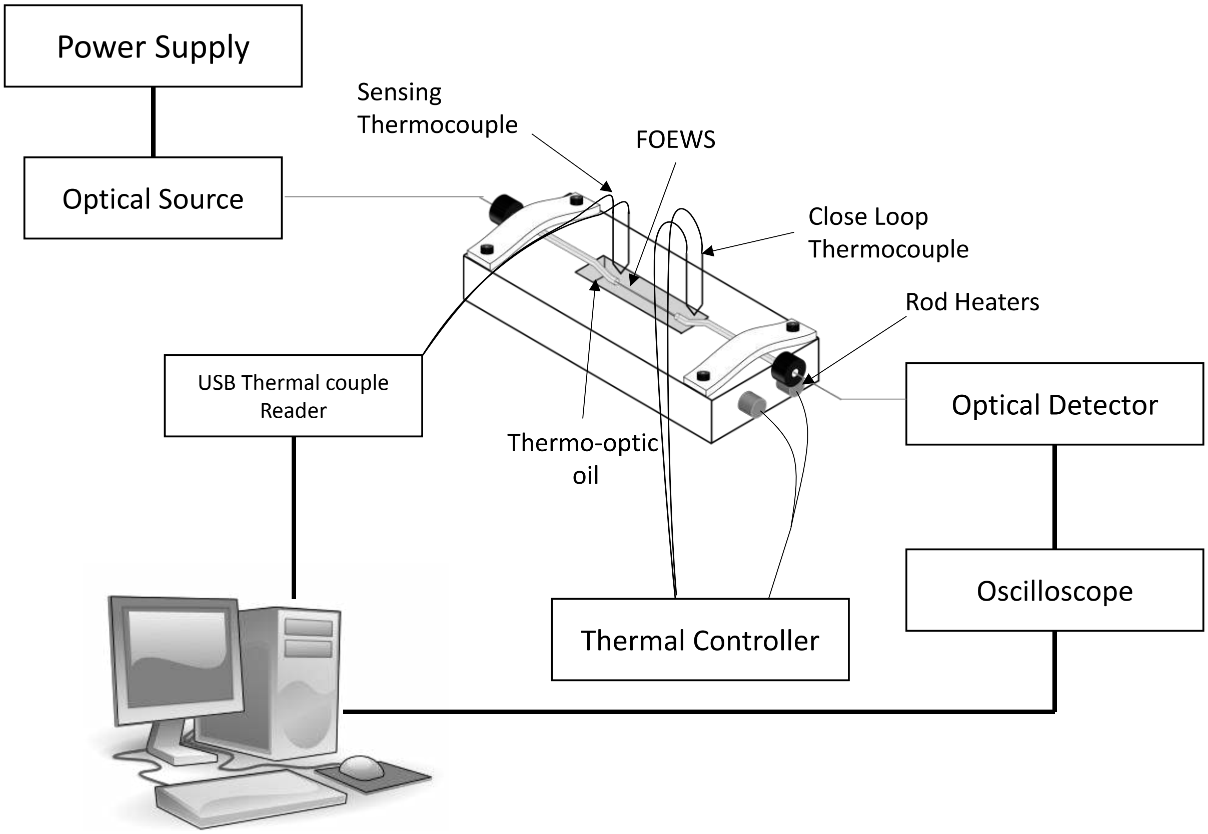

Figure 43: Overview outlining the components used in the characterization of the FOEWS and the experimental setup used in testing the FOEWS.

The FOEWS is illuminated using a high speed infrared surface emitting diode with an 850 nm emission narrow band spectrum available from Vishay Semiconductors model number 782-VSLY5850 [79]. As described in the previous chapter the LED has a beam angle of 3° with a radiant intensity of 600 mW/sr. Light from the LED is coupled directly into the fiber using an LED mounting adapter from ThorLabs product number RMS11P [80]. The LED source is powered using an Agilent E3631A DC power supply [81]. The intensity of the LED was fixed by holding the power supply output at a constant voltage of 1.67 Volts and 90 mA, corresponding to approximately 30 mW of radiant power. The output intensity of the FOEWS was measured using a ThorLabs DET10C- InGaAs detector which converted the optical signal to a current which was read by an Agilent 54621D oscilloscope [82], [83]. The oscilloscope was connected via GPIB to a desktop computer which recorded the optical signal and temperature readings in real-time. Figure 43 illustrates experimental setup schematic of the equipment used in the characterization of the FOEWS.

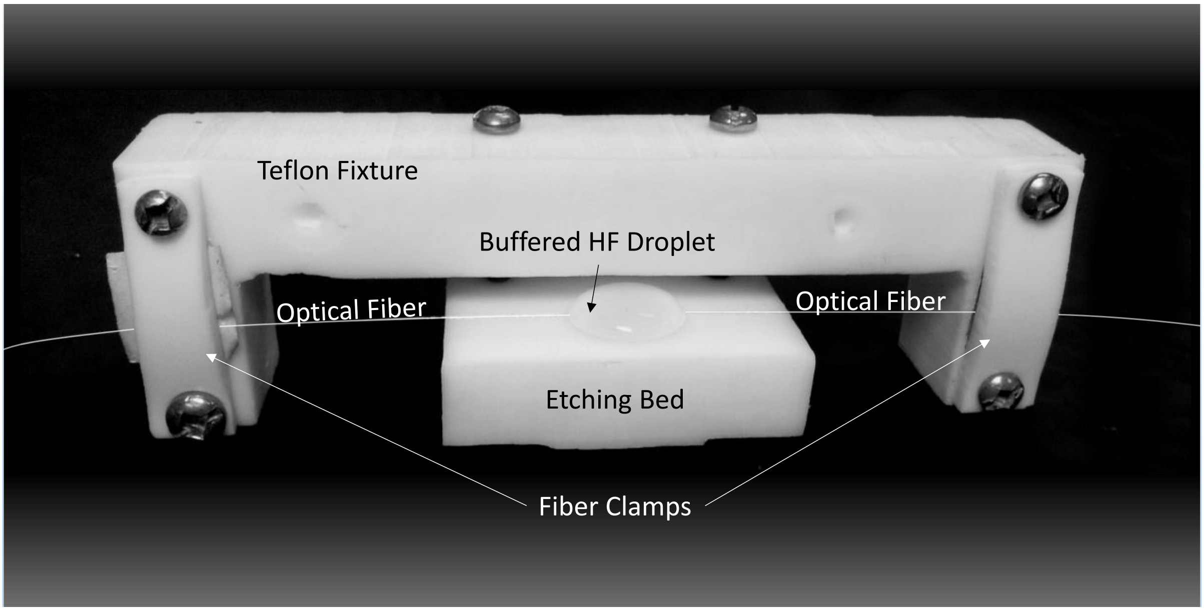

Figure 44: Teflon fixture used to etch optical fiber sensing region with BHFA.

The FOEWS itself was fabricated from a low-OH, set index multimode fiber from ThorLabs product number AFS105/125Y [84]. The optical fiber has a 105 μm silica core and a fluorine doped silica cladding that is 125 μm in diameter. The refractive index of the solid silica core is reported as 1.452 at a wavelength of 850 nm according to the work of Malitson [85]. The optical fiber is surrounded by an acrylate coating material. Fabrication of the sensor requires removal of the coating material and reduction of the cladding thickness over a given sensing length of the fiber. The acrylate coating is chemically removed with acetone exposing the fluorine doped cladding. Removal of the cladding requires chemical etching using hydrofluoric acid. The fibers are etching using a custom designed Teflon fiber holder for controlled emersion of the fiber within a buffered HF solution as shown in Figure 44. Etching depth of the cladding is controlled by emersion time in the acid and a rough estimate of the cladding thickness is accomplished using a combination of optical microscopy measurement and a glycerol contrast test. The etching process is carried out using a BHFA consisting of 6 parts NH_4F (40 % concentration) and 1 Part HF (49 % concentration which results in an etch rate of approximately 1 µm/min.

Under observation in a SEM as shown in Figure 45 the final etched surface is smooth with no pitting visible. The jacket, un-etched and etched regions of the fiber are visible within the image. Clear boundaries between the regions are visible, between the etched and etched region of the fiber a tapered region is visible which is caused by the partial emersion of the fiber in the buffered HF during etching. Measurements of the width of the fiber at the etched region vary along the entire etched region between anywhere from 102.1 to 104.6 µm with a mean value estimated at 103 µm.

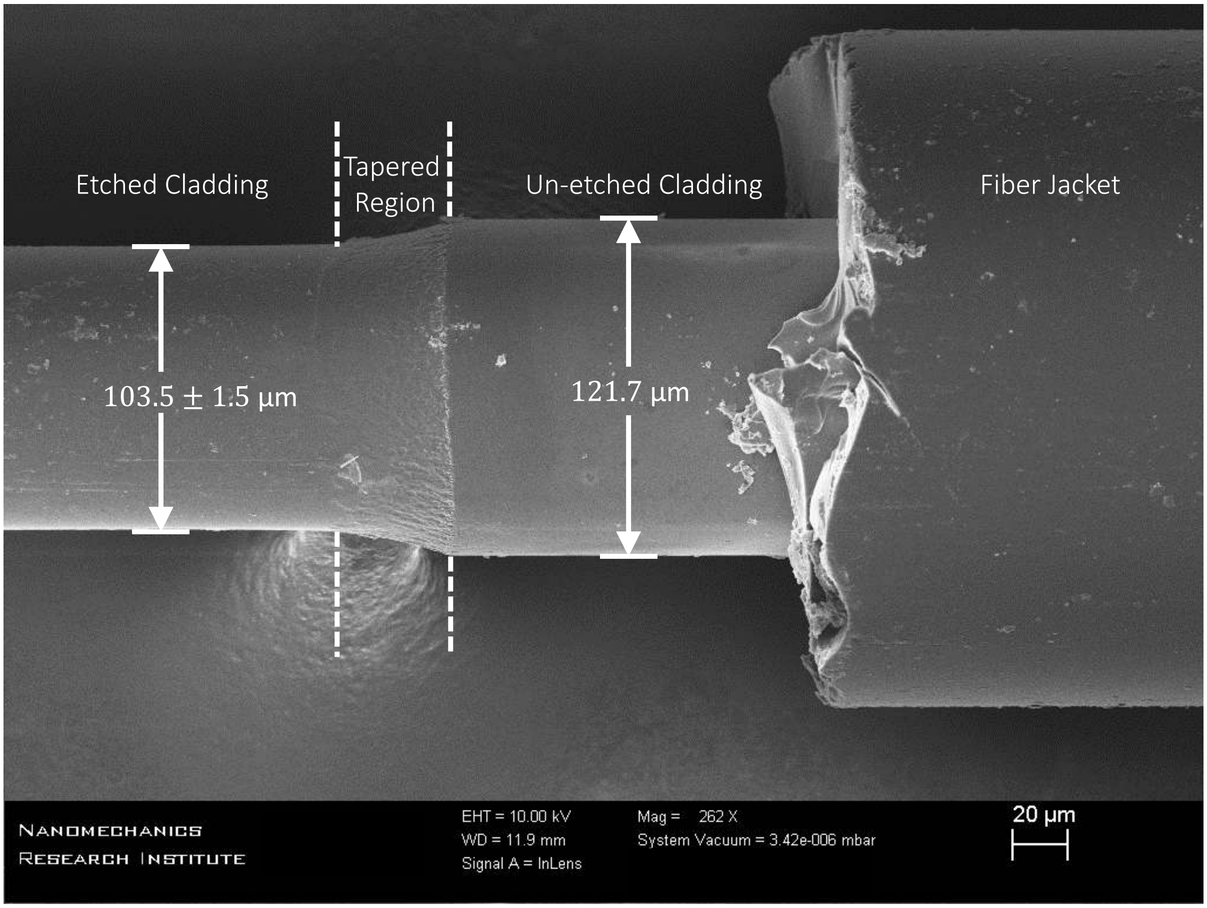

Figure 45: Scanning electron image of an etched FOEWS using a buffered HF solution sputtered with gold at a thickness of 10 nm. Image shows widths of fiber at both the etched and un-etched regions as well as the fiber jacket region.

4.2 Experimental determination of temperature dependence

To ensure that no intrinsic error in measurement can be attributed to the temperature of the FOEWS during measurement, it is important to isolate the sensor response to change in temperature. The goal of this section is to characterize the change in response of the FOEWS purely from a change in temperature while maintaining a constant IOR of the sample liquid. Since most liquids exhibit a change in IOR under a change in temperature, pure water is used to test the temperature dependence of the FOEWS. In Chapter 3 it was noted that when the FOEWS was exposed to an analyte with an IOR value below that of the IOR of the core, no power from the core escapes from the sensing region. Thus, the response for any IOR of the analyte below the core IOR should remain constant. Therefore, by exposing the FOEWS water which is known to have an IOR below the core index for all temperatures will allow the characterization of the intrinsic temperature dependence of the FOEWS itself.

Deionized water presents itself as an optimum candidate for use in measuring the temperature dependence of the FOEWS. The measured IOR of water at 850 nm was reported as 1.3276 by Daimon and Masumura [86]. This is well below the value of 1.455 for the core of the fiber. Additionally, the change in IOR of water was investigated by Bashkatov and Genina and the IOR change at 850 nm was reported to decrease by 0.014 with a temperature change from 0 to 100 °C [87]. Therefore, that for temperatures between 0 to 100 °C with an interrogation wavelength of 850 nm, any change in optical response of the FOEWS is attributed to the intrinsic temperature dependence of the sensor.

It should be noted that testing the FOEWS temperature response with an empty test well would also satisfies the low IOR requirements of test. However, attempting to accurately determine the temperature of the FOEWS in an air environment becomes more difficult than in water. Emersion of the FOEWS in water allows for conductive heating of the fiber in contrast to convective heating in air. In addition, emersion in water helps maintain a uniform temperature reading over the sensing length of the fiber due to the thermal capacity of water.

Figure 46 presents both the recorded temperature and normalized optical response of a fabricated FOEWS immersed in deionized water and exposed to a temperature ramping and cooling over time. The measured temperature of the FOEWS was ramped from 25 to 70 °C over a period of 90 seconds and then allowed to cool to 47 °C over a 14 minute period. The optical response of the sensor is presented as a ratio of the recorded voltage from the oscilloscope to the measured reference voltage.

The reference voltage is taken at a temperature of 25 °C. The reference voltage ratio corresponds to the in air power ratio used to characterize FOEWS performance back in Section 3.3.

Upon inspection of the normalized optical signal during the temperature ramping of the FOEWS in Figure 46, a change in optical signal of 0.4 % was measured over the full 50 degree temperature ramping. However, the simulations presented in Section 3.3 expect no change in optical signal for the corresponding IOR change of water at these temperatures. The observed change in response of the FOEWS due to temperature change is hypothesized to be caused by the change in IOR of the core and cladding materials of the fiber optic cable itself.

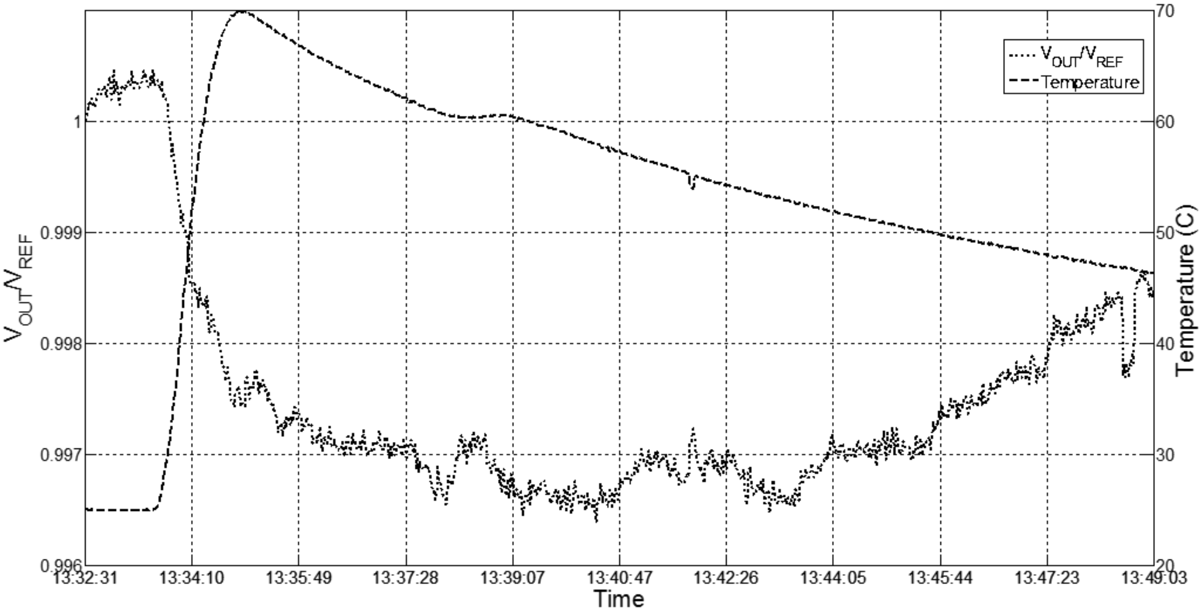

Figure 46: Recorded temperature dependence of FOEWS with temperature variations from 20°C to 70°C. Normalized change in optical response is minimal.

Changes to the IOR of the core and cladding materials would result in a change to the NA of the fiber resulting in a change in the transmission properties of the FOEWS. According to the specifications of the SFS105/125Y optical fiber used in this experiment, the designed operation temperature ranges from −40 to 85 °C [71]. Therefore, a 0.4 % change is relative transmission is to be expected for exposure to temperature variations of 50 °C.

With the intrinsic temperature variation of the FOEWS determined to be within 0.4 % of the reference transmission, it can be concluded that neglecting the effects of transmission variations in the

FOEWS model due to temperature changes will not significantly diminish the accuracy of the model. In the experimental test, and model verifications that follow, no accounting for temperature changes in the response properties of the FOEWS will be considered.

4.3 Experimental validation using calibrated oil samples

Now that the intrinsic temperature dependence of the FOEWS has been determined, thermo-optical oil is used next to characterize the transmission response of a FOEWS to known IOR changes in the analyte solution. The thermo-optic oil used in this section is the series A product number 14720 certified oil available from Cargille labs. The oil has a reported IOR of 1.4649 at 850 nm and a temperature coefficient of −3.92e-4 per degree Celsius.

The transmission voltage from the oscilloscope was measured before the addition of the oil to the test bed well and used as the reference voltage which would be used to normalize the transmission response to the thermo-optic oil. Figure 47 summarizes the recorded transmission response of the FOEWS during several temperature cooling runs using the test bed of Figure 42. It was noticed during testing that the rapid heating cycle of the test bed the correlation between the recorded temperature and transmission response is less accurate then during the longer cooling cycle. Therefore, the data shown in Figure 47 includes only the recorded data during the cooling period of the test bed.

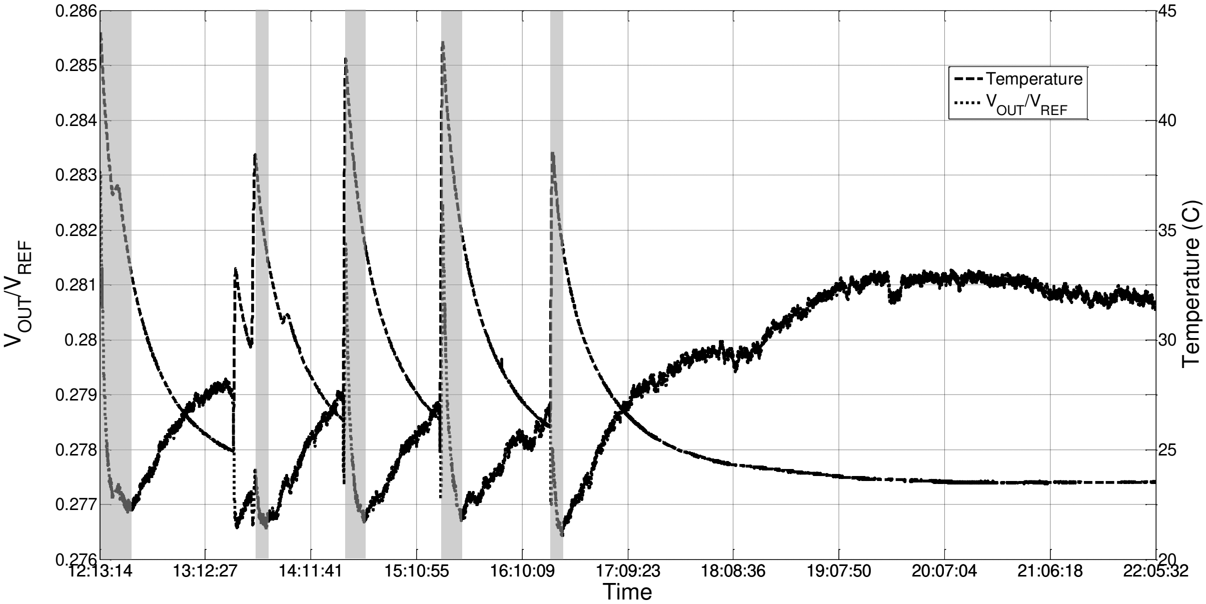

Figure 47: Recorded sensor response to thermo-optic oil at temperatures ranging from 22 to 44 °C. Optical response of sensor is given as a ratio to the reference signal in air.

From the temperature transmission response summarized in Figure 47, the transmission response correlates directly to the temperature of the oil for temperatures below **35** ℃, and correlates inversely with temperatures above as highlighted by the gray regions on the graph. The change in correlation behavior suggests that the thermo-optic oil IOR is spanning the region of minimum transmission of the FOEWS as described in the predicted response analysis of Section 3.3.

The measured temperature data of Figure 47 is converted to the IOR value of the thermo-optic oil using the relation given by:

$$N_{oil} = (T - 25)(-3.92e - 4) + 1.4650. \tag{56}$$

Where T is the recorded temperature of the test oil within the test bed. The temperature of the test bed was held below **35** ℃ in order to stay within the accuracy of the thermo-optic coefficient provided by the manufacturer. Using the relation given by Eq.(56), the transmission response as a function of IOR of the thermo-optic oil is derived and plotted in Figure 48.

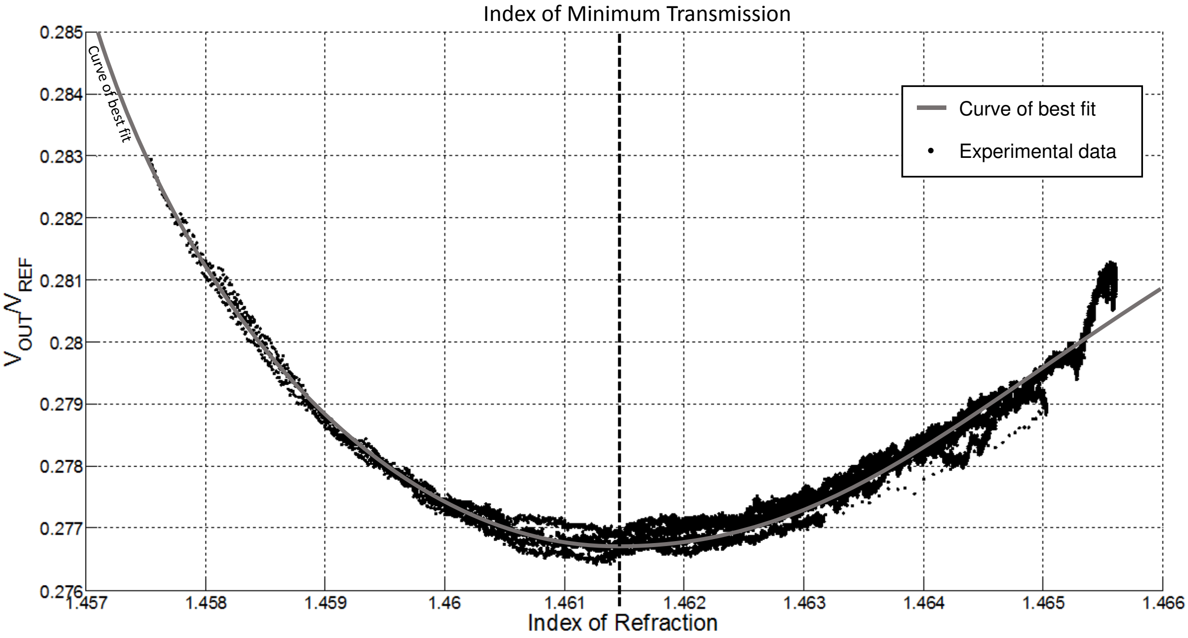

Figure 48: Computed normalized optical response to IOR of Series A 14720 thermo-optic oil created from the results of Figure 47 and the relation of Eq.(56). The index of minimum transmission is found from the curve of best fit and is estimated at 1.4615.

A curve of best fit is drawn over the scatter point data, and is used to determine the index of minimum transmission. From the graph in Figure 48, the index of minimum transmission is found to be 1.4615. In Section 3.3.1, it was determined the relationship between cladding thickness and the index of minimum transmission. Using the relationship correlating the index of minimum transmission to cladding thickness similar to Figure 32 for a fiber with a core index of 1.452, the correlation of index of minimum transmission to cladding thickness for a SFS105/125Y optical fiber shown in Figure 49 was obtained. The predicted cladding thickness of the sensor is found to be 0.57 m. This prediction falls well within the observed cladding thicknesses under SEM.

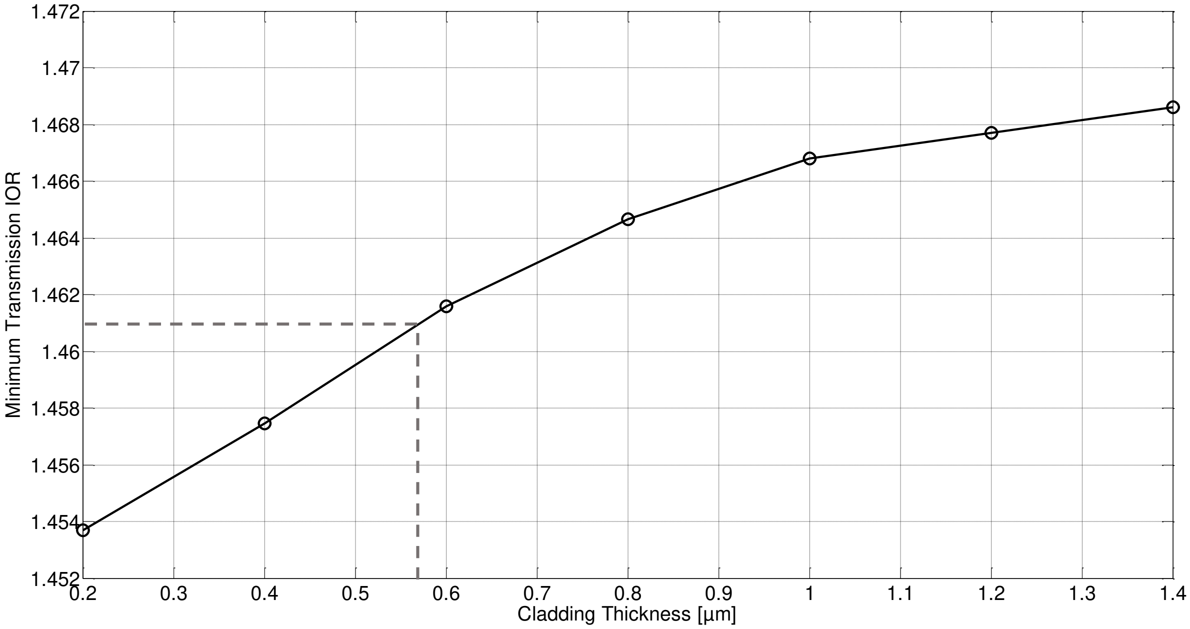

Figure 49: Index of minimum transmission as a function of cladding thickness as predicted by the model using the material properties of the SFS105/125Y optical fiber. Predictions show that the cladding thickness corresponding to the minimum transmission index of 1.4615 is about 0.57 µm in thickness.

4.4 Experimental validation using Glycerol

In addition to tests using the thermo-optic oil, a second analysis of the transmission response using the temperature dependent IOR of glycerol was performed. The full summarized temperature ramping of glycerol and transmission response of the FOEWS are shown in Figure 50. At the start of the experiment the transmission intensity before the addition of glycerol was recorded as indicated by $V_{REF} =$. The sharp drop in transmission intensity corresponds to the addition of glycerol to the test well. The IOR range of glycerol partially overlaps that of the thermo-optic oil used in the previous section. As such, the optical response of the FOEWS shows both positive in white, and negative in gray, correlations with the temperature range indicating that the index of minimum transmission of the FOEWS is reached during the temperature ramping of the glycerol. As in the case with the thermo-optic oil tests above. The data retrieved from the experiment for analysis excludes the temperature ramping portions of the test in favor of the slower cooling ramps. A total of three cooling cycles where performed, with only one encompassing the region of index of minimum refraction.

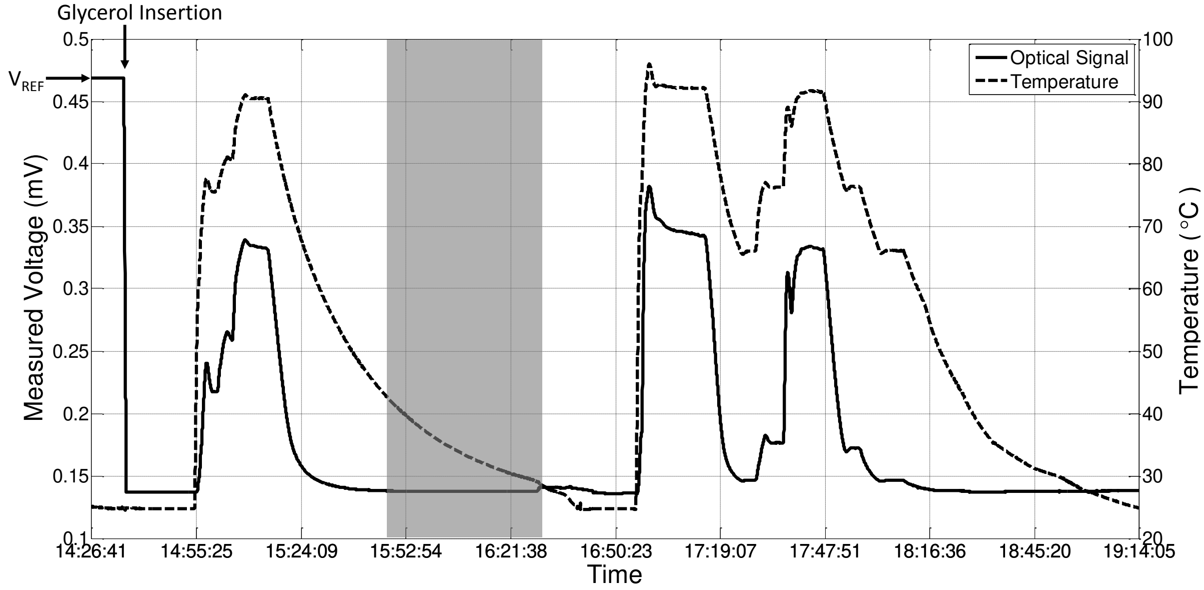

Figure 50: Recorded sensor response to glycerol at temperatures ranging from 25 to 95 °C. Optical response of sensor is measured as the voltage outputted from the photo detector. V_{REF} is the reference voltage measured in air before the insertion of glycerol. The gray region indicates where the correlation between the optical signal and the temperature is negative.

The thermo-optic properties for glycerol were derived from work done using an Abbe refractometer by Rheims et al. in [88]. The Cauchy dispersion constants were determined for wavelengths in the near infrared (IR) range. Additionally, measurements of the IOR change from at temperatures of 20 and 25°C were also conducted. The IOR of glycerol at 850 nm at 25 °C is given by the Cauchy dispersion equation as:

$$N_{glycerol}\Big|_{\lambda=8500\text{Å},T=25^{\circ}\text{C}} = 1.4585519 + \frac{446809}{\lambda^2} + \frac{7.018541e11}{\lambda^4} = 1.4642. \tag{57}$$

The reported index of glycerol at 20°C was given as 1.4670. Assuming a constant temperature coefficient for the thermo-optic properties of glycerol, a determined thermo-optic coefficient of $-2.2e-4\ {}^{\circ}\text{C}^{-1}$ was found. Using this coefficient the correlation between the calculated IOR of glycerol and the FOEWS sensor response was produced and is shown in Figure 51. It can be seen from the summarized data that the upward swing of the transmission response at lower IOR values is less sharp than expected from the response predictions calculated in Section 3.3. It is reasoned that the apparent deviation from expected behavior at lower IOR values are due to nonlinear behavior of the thermo-optic coefficient at the corresponding temperatures.

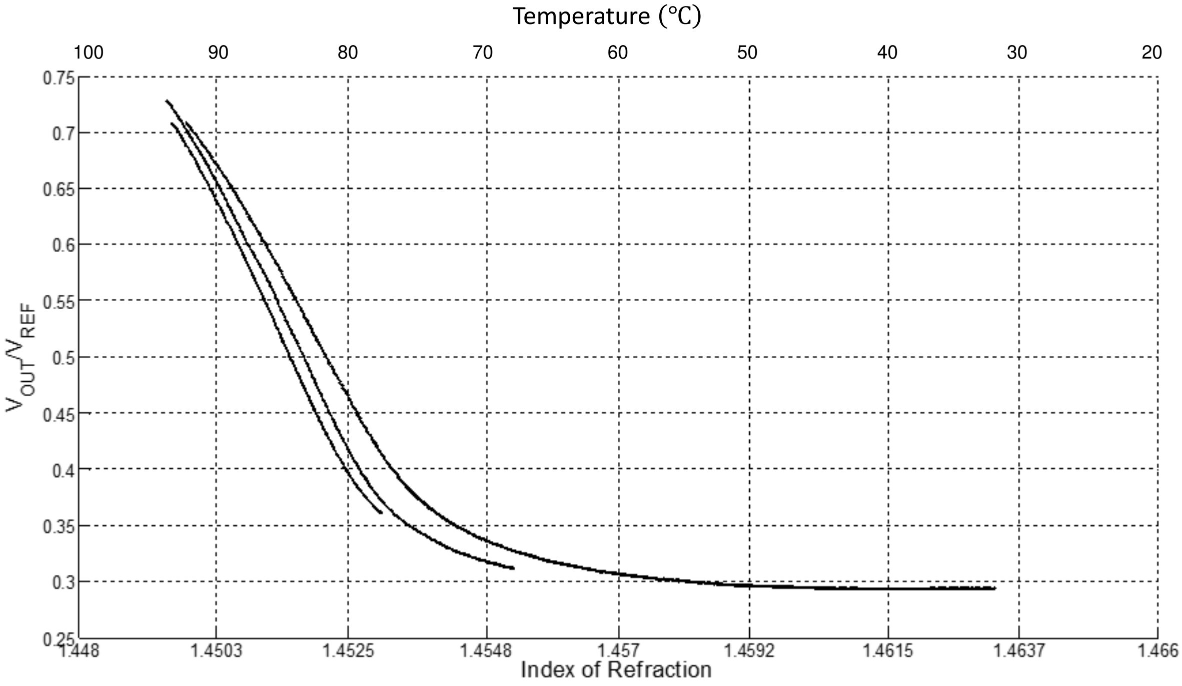

Figure 51: Recorded normalized optical response to IOR change using glycerol measured with 1 Hz sampling. At Temperatures above $70\ {}^{\circ}\text{C}$ the uncertainty in the thermo-optic coefficient of glycerol results in uncertainty in the proper calculation of the IOR. The presence of multiple sets of data points is attributed to measurement drift in the system.

As mentioned above, only one of the cooling cycles was able to pick up the point of minimum transmission. Enlarging the region of minimum transmission and finding a curve of best fit allows us to determine a precise minimum IOR. Figure 52 shows the enlarged region of minimum transmission along with the curve of best fit to the cooling cycle data. However, the IOR of minimum transmission is found to be located at $1.4617 \pm 2\text{e-}4$, corresponding to a cladding thickness of 0.57 to 0.62 μm from Figure 49 matching well with the reported minimum from the thermo-optic oil tests.

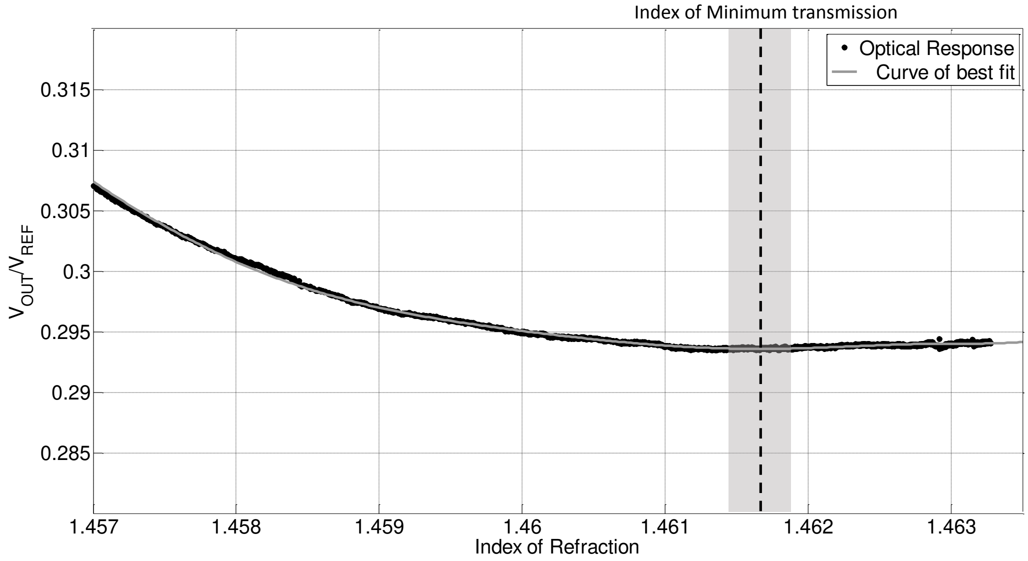

Figure 52: Enlargement of the region where the FOEWS transmission response is minimum. The gray highlighted region gives the uncertainty in the position of the minimum transmission of 29.4%.

In contrast to how the position of the index of minimum transmissions agreed well between both the thermo-optic oil and glycerol tests, the normalized voltage values for corresponding regions deviated much more significantly. The relative output ratio of the thermo-optic oil at the index of minimum transmission was reported in Figure 48 as $27.7 \pm 0.05\%$. While as shown in Figure 52, the reported output ratio was recorded as 29.4%. Measurements of recorded output ratios are subject to various external factors which can change the reference voltage of the FOEWS making it more difficult to accurately determine normalized transmission response intensity. Tracking the index of minimum transmission of a FOEWS removes the uncertainty related to direct intensity measurements providing a more accurate method for the determination of cladding thickness.

4.5 Comparison to Model Predictions

Combining the experimental sensor response to both the glycerol and thermo-optic oil tests provides a measure of the FOEWS response to IOR changes of the analyte liquid from 1.451 to 1.466. The experimental results presented in the previous two sections are combined to obtain the measured response shown in Figure 53. In addition, identifying the index of minimum transmission using the thermo-optic oil and glycerol experiments predicted a cladding thickness for the FOEWS of 0. 57 μm. In this section a comparison of the full FOEWS response curve measured experimentally in the previous sections to the corresponding model predictions using this cladding thickness obtained experimentally is done. This comparison will demonstrate the ability of the model to accurately predict the transmission response of a FOEWS over a range of analyte IOR values.

Figure 53 shows the fitting of the model to the experimentally measured transmission response. Using the predicted cladding thicknesses of Sections 4.3 and 4.4 that were arrived at by matching the observed index of minimum transmission a good fit of the model to the experimental results over the full range of IORs of the analyte from 1.451 to 1.466 is observed.

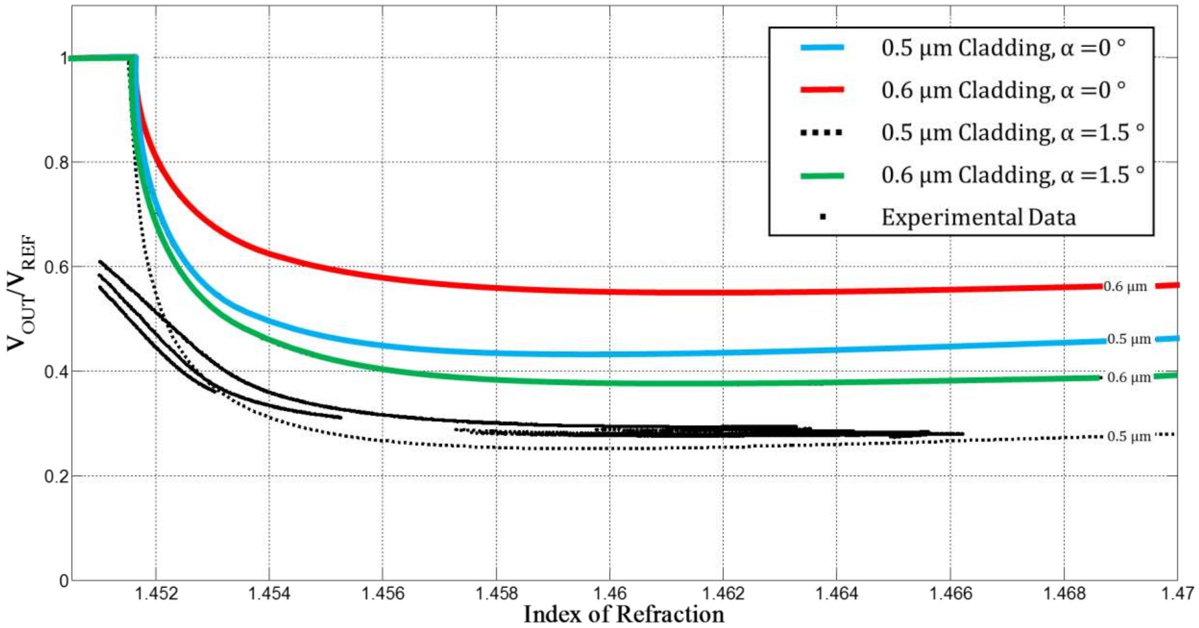

Figure 53: Fitting of the model to the experimentally measured transmission response behavior of a fabricated FOEWS. Experimental results fall within model predictions with a variation of 0.1 μm in the cladding thickness.

The predicted behavior from the model for a tilt angle $\alpha = 0°$ resulted in normalized transmission intensities higher than what was shown experimentally. However, the position of minimum transmission of the experimental and simulated response curves are in agreement. Running the simulations with a change in tilt angle of the LED on the fiber face of 1.5° shifted the response curves to the appropriate transmission response while keeping the index of minimum transmission at the same value. As discussed in Section 4.4, the transmission response of the glycerol test at IOR values below 1.454 correspond to a high temperature of the glycerol sample. Due to the limited information available on the thermo-optic properties of glycerol at these temperatures, deviation of the experimental curve from the simulated response is attributed to an error in the calculated IOR value of glycerol.

From this comparison, the measured transmission response of the fabricated FOEWS falls within a variation of $0.1\ \mu\text{m}$ in the cladding thickness and a correction in tilt angle (α) of 1.5° of the simulated response predictions. The measured cladding thickness from SEM analysis of the FOEWS had a median cladding thickness of 0.8 μm over an observed range from 0 to 1.4 μm. The value of 0.5 to 0.6 μm found from comparison with the model fall well within the acceptable range.

Chapter 5

Nature of Contact

The contact between the fiber optic sensing region and the analyte is crucial in the response of the sensor. If the analyte does not make full contact with the FOEWS, then the resulting signal modulation will differ from the expected response of a full contact model. As discussed in the literature of Chapter 2, the modelling of contact with analyte has larger been considered with gases and liquids where the sensing region is considered in full contact with the analyte material. In this section the transfer matrix method of analysis developed in Section 3.2.2.2 is used to account for a solid analyte held in partial contact with the FOEWS.

Partial contact of a solid analyte with the sensor implies that unlike a liquid or gaseous analyte, complete direct coverage of the sensing region is not guaranteed. Instead, there is the possibility for the presence of a separation layer forming in between the cladding and analyte layers that will affect the reflection coefficient calculation. Using the modelling of multi-layers structures that TMM provides it is simple to include an additional gap layer in of reflection coefficient calculation.

With partial contact of a solid analyte two possible interfaces are possible within the sensing region of the fiber, direct contact and no contact. Where the solid is in direct contact with the cladding the reflection coefficient can be determined using a three layer two interphase geometry that was used in Chapter 3. When the solid has no contact with the cladding of the sensing region a separate reflection coefficient can be calculated using a four layer three interphase geometry. The final response of the FOEWS with the partial contact solid analyte can therefore be determined by calculating the transmission loss from interaction using two sensing sections, (i) one representing full contact and a three medium interphase, and (ii) the second representing the gap and a four media interphase. The length of each respective section is determined by the percent of direct contact that the solid is determined to have with the FOEWS.

Once the model was extended to account for the partial contact of a solid analyte, analysis of SEM images of the contact surface of a solid graphite material that was held in partial contact with a fabricated FOEWS were conducted. The SEM images were used to determine percentage contact between the fiber and graphite surfaces, and to find appropriate values for the depth of the indirect contact gaps for modeling. An investigation of the resulting effects of several direct to indirect contact ratios, gap thicknesses, and optical properties of the gap media on the FOEWS response was also conducted.

5.1 Description of surface contact

A solid analyte in contact with a FOEWS differs from contact with a liquid or gas. Because a solid analyte will not conform completely to the surface of the fiber when in contact, there exists the possibility that gaps will appear between the analyte and cladding of the sensing region. In the literature review of Chapter 2 it was noted that the ability to account for a solid analyte in FOEWS models has received little to no attention. However, the derivation of the reflection coefficient for a sensing region using the TMM back in Section 3.2.2.2, has the advantage of accounting for not only a two interface but an n-interface system in general.

Recall that the TMM is capable of modeling thin films that can be considered of infinite dimension along the plane of incidence. Therefore, when applying it to the instance of partial contact with a solid analyte it is limited to cases where the gap between layers is optically large in the direction parallel to the plane of incidence, but can be thin perpendicular to it. Figure 54 provides a schematic representation of the type of partial contact described here using the TMM. Based on the limitations of the TMM to infinite planar geometries, the gap regions that can be considered must be optically larger in width $\left(w_{gap} \gg \lambda\right)$, and separated an optically large distances as well.

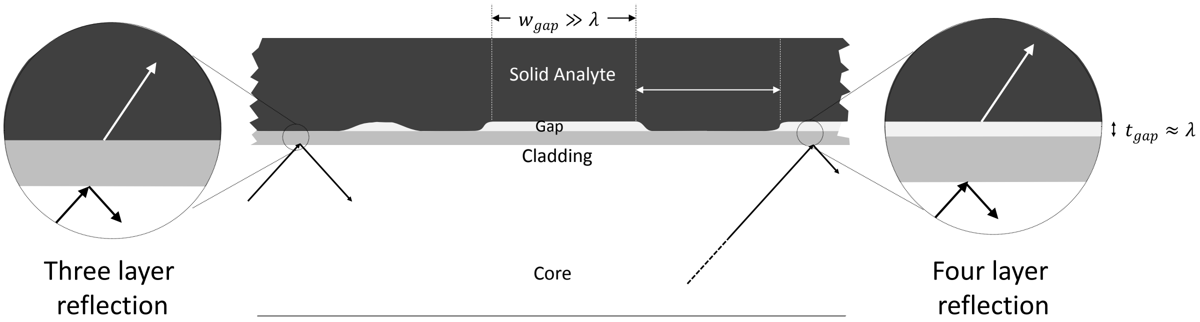

Figure 54: Schematic representation of the partial contact phenomenon included into the model. Gap regions are considered optically large in width and separated by optically large distances.

As a result on the limitations in gap geometry that result from the TMM, the gaps in the contact interface between the cladding and solid analyte must be large and spread relatively far apart. Relatively far apart refers to an optically large distance apart which is defined again by distances larger than an order of magnitude of the wavelength of interest, $(w_{contact} > 10\lambda)$. The limitation of optically large gaps and distances between gaps, is in fact useful for modeling a solid analyte that is inhomogeneous and composed of a conglomerate of large unit cells. In the following section, a graphite electrode, which under SEM is an ideal candidate for modeling the TMM partial contact method described here is characterized.

5.2 Derivation of three interface reflection coefficient

In Section 3.2.2.2 the reflection coefficient for a two interface thin film system using the TMM was derived. It was noted that this method can be easily used to solve a n-layer thin film interface by making use of characteristic matrix that will represent each layer in the stack. The general form of a characteristic matrix is [73]:

$$M_r = \begin{bmatrix} \cos\delta_r & \dfrac{i\sin(\delta_r)}{\eta_r} \\ i\eta_r\sin\delta_r & \cos\delta_r \end{bmatrix}. \tag{58}$$

Where,

$$\delta_r = \frac{2\pi N_r d_r \cos\theta_r}{\lambda},$$

$$\eta_r = \begin{matrix} N_r\sqrt{\epsilon_0\mu_0}\cos\theta_r, \text{for TE} \\ \frac{N_r\sqrt{\epsilon_0\mu_0}}{\cos\theta_r}, \text{for TM} \end{matrix} ,$$

with N_r representing the complex IOR of the individual layer and d_r as the thickness of the layer. The specific θ_r for each layer is calculated simply from the initial incident angle θ_1 using Snell's law. Once the characteristic matrix is defined for each layered media in the stack, the reflection coefficient of the structure is then found from the same equation as in Section 3.2.2.2 repeated here for clarity.

$$R = \left(\frac{n_{core}B - C}{n_{core}B + C}\right)\left(\frac{n_{core}B - C}{n_{core}B + C}\right)^{*}. \tag{59}$$

However, the individual coefficients B and C are now defined by the product of the individual matrices taken in the order presented in Figure 55, within the relationship below:

$$\begin{bmatrix} B \\ C \end{bmatrix} = \left\{ \prod_{r=1}^{q} \begin{bmatrix} \cos\delta_r & \dfrac{i\sin(\delta_r)}{\eta_r} \\ i\eta_r \sin\delta_r & \cos\delta_r \end{bmatrix} \right\} \begin{bmatrix} 1 \\ \eta_q \end{bmatrix}. \tag{60}$$

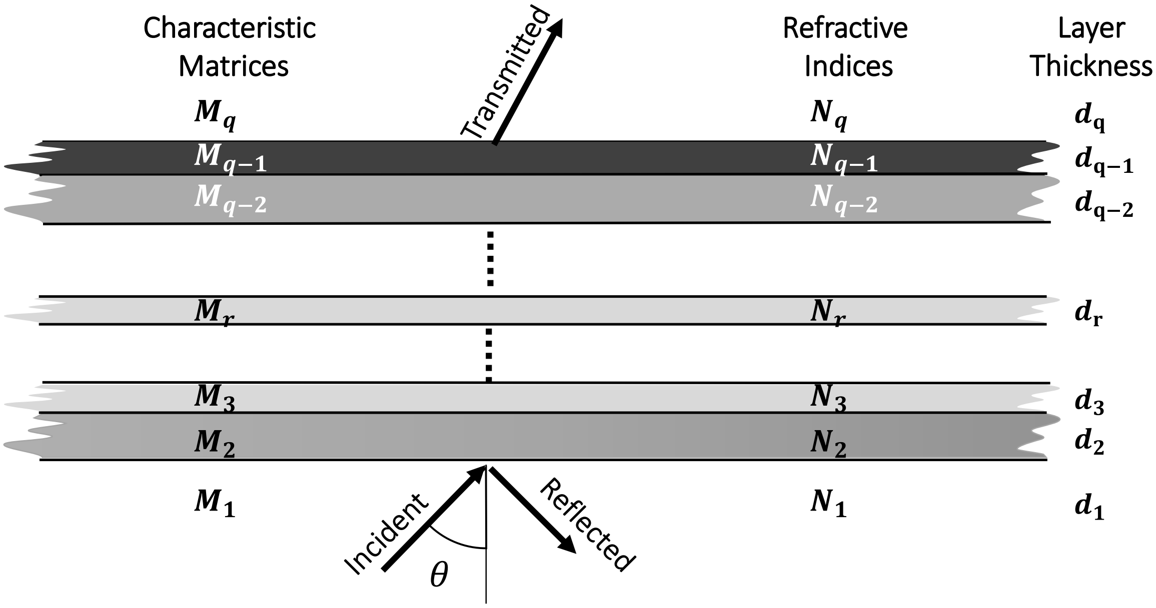

Figure 55: Schematic representation of a $\boldsymbol{q}$ assembly and how it is represented in the TMM.

As expected the coefficients for B and C in Eq. (60) revert to those for the three layer interface shown in Eqs. (42) and (43) , see Section 3.2.2.2, when q is made equal to 3. In addition, when considering the gap layer in the layer assembly, this value changes to $q = 4$ with the gap layer being represented by the subscript 3.

With the reflection coefficient for the three and four layer assemblies now defined, it is possible to extend the capabilities of the model. However, accounting for direct and in direct contact within the model will requires a simplification of the inhomogeneous cladding solid analyte interface seen under SEM analysis below. When outlining the nature of the inhomogeneous interface that would be considered in Section 5.1, restrictions were placed on the length of each individual gap as well as the space between consecutives gaps on the interface.

5.3 Observation of graphite electrode solid analyte contact surface

As previously mentioned, the interface of a solid analyte on a fiber sensing surface is to be investigated using a graphite material that was pressed onto the surface of a fabricated FOEWS. The specific type of graphite studied here was used as the anode electrode in in-house lithium-ion battery cells fabricated in a pouch cell configuration [89] and prepared specifically for this purpose. In these batteries, the anode electrode is composed of a 50 μm thick composite graphite layer deposited onto a 9 μm copper foil sheet. The graphite electrode material was obtain from MTI Corporation under the product name Li-Ion Battery Anode – Copper foil single side coated by CMS Graphite [90]. The separator is composed of a 16 μm thick monolayer polyethylene membrane with a double side ceramic 0.75 μm thick alumina coating. The separator material is a ceramic coated membrane obtained from MTI Corporation [91].

During fabrication of the lithium-ion cell, the FOEWS is sandwiched between the anode electrode and separator layers of the lithium-ion battery cell as depicted in Figure 56.

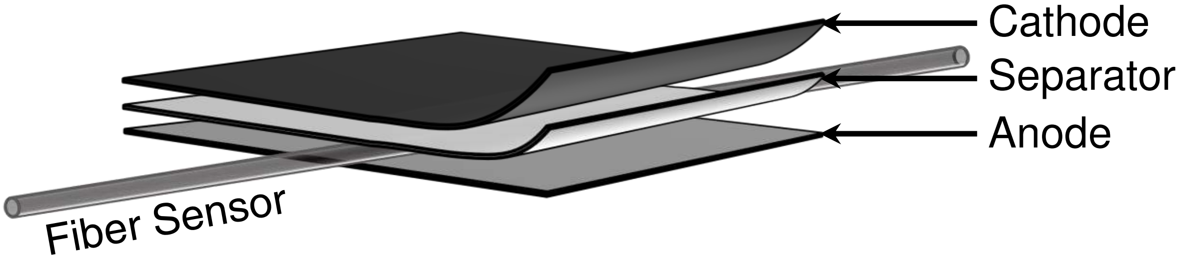

Figure 56: Cross section schematic of fiber placement in contact with an anode electrode within a lithium-ion battery cell. The entire battery in encased inside a pouch cell with only the fiber sensor and terminals exiting the pouch. Contact between the sensor and anode is ensured by applying pressure to the pouch cell after fabrication.

To ensure that proper contact is made with the anode layer, the fabricated pouch cell is place under a set weight of 6 lbs. The application of this weight helps to imprint the fiber into the graphite material. After upwards of 100 hours of battery operation and upon disassembly of the pouch cell, an indentation of the fiber in the graphite is clearly visible. Figure 57 shows an SEM image of the fiber indentation into the graphite electrode. Using the measurement scale of the SEM image, the width of the fiber trench was estimated to be approximately 106 μm across which falls within the expected width of the

FOEWS diameter at the sensing region. Therefore, it is safe to assume that the set weight of 3 lbs used to embed the fiber into the electrode is enough to cover half of the sensor with the graphite. The SEM picture also shows that the morphology of the indented graphite surface is different than that of the unaltered bed. Hence, embedding the fiber into the graphite tends to flatten the particles allowing for a smoother interface between the FOEWS and the graphite material. While the particles have been flattened to make smooth contact with the FOEWS, Figure 57 clearly shows that there remains a significant number of gaps in between flattened particles which result in gaps in the solid analyte cladding interface. From the image it can be seen that the gaps range in size from as large as 10 µm down to 1 µm or lower. As discussed in the previous section, the modification to the model to allow for partial contact with a solid analyte is designed to work when the dimensions of the partial contact structure are larger than the wavelength of light sent propagating through the optical fiber. The light source used in the analysis of the graphite anode had a wavelength of 850 nm which was chosen based on the work done by Norris et al. in [89]. Considering this wavelength, and that the dimensions of the gap structure are between 1-10 µm, the appropriate range of tolerances exist so as to expect that the assumptions made to account for a partial contact interface in the previous section will remain valid here.

Now that the surface structure of a solid graphite analyte with an embedded FOEWS has been investigated and deemed appropriate for partial contact analysis using the adjusted model, an appropriate average characteristic gap depth and contact fraction must be found. The area outlined within the dotted rectangular region of Figure 57 will be used as a representative sample region.

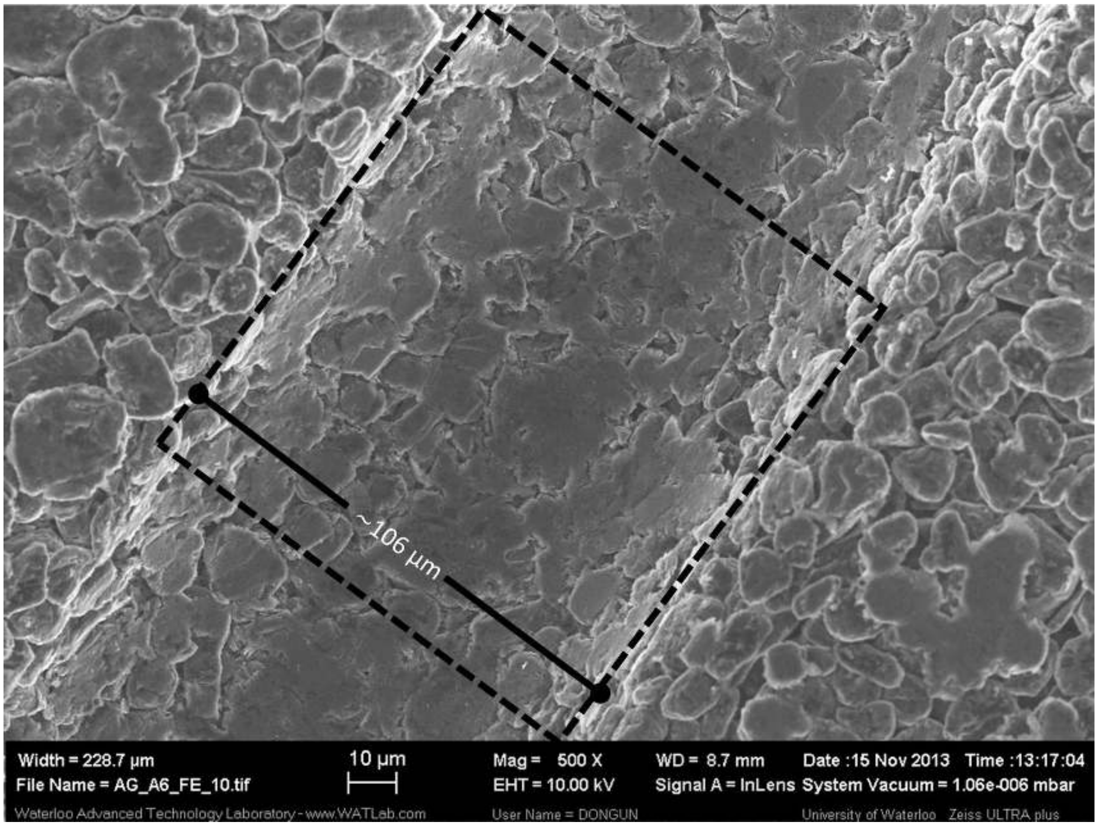

Figure 57: SEM image of a solid graphite electrode from a dissembled battery cell. Image shows fiber sensor indentation clearly demonstrating partial contact of the fiber and solid analyte.

In order to determine the area fraction of contact present within the rectangular region of Figure 57, the image was imported into the open source software ImageJ for analysis [92]. Using the *analyze particle* algorithm within ImageJ, the boundaries between the contact and non-contact regions of the graphite surface where found. After boundary tracking the image was converted to black and white as shown in Figure 58. The white portion represents regions of full contact while the black region showing the gaps in the interface.

With the image now in black and white the area contact ratio is easily determined by the *measure* command which gives the average grayscale value of the black and white image that is easily converted to a ratio of contact to non-contact regions.

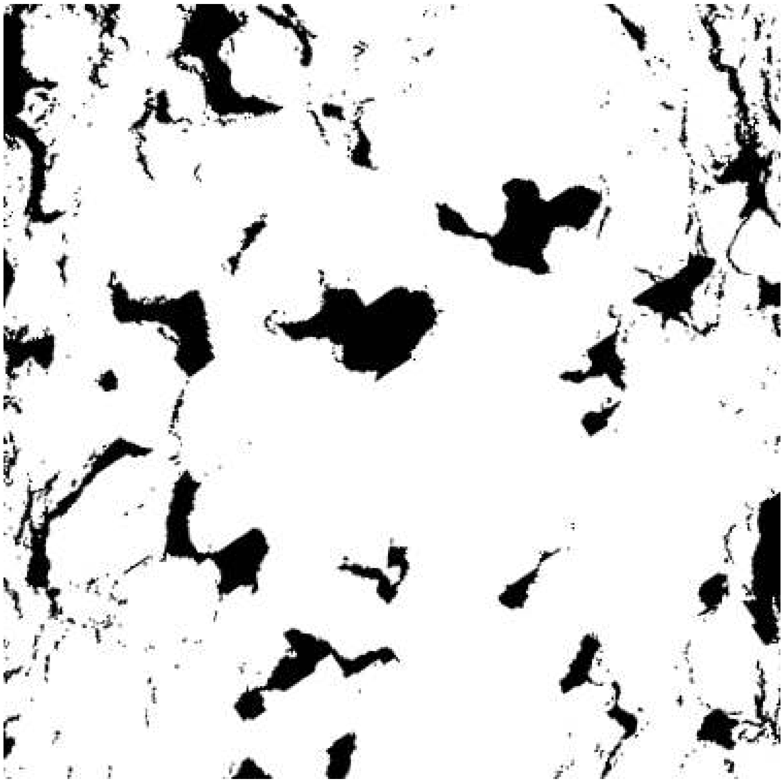

Figure 58: Resulting black and white image of the framed portion of the indented SEM image of Figure 57. This view is a planar projection of the actual cylindrical surface.

To determine the area ratio of contact and non-contact regions from Figure 58, the *measurement tool* in ImageJ was used to give the area statistics of the image. When applied to the entire image surface a mean value of pixel gray value is obtained. With a black and white image, the possible gray values range from 0 for black to 255 for white pixels. The summary of the measurement results for Figure 58 find a mean pixel value of 222.960 which converted to a percentage results in an estimated 87.1 % direct contact of the solid analyte.

The SEM image gives a top down view of the fiber indentation surface, which effectively projects the cylindrical surface onto a plane distorting the actual contact surface on the sidewalls of the trench. This distortion compresses the sidewalls of the surface on the image when viewed from the planar projection of the SEM image of Figure 57. As a result of this compression from the projection of a cylindrical surface onto a plane, the ratio of contact obtained by the ratio of black to white pixels in the projected view does not properly represent the actual contact ratio on the cylindrical surface. In order to account for the distortion due to the project, a reverse transformation of the projected image back to a cylindrical surface must be made. Mathematically the projection of a plane to a unit cylinder along the y-axis is done under the transformation given by:

$$\begin{aligned} x &\to x \\ y &\to y \\ z &\to x^2 + y^2 \end{aligned} . \tag{61}$$

By applying the transformation of Eq. (61) to the image of Figure 58, view the reconstructed three dimensional representation of the cylindrical indentation surface can be made as shown in Figure 59. The transformation mapping removes the distortion on the edges of the channel so that the resulting surface has a more homogeneous pattern than what was seen in the original image. While the contact pattern does seem more homogeneous when transformed to the cylindrical surface, some distortion in the pixel pattern does arise do to the interpolation method used to associate color values to the added pixels on the new surface. The interpolation algorithm utilized by Matlab® to associate the pixel values of the newly added pixels uses a linear interpolation method which assigns a gray value to the image based on a linear fit of the neighboring original pixels. Make note that this results in the reappearance of gray valued pixels that were removed in the thresholded image. Therefore, a secondary thresholding will be required to return the image to a binary color map.

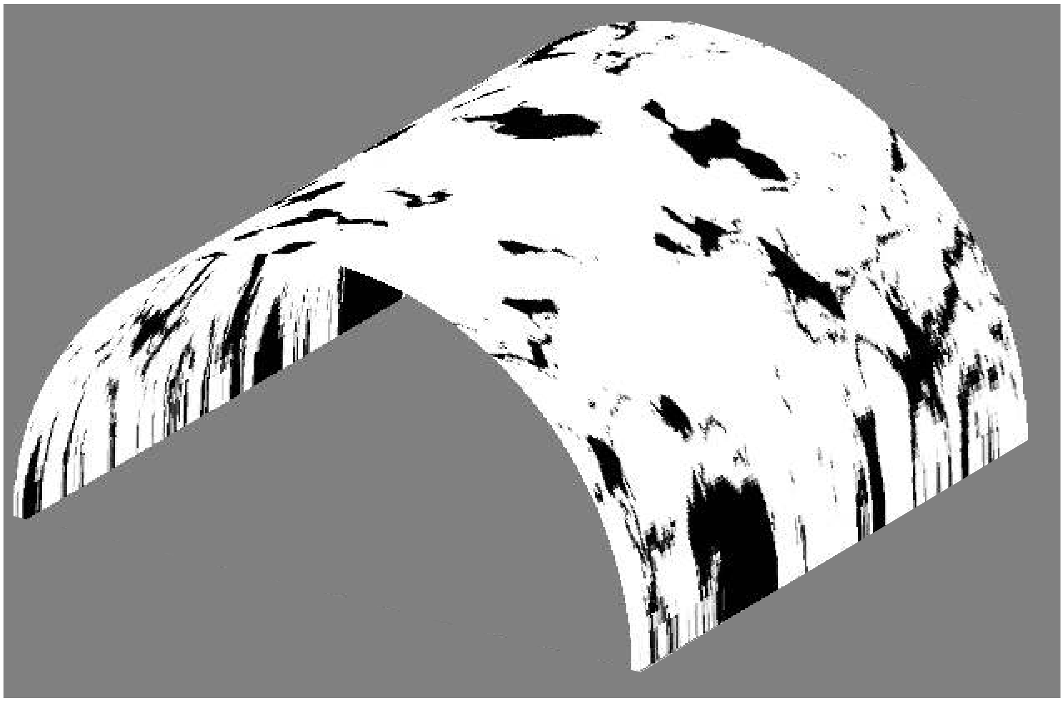

Figure 59: Projection of Figure 58 onto a cylindrical surface. Under this transformation, the distortion near the vertical walls of the channel are removed.

While the cylindrical representation of the fiber bed contact in Figure 59 is informative, the surface needs to be mapped to a plane without changing the black to white area ratio in order to submit it for measure analysis using ImageJ. Fortunately, the unwrapping of a cylinder to convert it to a plane is an area preserving transformation that is described by [93]:

$$\begin{aligned} x &\rightarrow \operatorname{asin}(x) \\ y &\rightarrow y \\ z &\rightarrow 1 \end{aligned} \quad . \tag{62}$$

This transformation maps the pixels of the original image in Figure 58 directly to the planar image of Figure 60 without the need to map the to an intermediary cylindrical surface. From the transformation equations of Eq.(62) it is clear how the image is stretched non-linearly along the x-axis, perpendicular to the fiber bed, while keeping the dimensions in the y-axis unaltered. The nonlinear stretch in the x-axis accomplished by the arc sine function applies little to know stretch to the center of the image corresponding to the bottom of the fiber indentation. Conversely, the pixels away from the center of the indentation are skewed appropriately to invert the projection distortion arising from the overhead perspective of the SEM image.

Figure 60 shows the output image of Figure 58 having gone under the mapping of Eq.(62). Additionally, as mentioned, the image was thresholded again to remove the gray valued pixels which appeared due to the linear interpolation performed in Matlab®. By remapping the pixels to in an attempt to counteract the distortion due to the overhead view of the fiber indentation significant changes to the perceived morphology become apparent. Measurement analysis of the compensated image under ImageJ in contrast to the results of the uncompensated image show that the pixel area has increased to 251600 from 160000 due to the transformation of Eq. (62). Additionally, the mean pixel value is now 213.504 compared to 222.960 resulting in a new measured contact ratio of 83.2%.

Figure 60: Unwrapped cylindrical projection of Figure 59 which appropriately removes the compression of the vertical side walls of the original image in Figure 58. Analysis of this view indicates a contact percentage of 83.2%.

This difference of 4% demonstrates the need to account for visual distortions in the SEM due to projections of the cylindrical indentation onto the planar image. In addition to the measurement of contact ratio, the mean gap depth present in the indentation bed is crucial in order to effectively incorporate the effects of partial contact into the model described in Section 5.2 above. The depth of the gaps in contact are more difficult to properly determine from the SEM image of Figure 57, given the limited resolution of the sidewall area.

Depth measurements using SEM images on similar structures were performed by Zhong et al. in [67], [68] for the purposes of determining surface roughness parameters in hydrofluoric etch optical fibers. In Figure 61, the magnification of the fiber indentation is doubled to 1000X, giving a better view of the gap height along the vertical wall sections in the lower right and upper left corners of the image. While not a full cross section of the indentation surfaces, the outlined regions in the lower right corner clearly show that the gap depth is between 4 to 8 µm in depth. The presence of such gap depths relative to the wavelength of interest of 850 nm, used to monitor the electrode bed present an optically large domain that intuitively will impact on the expected response of the FOEWS.

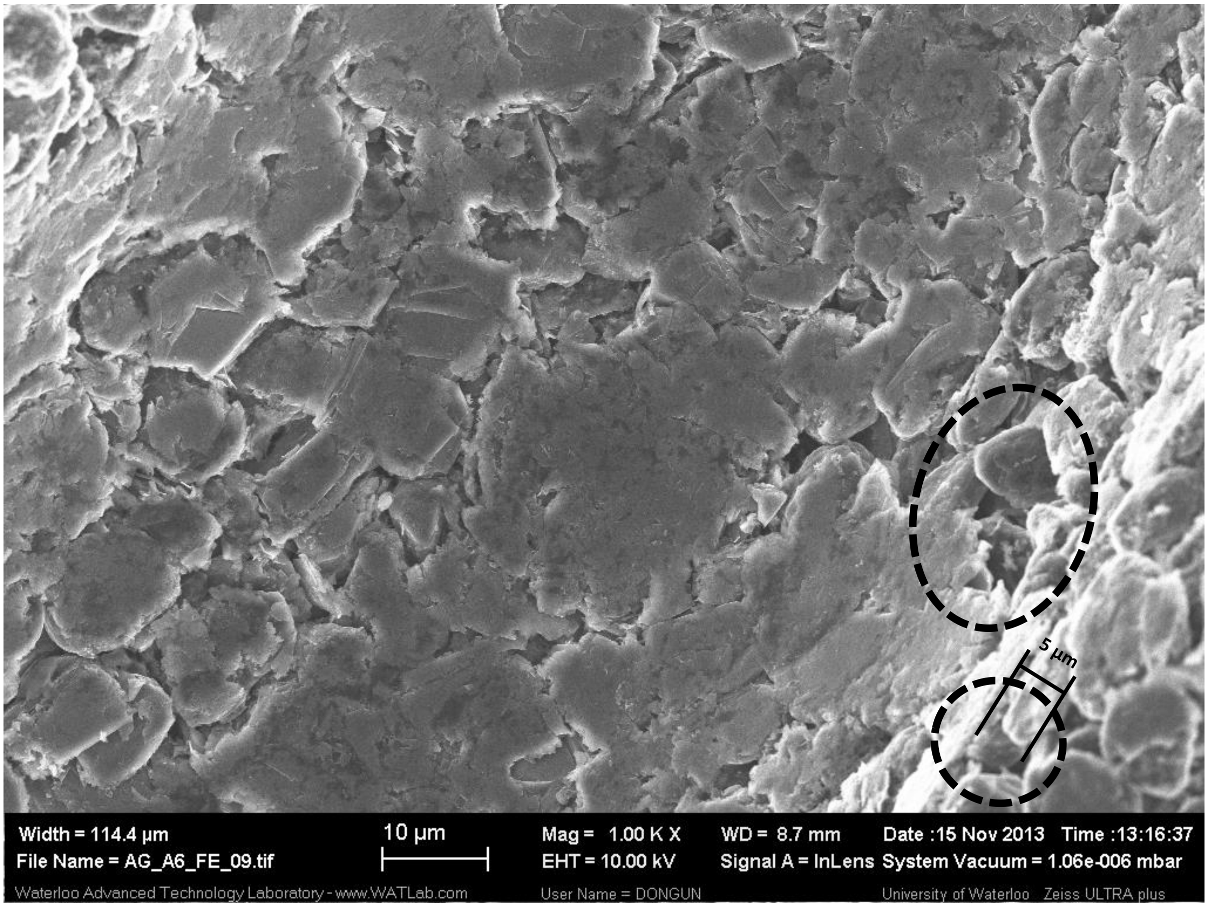

Figure 61: Enlarged view of the fiber indentation of Figure 57 under 1000X magnification. The lower right and upper left corners show near cross section view of the wall morphology. The encircled regions show the gap depth between 4 to 8 μm.

Table 2: Summary of several fiber indentation surface morphology and dimension obtained using the methodology presented above.

Electrode Sample	Contact Percentage	Mean Gap Depth ($\mu m \pm 1$)
1	83.2	5
2	60.5	5
3	63.0	5

Making use of the gap dimensions presented above, the following section makes use of the partial contact model to determine the expected change in response of the FOEWS due to variations in contact nature with a solid analyte.

5.4 Expected variations in response due to partial contact with a solid analyte

In the previous sections, both the modifications in the FOEWS model to include partial contact and a brief analysis of the contact morphology with a graphite electrode were made. The tools and inputs parameters required to investigate the effects of the contact nature on FOEWS response are present. In addition to the gap thicknesses observed above, further simulation results are presented whereby the gap thickness is reduced to optically short distances in order to demonstrate the effects that a thin liquid film present between the cladding and solid analyte layers can have on the expected FOEWS response.

The partial contact statistics that are reported in Table 2 represent the gap dimensions for contact with a graphite electrode. In practice, when the FOEWS is included in the battery fabrication as shown in Figure 56, the electrode does not envelope the entire fiber. In fact, even after the fabricated pouch cell is completed and a loading pressure is applied to maximize the contact surface, at most half of the fiber can be expected to be in contact with the electrode while the remaining portion is in contact with the separating polymer layer. Accounting for this half envelopment of the electrode on the fiber, the input contact percentage parameters of Table 2 are divided by a factor of two.

For simplicity, the material properties of the non-contact regions are chosen to match the material properties of the liquid electrolyte solutions present in the battery. The electrolyte used in the fabrication of this specific battery cell is ethylene carbonate and dimethyl carbonate (EC:DC) in a 3:7 ratio with a 1M concentration of $LiFP_6$ salt. The predicted IOR of the electrolyte mixture extrapolated from the weighted volume ratio of the IOR of the individual components. Pure ethylene carbonate has a reported IOR of 1.4158 at 50°C [94] while pure dimethyl carbonate has a reported index value of 1.368 [95]. The IOR of the electrolyte mixture can be determined from a linear combination of the refractive indices of the individual solutions [96]. Therefore, without consideration for the addition of the $LiFP_6$ salt the IOR of the binary solution can be assumed by the volume fraction:

$$N_{EC:DC} = \frac{\big(1.4158(3) + 1.368(7)\big)}{10} = 1.382. \tag{63}$$

The addition of the $LiFP_6$ salt to create the one molar solution used as the electrolyte in the fabricated cell adds an additional factor to the resulting IOR of the mixture. A study on the change in absorbance at of a binary mixture of ethylene carbonate and dimethyl carbonate under the addition of $LiFP_6$ salt was conducted by Stewart and Newman in [97]. Results of this work showed that the addition of $LiFP_6$ salt increased the absorbance of the binary solution following an affine relation in the range of zero to one molar concentrations at 250 nm wavelength. Results from 300 to 400 nm showed little to no change in absorption with the addition of $LiFP_6$. In the description of the electrolyte here it will be assumed that the absorption of the electrolyte is zero at 850 nm based on the results from [97]. A similar work on the change of the real portion of the IOR change due to the addition of $LiFP_6$ to a propylene carbonate solution for use as a battery electrolyte. Results obtained using holographic interferometry that the real portion of the IOR changed according to the relation [98].

$$N_{LiFP_6\,PC} = 1.422 - 0.0071C. \tag{64}$$

Where C is the molar concentration of $LiFP_6$. This limited changed in the real IOR of propylene carbonate solutions with the addition of $LiFP_6$, allows us to assume an IOR for the EC:DC 1 molar $LiFP_6$ solution is given by Eq.(63).

In the following analyses, the polymer separator material is not considered, so that there are only two possible layer stack configurations responsible for the modulation of the light intensity. The first layer configuration considered is from the idealized direct contact of the cladding layer with the solid electrode analyte resulting in a reflection coefficient dependent on the optical properties of the analyte and the design of the sensor only. This reflection coefficient is described by the three layer stack equation presented in Section 3.2.2.2. The second type of layer stack configuration results from the indirect contact of the solid analyte and cladding layers due to the presence of an intermediary liquid electrolyte layer. Depth of the liquid electrolyte layer is taken as the mean gap depth, while its IOR is chosen as that of the electrolyte liquid. The reflection coefficient for this layer interaction is given in Section 5.2 above.

In regards to the refractive index properties of the solid analyte electrode, a simplification of the chemical change of the chemistry undergone during charging and discharging is assumed. In a lithium-ion battery with a pure graphite anode, the effects of charging the battery result in the lithiation and de-lithiation of the anode material. A theoretically fully discharged battery would result an anode composed entirely of pure graphite. The process of charging the battery results in the lithiation of the graphite material through several intercalation stages. Each intercalation stage is characterized by the dominance of a specific lithium carbon compound. Theoretically, the process of charging a battery from full discharge to full charge takes the graphite anode composition through six distinct lithiation compounds. The work of Ohzuku et al. observed that the lithiation stages of a graphite electrode in a lithium-ion cell were characterized by the five stages summarized in the following table [99].

Table 3**:** Summary of the lithiation stages and compounds of a lithium-ion graphite electrode as observed in [99].

Lithiation Stage	**Lithium Carbon Compound**
I	LiC_6
II	LiC_{12}
III	LiC_{18}
IV	LiC_{27}
V	LiC_{36}
VI	C

Given that the chemical composition of the graphite electrode changes in chemical composition during the charging and discharging process, the expected response of the FOEWS placed in proximity to the electrode would have its response modulated according to the dominant lithium carbon compound of each stage.

For the purposes of this thesis, a simplified lithiation model of a charging and discharging anode is used to give a valid range of IOR change that can be used to evaluate the FOEWS response. This simple model assumes that the change in refractive index of a graphite electrode is interpolated between the IOR values of pure graphite and fully lithiated graphite, with chemical formula LiC_6. The interpolation function giving the refractive index at a given state of charge is given by:

$$N_{SOC} = N_C(1 - SOC) + N_{LiC_6}(SOC). \tag{65}$$

Where the value of SOC varies from 0 representing fully discharged and 1 for full charge. The value of N_{LiC_6} was obtained from work done on the reflectivity spectra analysis of stage-1 graphite intercalation compounds by Fischer et al.[100]. Using a combination of normal-incidence reflectivity and electron-energy-loss spectra along with successive Kramer-Kronig analyses, the complex permittivity of LiC_6 was determined. Converting to an optical constants, the refractive index of LiC_6 and 850 nm was found to be:

$$N_{LiC_6} = 2.3032 + i2.3987. \tag{66}$$

The IOR of graphite is given by Djurišić and Li as [101]:

$$N_C = 3.0761 + i1.8101. \tag{67}$$

The linear interpolation of the anode refractive index provides a simple model for the chemical change occurring during charging and discharging of the battery without accounting for the presence of the different intercalation stages summarized in Table 3. However, it is used here to give an expected response change of a FOEWS embedded in lithium-ion battery cell.

In order to simulate the response from a mixture of direct and partial contact of the solid analyte with the sensing region of the FOEWS, two separate sensing geometries are set up. The two sensing regions represent direct and indirect contact, and use the appropriate reflection coefficient for each. The length of the each region is then determined using the direct contact area percentage which can be determined from the investigation of the SEM of the fiber indentation surface on the graphite material as done in the previous section.

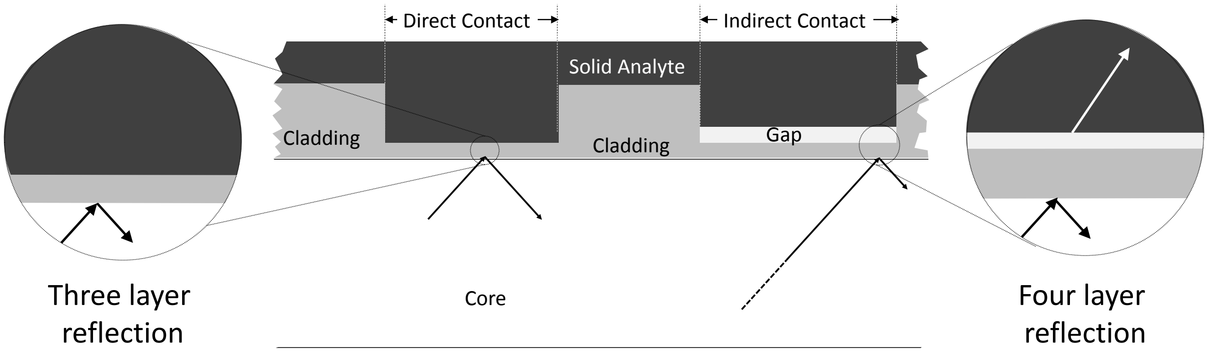

Figure 62: Schematic showing modified geometry of partial contact interface used to describe the inhomogeneous contact interface show in Figure 54.

Figure 62 illustrates the equivalent sensing interface of Figure 54 after the inhomogeneous interface has been represented by a combination of direct and indirect contact regions as described above. This representation of the inhomogeneous interface remains a valid representation so long as both the gap and contact surface areas remain optically long as described in the onset of Section 5.1. In the following section, simulation results are presented that will give insights into the effects of the gap thickness, and direct to indirect contact ratios on the expected performance response of an FOEWS.

5.5 Simulated effects of contact nature of FOEWS response

With the characterization of the solid analyte cladding interface completed in the previous section, this section makes use of the indirect contact simulation capabilities of the FOEWS model to derive insights into the relative effects of partial contact of the expected response of a FOEWS in proximity to a charging lithium-ion cell graphite electrode.

5.5.1 Effect of electrolyte gap depth on sensitivity

The graph presented in Figure 63 demonstrates the effects of a deeper gap depth caused by deeper wells of electrolyte between the cladding and electrode materials. The simulations were run for a FOEWS with a sensing length of 1 cm with a cladding thickness of 0.5 µm and no tilt angle of the LED assuming 50 % full contact of the electrode and cladding interface. For the purposes of comparison, the reference power was taken as the output power calculated for the IOR of pure graphite.

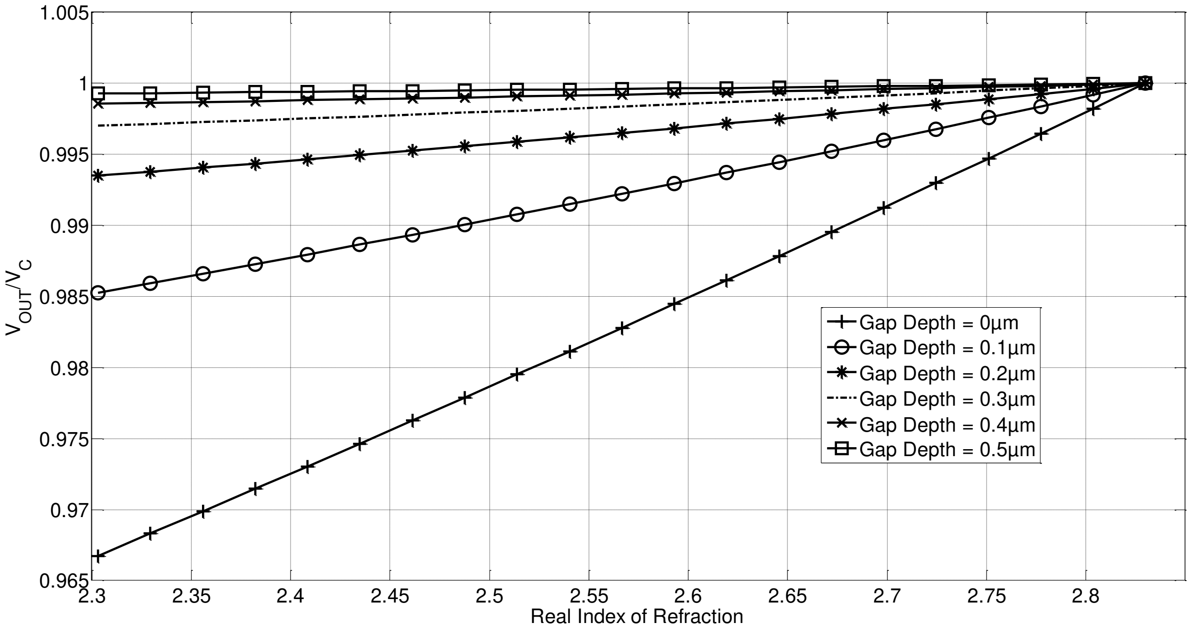

Figure 63: Simulated response behavior for a FOEWS under variations in gap depth with the assumption of full non-direct contact. Refractive index change corresponding to those of pure graphite and fully lithiated graphite.

From the simulations presented above, increasing the gap depth from 0 representing full contact to 0.5 µm has a significant effect on the sensitivity of the signal. At zero gap depth the sensitivity of the transmission response of the FOEWS is approximately 0.7 % per 0.1 refractive units while the presence of a 0.5 µm gap depth between half of the sensing surface results in a sensitivity of only 1.4e-2 % per refractive units. Such a change in sensitivity predictions indicates that the presence of a gap between the cladding and electrode surfaces must be kept at a minimum in order to provide the best monitoring of the optical properties of the electrode during charge cycling.

5.5.2 Effect direct to indirect contact ratio on transmission intensity

The ratio of direct to indirect contact of the electrode and cladding surfaces can be varied with the outside application of pressure to the battery pouch cell. A pressure test was performed on a pouch cell which contained a FOEWS in contact with the anode electrode as described in Figure 56. The test was performed by placing known weights on a monitored pouch cell held at a constant state of charge. The transmission response of the FOEWS while weight was applied to the pouch cell is summarized in Figure 64.

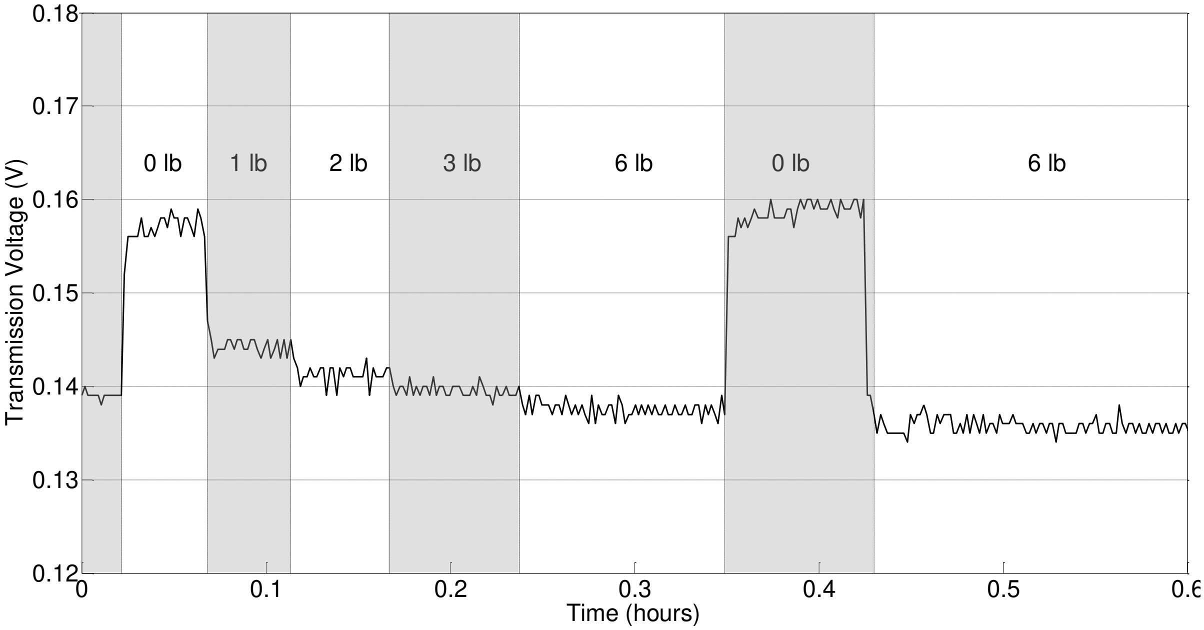

Figure 64: Measured transmission response of FOEWS in a pouch cell during weight application to the cell. Results show the decrease in transmission intensity when the applied weight is increased. Gray shadings are used to distinguish the different weighted regions.

From the measured results the change in transmission voltage decreases with the pressure loaded onto the pouch cell. The largest drop in transmission intensity occurs with the initial addition of 1 lb. to the cell and decreases less with the addition of further weight. Removal of the weight returns the lost intensity. The correlation between the transmission signal and the applied weight is summarized in Figure 65. By fitting the data to an exponential curve, it is clear that the transmission voltage has an exponential dependence on the applied weight.

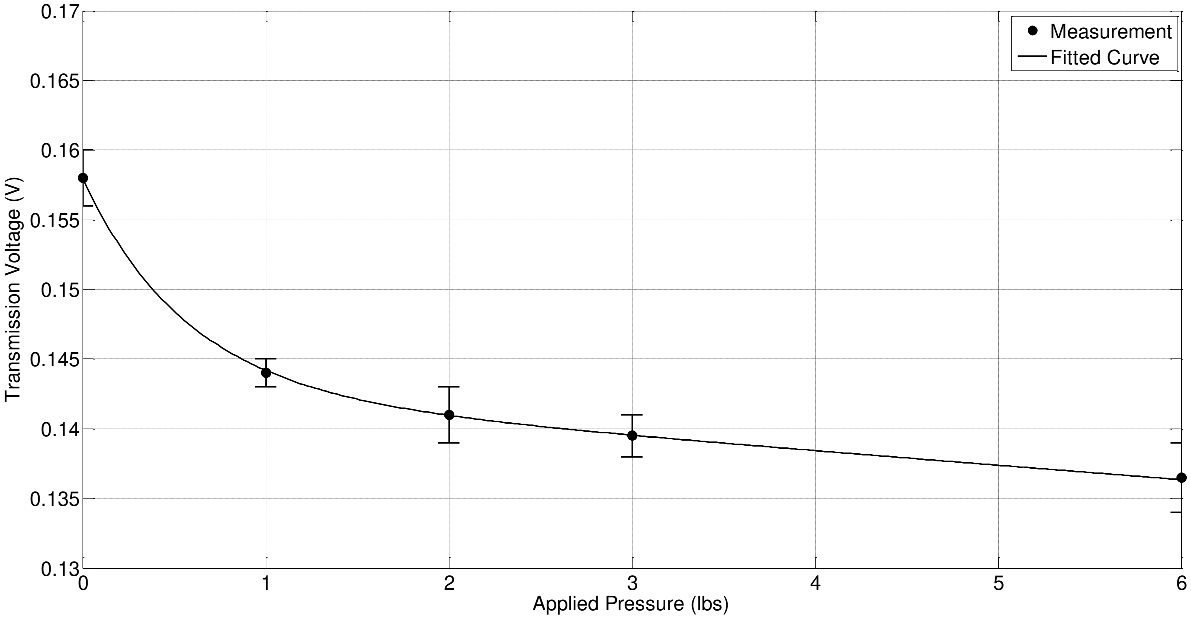

Figure 65: Transmission intensity as a function of applied pressure to the pouch cell. The behavior follows an exponential decay function

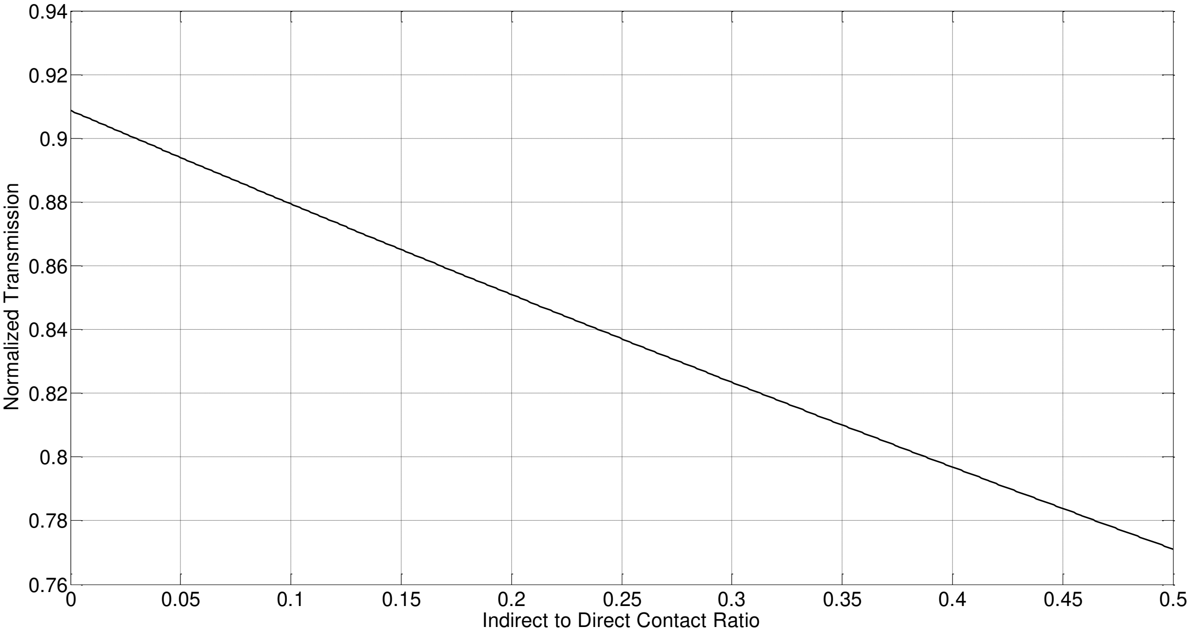

Figure 66: Predicted change in normalized transmission as a function of the contact ratio. Transmission is normalized to the calculated input power at the fiber face. Simulation parameters correspond to a sensor of 0.5 µm cladding thickness, sensing length of 1.7 cm, with a fix electrolyte gap thickness of 0.5 µm at a fixed anode IOR of 2.5.

The measured intensity as a function of applied weight follows an exponential decay behavior. In Figure 66, simulated behavior of normalized transmission response for a FOEWS with parameters: $0.5\ \mu\text{m}, 1.7\ \text{cm}, 0.5\ \mu\text{m}, 0°, 1\ \text{mm},$ for cladding thickness, sensing length, electrolyte gap depth, tilt angle, and LED source distance respectively is presented. The normalized transmission response is done at an IOR of 2.5 corresponding to 50% lithiation according to the linear model in Eq.(65), and the signal is normalized to the calculated input power at the fiber entry face. The simulation shows a negative correlation between transmission power and contact ratio. This prediction agrees in behavior with the measured results of Figure 66 in that an increase in applied pressure increases the fraction of direct contact with the graphite anode allowing for greater power loss through the sensing region. The exponential decrease of transmission as a function of applied weight is a product of the contact ratio change as a function of applied weight and is beyond the scope of this thesis.

Chapter 6

Conclusions and Future Work

6.1 Conclusion

In this thesis, an analytical model capable of modeling the transmission response behavior of a FOEWS capable of monitoring the charge cycle of a lithium-ion battery cell was presented. The sensor was fabricated by partial removal of the cladding material surrounding the core of a multimode fiber optic. The thinned cladding section allows for transmission loss via evanescing waves which radiate power out from the core as a function of the environment within a battery cell. The transmission output of the sensor can then be monitored and used to derive conclusions on the behavior of the optical and physical properties of the battery electrode material.

6.2 Contributions of thesis

6.2.1 Development of an analytical model capable of predicting the transmission response of a FOEWS sensor by direct simulation of the thin film tunneling losses along the sensing region

The main contribution of the hybrid FOEWS model is its ability to simulate the transmission response of a sensor by computing the reflection coefficient off the thin cladding interface directly and not using an effective coefficient. Using the transfer matrix method to solve the optical tunneling of rays through the thin cladding region as presented in Section 3.2.2 provides an analytical equation based solely on the IOR values of the core cladding and external media and the thickness of the cladding. The ability to compute the reflection coefficient directly by solving the electromagnetic wave equations accurately and efficiently with the transfer matrix method instead of using effective absorption parameters has, to our knowledge, not been applied to the modeling of evanescent wave sensors.

6.2.2 Use of the index of minimum transmission of the FOEWS response to characterize cladding thickness

Using the analytically derived FOEWS model to investigate the transmission response behavior as a function of wavelength, a new method for the characterization of cladding thickness was found. The index of minimum transmission of a FOEWS was found to change solely as a function of the cladding thickness. This behavior was exploited in order to accurately determine the cladding thickness of a fabricated FOEWS without relying on the absolute intensity output of a sole IOR measurement.

6.2.3 Derivation of the intensity and angular distribution of illumination conditions from an LED source onto the fiber face

The equations governing the distribution of light rays propagating within the FOEWS based on the direct illumination of the fiber with a Lambertian LED source were calculated. These equations were then used as the excitation parameters for the FOEWS model allowing for experimental validation of the FOEWS model using measured transmission response behavior of a fabrication FOEWS exposed to thermo-optic calibration oils. Simulated transmission behavior of the model was found to agree with experimental results within an accuracy of 0.1 μm in cladding thickness over a measured range in refractive index values from 1.43 to 1.466.

6.2.4 Characterization of the contact nature between a solid graphite electrode and FOEWS

A new method was develop to determine the effect of a partial contact interface between a FOEWS and a lithium-ion graphite anode using SEM analysis. Observations showed that the interface surface was not uniform and homogeneous but instead was made up of a mix of indirect and direct contact regions with morphologies that were an order of magnitude larger than the interrogation wavelength used to monitor the electrode with the FOEWS. An empirical method for characterizing the contact surface using the mean contact ratio and mean indirect contact gap was calculated from the SEM pictures was developed.

Using the transfer matrix method, the three layer reflection coefficient used to predict the transmission loss in a FOEWS in full direct contact with the analyte material was extended to four layers in order to account for a gap layer separating the analyte from the FOEWS sensing surface. The three and four layer reflection coefficients were then utilized to develop a model capable of predicting the response behavior of a FOEWS in partial contact with a solid analyte media. The ability to account for the partial contact by including a fourth layer in the calculation of the transmission loss of the FOEWS has to our knowledge not been demonstrator previously.

6.3 Proposed future work

Some potential extensions of the presented research work are presented in this section. They are categorized in three main groups as follow:

6.3.1 Modeling and Optimization

- *Improving the parameter determination algorithm*: for example, in this research, the cladding thickness of a fabrication FOEWS was determined by first identifying the index of minimum transmission to find the cladding thickness after which the illumination conditions were adjusted in order to improve the model predictions. An algorithm capable of simultaneously fitting all model parameters to the experimental data would improve the accuracy of the model.
- *Mechanical model of the partial contact of the surface*: the sensing region of the fiber embeds itself into the graphite electrode of the pouch cell based on the applied pressure to the cell. A mechanical model capable of predicting the change in direct contact between the electrode and fiber sensing region as a function of the cylindrical geometry of the fiber and pressure applied to deform the electrode bed would be able to optimize the sensing capabilities of the FOEWS within the battery cell.

6.3.2 Experiments and test setups

- *Use of the FOEWS as novel refractometer*: in combination with the predicted response behavior of the model and accurate mapping of the transmission response of a FOEWS using a wider range of thermo-optic oils, the temperature dependent IOR of liquids can measured based on the transmission response.
- *Characterization of the refractive index change of the anode*: by accurately determining the refraction indices of the graphite electrode at each of the lithiation states undergone during charge cycling, the FOEWS response can be mapped directly to state of charge of the lithium-ion cell.

Bibliography

[1] D. G. O'Keeffe, "Development of fibre optic evanescent-wave fluorescent-based sensors," doctoral, Dublin City University. School of Physical Sciences, 1995.

[2] B. H. Lee, Y. H. Kim, K. S. Park, J. B. Eom, M. J. Kim, B. S. Rho, and H. Y. Choi, "Interferometric Fiber Optic," *Sensors*, vol. 12, no. 3, pp. 2467–2486, Feb. 2012.

[3] E. Udd, "An overview of fiber-optic sensors," *Rev. Sci. Instrum.*, vol. 66, no. 8, pp. 4015–4030, Aug. 1995.

[4] W. Lin, C. Zhang, L. Li, and S. Liang, "Review on Development and Applications of Fiber-Optic Sensors," in *2012 Symposium on Photonics and Optoelectronics (SOPO)*, 2012, pp. 1–4.

[5] K. Rahnavardy, V. Arya, A. Wang, and J. M. Weiss, "Investigation and application of the frustrated-total-internal-reflection phenomenon in optical fibers," *Appl. Opt.*, vol. 36, no. 10, pp. 2183–2187, Apr. 1997.

[6] J., W. B. Spillman and D. H. McMahon, "Frustrated-total-internal-reflection multimode fiber-optic hydrophone," *Appl. Opt.*, vol. 19, no. 1, pp. 113–117, Jan. 1980.

[7] I. N. Court and F. K. von Willisen, "Frustrated Total Internal Reflection and Application of Its Principle to Laser Cavity Design," *Appl. Opt.*, vol. 3, no. 6, pp. 719–726, Jun. 1964.

[8] K. Försterling, "By measuring the optical constants of a very thin metal layers," *Ann. Phys.*, vol. 422, no. 8, pp. 745–751, Jan. 1937.

[9] J. M. Guerra, "Photon tunneling microscopy," *Appl. Opt.*, vol. 29, no. 26, pp. 3741–3752, Sep. 1990.

[10] P. Nath, H. K. Singh, P. Datta, and K. C. Sarma, "All-fiber optic sensor for measurement of liquid refractive index," *Sens. Actuators Phys.*, vol. 148, no. 1, pp. 16–18, Nov. 2008.

[11] S. Simhony, E. M. Kosower, and A. Katzir, "Novel attenuated total internal reflectance spectroscopic cell using infrared fibers for aqueous solutions," *Appl. Phys. Lett.*, vol. 49, no. 5, pp. 253–254, Aug. 1986.

[12] P. Paul, "A miniature fiber-optic probe for optical particle sizing," *Light. Technol. J. Of*, vol. 5, no. 7, pp. 967–971.

[13] M. D. DeGrandpre and L. W. Burgess, "Long path fiber-optic sensor for evanescent field absorbance measurements," *Anal. Chem.*, vol. 60, no. 23, pp. 2582–2586, Dec. 1988.

[14] H. Tai, T. Yoshino, and H. Tanaka, "Fiber-optic evanescent-wave methane-gas sensor using optical absorption for the 3.392-μm line of a He-Ne laser," *Opt. Lett.*, vol. 12, no. 6, pp. 437–439, Jun. 1987.

[15] A. Messica, A. Greenstein, and A. Katzir, "Theory of fiber-optic, evanescent-wave spectroscopy and sensors," *Appl. Opt.*, vol. 35, no. 13, pp. 2274–2284, May 1996.

[16] M. P. Buric, P. Ohodnicki, and B. Chorpening, "Theoretical and experimental investigation of evanescent-wave absorption sensors for extreme temperature applications," 2013, vol. 8816, p. 88160N–88160N–16.

[17] P. K. Choudhury, “Dispersion Behavior of Gold-Nanocoated Dielectric Optical Fibers,” *Adv. Mater. Sci. Eng.*, vol. 2012, Sep. 2012.

[18] M. A. Baqir and P. K. Choudhury, “Effects on the Energy Flux Density Due to Pitch in Twisted Clad Optical Fibers.,” *Prog. Electromagn. Res.*, vol. 139, pp. 643–654, 2013.

[19] M. Ghasemi and P. K. Choudhury, “On the sustainment of optical power in twisted clad dielectric cylindrical fibers,” vol. 27, no. 11, pp. 1382–1391, Jul. 2013.

[20] R. Pieper, M. Shirvaikar, and J. Salvatierra, “A transmission line model for analysis of thin film optical filters,” in *Proceeding of the Thirty-Eighth Southeastern Symposium on System Theory, 2006. SSST ’06*, 2006, pp. 186–191.

[21] M. Born and E. Wolf, *Principles of Optics: Electromagnetic Theory of Propagation, Interference and Diffraction of Light*. Cambridge University Press, 1999.

[22] F. T. Ulaby and Ulaby, Fawwaz T., *Fundamentals of Applied Electromagnetics*, 5th ed. Pearson Education, 2007.

[23] P. Yeh, *Optical Waves in Layered Media (Pure & Applied Optics)*, Illustrated edition. John Wiley & Sons, 1988.

[24] S. Hayashi, H. Kurokawa, and H. Oga, “Observation of Resonant Photon Tunneling in Photonic Double Barrier Structures,” *Opt. Rev.*, vol. 6, no. 3, pp. 204–210, May 1999.

[25] A. Q. Jian and X. M. Zhang, “Resonant Optical Tunneling Effect: Recent Progress in Modeling and Applications,” *IEEE J. Sel. Top. Quantum Electron.*, vol. 19, no. 3, pp. 9000310–9000310, May 2013.

[26] R. A. Oliveira, “Numerical approach for designing a Bragg grating acousto-optic modulator using the finite element and the transfer matrix methods,” *Opt. Commun.*, vol. 281, no. 19, pp. 4899–4905, Oct. 2008.

[27] C. A. F. Marques, L. Bilro, L. Kahn, R. A. Oliveira, D. J. Webb, and R. N. Nogueira, “Acousto-Optic Effect in Microstructured Polymer Fiber Bragg Gratings: Simulation and Experimental Overview,” *J. Light. Technol.*, vol. 31, no. 10, pp. 1551–1558, May 2013.

[28] R. Mahakud, O. Prakash, J. Kumar, S. V. Nakhe, and S. K. Dixit, “Analysis on the effect of UV beam intensity profile on the refractive index modulation in phase mask based fiber Bragg grating writing,” *Opt. Commun.*, vol. 285, no. 24, pp. 5351–5358, Nov. 2012.

[29] R. A. Oliveira, K. Cook, J. Canning, and A. A. P. Pohl, “Bragg grating writing in acoustically excited optical fiber,” *Appl. Phys. Lett.*, vol. 97, no. 4, p. 041101, Jul. 2010.

[30] R. A. Oliveira, J. Canning, K. Cook, and A. A. P. Pohl, “Complex Bragg grating writing in acoustically excited optical fiber,” in *2010 35th Australian Conference on Optical Fibre Technology (ACOFT)*, 2010, pp. 1–3.

[31] R. A. Oliveira, G. R. C. Possetti, C. A. F. Marques, P. T. N. Jr, K. Cook, R. C. Kamikawachi, C. Bavastri, J. L. Fabris, M. Muller, R. N. Nogueira, J. Canning, and A. A. P. Pohl, “Control of the long period grating spectrum through low frequency flexural acoustic waves,” *Meas. Sci. Technol.*, vol. 22, no. 4, p. 045205, Apr. 2011.

[32] C. A. F. Marques, R. A. Oliveira, J. Canning, A. A. P. Pohl, and R. N. Nogueira, “Control of the properties of fiber Bragg gratings based on the acousto-optic effect,” in *2010 36th European Conference and Exhibition on Optical Communication (ECOC)*, 2010, pp. 1–3.

[33] R. E. Silva, M. A. R. Franco, P. T. Neves, H. Bartelt, and A. A. P. Pohl, “Detailed analysis of the longitudinal acousto-optical resonances in a fiber Bragg modulator,” *Opt. Express*, vol. 21, no. 6, pp. 6997–7007, Mar. 2013.

[34] C. A. F. Marques, R. A. Oliveira, A. A. P. Pohl, and R. N. Nogueira, “Tunability of the FBG group delay through acousto-optic modulation,” *Opt. Fiber Technol.*, vol. 19, no. 2, pp. 121–125, Mar. 2013.

[35] C. A. F. Marques, R. A. Oliveira, and R. N. Nogueira, “Tunable narrow dispersion compensation for independent CWDM channels using the acousto-optic modulation,” *Microw. Opt. Technol. Lett.*, vol. 55, no. 4, pp. 929–932, Apr. 2013.

[36] R. A. Oliveira, P. T. Neves Jr., J. T. Pereira, J. Canning, and A. A. P. Pohl, “Vibration mode analysis of a silica horn–fiber Bragg grating device,” *Opt. Commun.*, vol. 283, no. 7, pp. 1296–1302, Apr. 2010.

[37] KRETSCHM.E and H. RAETHER, “RADIATIVE DECAY OF NON RADIATIVE SURFACE PLASMONS EXCITED BY LIGHT,” *Z. NATURFORSCHUNG PART -Astrophys. Phys. Phys. Chem.*, vol. A 23, no. 12, p. 2135–&, 1968.

[38] J. Čtyroky´, “Modelling of surface plasmon resonance waveguide sensor by complex mode expansion and propagation method,” *Opt. Quantum Electron.*, vol. 29, no. 2, pp. 301–311.

[39] J. Čtyroký, J. Homola, P. V. Lambeck, S. Musa, H. J. W. M. Hoekstra, R. D. Harris, J. S. Wilkinson, B. Usievich, and N. M. Lyndin, “Theory and modelling of optical waveguide sensors utilising surface plasmon resonance,” *Sens. Actuators B Chem.*, vol. 54, no. 1–2, pp. 66–73, Jan. 1999.

[40] J. Chilwell and I. Hodgkinson, “Thin-films field-transfer matrix theory of planar multilayer waveguides and reflection from prism-loaded waveguides,” *J. Opt. Soc. Am. A*, vol. 1, no. 7, pp. 742–753, Jul. 1984.

[41] R. D. Harris and J. S. Wilkinson, “Waveguide surface plasmon resonance sensors,” *Sens. Actuators B Chem.*, vol. 29, no. 1–3, pp. 261–267, Oct. 1995.

[42] M. Kanso, S. Cuenot, and G. Louarn, “Sensitivity of Optical Fiber Sensor Based on Surface Plasmon Resonance: Modeling and Experiments,” *Plasmonics*, vol. 3, no. 2–3, pp. 49–57, Sep. 2008.

[43] Lin, Yu-Cheng. “A Fiber-Optic Alcohol Sensor Based on Surface Plasmon Resonance.” Microwave and Optical Technology Letters 56, no. 3 (March 1, 2014): 766–69. doi:10.1002/mop.28140.

[44] Zhao, Yong, Ze-qun Deng, and Qi Wang. “Fiber Optic SPR Sensor for Liquid Concentration Measurement.” Sensors and Actuators B: Chemical 192 (March 1, 2014): 229–33. doi:10.1016/j.snb.2013.10.108.

[45] R. Bharadwaj, “Gold nanoparticle coated U-bend fibre optic probe for localized surface plasmon resonance based detection of explosive vapours,” vol. 192, no. 1–2, pp. 804–811.

[46] S. K. Mishra, S. Rani, and B. D. Gupta, “Surface plasmon resonance based fiber optic hydrogen sulphide gas sensor utilizing nickel oxide doped ITO thin film,” *Sens. Actuators B Chem.*, vol. 195, pp. 215–222, May 2014.

[47] N. Cennamo, D. Massarotti, L. Conte, and L. Zeni, “Low Cost Sensors Based on SPR in a Plastic Optical Fiber for Biosensor Implementation,” *Sensors*, vol. 11, no. 12, pp. 11752–11760, Dec. 2011.

[48] N. Cennamo, D. Massarotti, R. Galatus, L. Conte, and L. Zeni, “Performance Comparison of Two Sensors Based on Surface Plasmon Resonance in a Plastic Optical Fiber,” *Sensors*, vol. 13, no. 1, pp. 721–735, Jan. 2013.

[49] L. Liu, J. Yang, Z. Yang, X. Wan, N. Hu, and X. Zheng, “Theoretical Analysis of the Optical Propagation Characteristics in a Fiber-Optic Surface Plasmon Resonance Sensor,” *Sensors*, vol. 13, no. 6, pp. 7443–7453, Jun. 2013.

[50] S. Roh, H. Kim, and B. Lee, “A comparative analysis of surface plasmon resonance fiber sensor with symmetric and asymmetric metal coating by three-dimensional ray-tracing,” 2010, pp. 778111–778111–8.

[51] T. Makiabadi, V. Le Nader, M. Kanso, and G. Louarn, “Comprehensive study of an optical fiber plasmonic microsensor in a microfluidic device,” *Eur. Phys. J. - Appl. Phys.*, vol. 56, no. 01, p. null–null, 2011.

[52] V. Ruddy, “An effective attenuation coefficient for evanescent wave spectroscopy using multimode fiber,” *Fiber Integr. Opt.*, vol. 9, no. 2, pp. 143–151, 1990.

[53] W. F. Love, L. J. Button, and R. E. Slovacek, “Optical Characteristics of Fiberoptic Evanescent Wave Sensors,” in *Biosensors with Fiberoptics*, D. L. Wise and L. B. W. Jr, Eds. Humana Press, 1991, pp. 139–180.

[54] S. P. McCabe, “An investigation of evanescent wave gas sensing using Zirconium Fluoride optical fibre,” doctoral, Dublin City University. School of Physical Sciences, 1994.

[55] R. M. Chyad, M. Z. M. Jafri, K. N. Mutter, and K. Ibrahim, “Numerical ray tracing through a modified cladding fiber optic segment sensors,” *Opt. - Int. J. Light Electron Opt.*, vol. 123, no. 10, pp. 860–862, May 2012.

[56] M. Ahmad and L. L. Hench, “Effect of taper geometries and launch angle on evanescent wave penetration depth in optical fibers,” *Biosens. Bioelectron.*, vol. 20, no. 7, pp. 1312–1319, Jan. 2005.

[57] K. A. Stasiewicz, “Influence of tapering process on changes of optical fiber refractive index distribution along a structure,” *Opto-Electron. Rev.*, vol. 18, no. 1, pp. 102–109, Mar. 2010.

[58] A. B. Socorro, “Influence of Waist Length in Lossy Mode Resonances Generated With Coated Tapered Single-Mode Optical Fibers,” *IEEE Photonics Technol. Lett.*, vol. 23, no. 21, pp. 1579–1581, Nov. 2011.

[59] A. B. Socorro, “Tapered Single-Mode Optical Fiber pH Sensor Based on Lossy Mode Resonances Generated by a Polymeric Thin-Film,” *IEEE Sens. J.*, vol. 12, no. 8, pp. 2598–2603, Aug. 2012.

[60] A. Goyal, R. Gupta, C. N. Kumar, T. Soloman Raju, and P. K. Panigrahi, “Controlling optical similaritons in a graded-index nonlinear waveguide by tailoring of the tapering profile,” *Opt. Commun.*, vol. 300, pp. 236–243, Jul. 2013.

[61] S.-M. Tseng and C.-L. Chen, “Side-polished fibers,” *Appl. Opt.*, vol. 31, no. 18, pp. 3438–3447, Jun. 1992.

[62] S. M. Chandani, A. Kulpa, and N. A. F. Jaeger, “Nondestructive determination of cladding thickness in D-fibers,” *IEEE Photonics Technol. Lett.*, vol. 18, no. 9, pp. 1082–1084, May 2006.

[63] L. Bilro, N. Alberto, J. L. Pinto, and R. N. Nogueira, “A simple and low-cost cure monitoring system based on a side-polished plastic optical fibre,” *Meas. Sci. Technol.*, vol. 21, no. 11, p. 117001, Nov. 2010.

[64] L. Bilro, N. Jordão Alberto, L. M. Sá, J. de L. Pinto, and R. Nogueira, “Analytical Analysis of Side-Polished Plastic Optical Fiber as Curvature and Refractive Index Sensor,” *J. Light. Technol.*, vol. 29, no. 6, pp. 864–870, Mar. 2011.

[65] M. R. R. Khan, B.-H. Kang, S.-W. Lee, S.-H. Kim, S.-H. Yeom, S.-H. Lee, and S.-W. Kang, “Fiber-optic multi-sensor array for detection of low concentration volatile organic compounds,” *Opt. Express*, vol. 21, no. 17, pp. 20119–20130, Aug. 2013.

[66] V. R. Machavaram, R. A. Badcock, and G. F. Fernando, “Fabrication of intrinsic fibre Fabry–Perot sensors in silica fibres using hydrofluoric acid etching,” *Sens. Actuators Phys.*, vol. 138, no. 1, pp. 248–260, Jul. 2007.

[67] N. Zhong, X. Zhu, Q. Liao, Y. Wang, R. Chen, and Y. Sun, “Effects of surface roughness on optical properties and sensitivity of fiber-optic evanescent wave sensors,” *Appl. Opt.*, vol. 52, no. 17, pp. 3937–3945, Jun. 2013.

[68] N. Zhong, Q. Liao, X. Zhu, Y. Wang, and R. Chen, “High-quality fiber fabrication in buffered hydrofluoric acid solution with ultrasonic agitation,” *Appl. Opt.*, vol. 52, no. 7, pp. 1432–1440, Mar. 2013.

[69] N. Zhong, X. Zhu, Q. Liao, Y. Wang, and R. Chen, “GeO2-SiO2-chitosan-medium-coated hollow optical fiber for cell immobilization,” *Opt. Lett.*, vol. 38, no. 16, pp. 3115–3118, Aug. 2013.

[70] G. Keiser, *Optical fiber communications*. McGraw-Hill, 2000.

[71] “Thorlabs - 0.22 NA Step-Index Multimode Fibers.” [Online]. Available: http://www.thorlabs.com/NewGroupPage9.cfm?ObjectGroup_ID=360. [Accessed: 21-May-2013].

[72] J. R. Godin and P. Nieva, “Use of a hybrid ray-thin film interference model for the optimization of a FTIR FOEWS,” 2014, p. 898008.

[73] H. A. Macleod, *Thin-film Optical Filters*. Macmillan Publishing Company, 1986.

[74] B. D. Gupta, C. D. Singh, and A. Sharma, “Fiber optic evanescent field absorption sensor: effect of launching condition and the geometry of the sensing region,” *Opt. Eng.*, vol. 33, no. 6, pp. 1864–1868, Jun. 1994.

[75] “Thorlabs - BFTU Universal Bare Fiber Terminator.” [Online]. Available: http://www.thorlabs.com/thorproduct.cfm?partnumber=BFTU. [Accessed: 31-Jul-2014].

[76] "Watlow | FIREROD Cartridge Heaters for the Heating Element Industry." [Online]. Available: http://www.watlow.com/products/heaters/firerod-cartridge-heaters.cfm?famid=1. [Accessed: 31-Jul-2014].

[77] "Watlow Mini Control Console | Temperature Controllers | Instrumart." [Online]. Available: https://www.instrumart.com/products/23665/watlow-mini-control-console. [Accessed: 31-Jul-2014].

[78] "NI USB-TC01 Thermocouple Measurement Device - National Instruments." [Online]. Available: http://sine.ni.com/nips/cds/view/p/lang/en/nid/208177. [Accessed: 31-Jul-2014].

[79] "VSLY5850 Vishay Semiconductors | Mouser," *Mouser Electronics*. [Online]. Available: http://ca.mouser.com/Search/ProductDetail.aspx?R=VSLY5850virtualkey61350000virtualkey782-VSLY5850. [Accessed: 31-Jul-2014].

[80] "Thorlabs - RMS11P RMS-Threaded Adapter for M11 x 0.5-Threaded Components." [Online]. Available: http://www.thorlabs.com/thorproduct.cfm?partnumber=RMS11P. [Accessed: 31-Jul-2014].

[81] "E3631A 80W Triple Output Power Supply, 6V, 5A & ±25V, 1A | Agilent." [Online]. Available: http://www.home.agilent.com/en/pd-836433-pn-E3631A/80w-triple-output-power-supply-6v-5a-25v-1a?&cc=CA&lc=eng. [Accessed: 31-Jul-2014].

[82] "Thorlabs - DET10C InGaAs Detector, 700-1800 nm, 10 ns Rise Time, 0.8 mm^2." [Online]. Available: http://www.thorlabs.com/thorproduct.cfm?partnumber=DET10C. [Accessed: 03-Sep-2013].

[83] "54621D Portable MSO [Obsolete] | Agilent." [Online]. Available: http://www.home.agilent.com/en/pd-1000000809%3Aepsg%3Apro-pn-54621D/portable-mso?&cc=CA&lc=eng. [Accessed: 31-Jul-2014].

[84] "Thorlabs - AFS105/125Y Multimode Fiber, 0.22 NA, Low-OH, Ø105 µm Core, Vis-IR." [Online]. Available: http://www.thorlabs.com/thorProduct.cfm?partNumber=AFS105/125Y&. [Accessed: 08-Aug-2014].

[85] I. H. Malitson, "Interspecimen Comparison of the Refractive Index of Fused Silica," *J. Opt. Soc. Am.*, vol. 55, no. 10, p. 1205, Oct. 1965.

[86] M. Daimon and A. Masumura, "Measurement of the refractive index of distilled water from the near-infrared region to the ultraviolet region," *Appl. Opt.*, vol. 46, no. 18, pp. 3811–3820, Jun. 2007.

[87] A. N. Bashkatov and E. A. Genina, "Water refractive index in dependence on temperature and wavelength: a simple approximation," 2003, vol. 5068, pp. 393–395.

[88] J. Rheims, J. Köser, and T. Wriedt, "Refractive-index measurements in the near-IR using an Abbe refractometer," *Meas. Sci. Technol.*, vol. 8, no. 6, p. 601, Jun. 1997.

[89] R. Norris, K. Iyer, V. Chabot, P. Nieva, A. Yu, A. Khajepour, and J. Wang, "Multi-band reflectance spectroscopy of carbonaceous lithium iron phosphate battery electrodes versus state of charge," 2014, vol. 8982, pp. 898214–898214–8.

[90] "Li-Ion Battery Anode -Copper foil single side coated by CMS Graphite (267mm L x 214mm W x 0.1mm Thickness) 5 sheets/bag bc-cf-267-ss," *MTI Corp - Leading provider of lab equipments*

and advanced crystal substrates. [Online]. Available: http://www.mtixtl.com/li-ionbatteryanode-copperfoilsinglesidecoatedbycmsgraphite267mm.aspx. [Accessed: 28-Jul-2014].

[91] “Ceramic Coated Membrane (16um thickness x 60mm width x 500m Length) for Li-ion Battery R&D - EQ-bsf-0016-500A,” *MTI Corp - Leading provider of lab equipments and advanced crystal substrates*. [Online]. Available: http://www.mtixtl.com/ceramiccoatedmembraneforli-ionbatteryrandd-eq-bsf-0016-500a.aspx. [Accessed: 28-Jul-2014].

[92] “ImageJ.” [Online]. Available: http://imagej.nih.gov/ij/. [Accessed: 07-Jul-2014].

[93] A. Pressley, *Elementary Differential Geometry*. Springer Science & Business Media, 2001.

[94] “Ethylene Carbonate (EC) in Dongying, Shandong, China - Dongying UPC Industry & Trade Co., Ltd.” [Online]. Available: http://www.tradeindia.com/fp638832/Ethylene-Carbonate-EC-.html. [Accessed: 16-Jul-2014].

[95] “Dimethyl carbonate, ReagentPlus®, 99% | (CH3O)2CO | Sigma-Aldrich.” [Online]. Available: http://www.sigmaaldrich.com/catalog/product/sial/d152927?lang=en&region=CA. [Accessed: 17-Jul-2014].

[96] J. Newman and T. W. Chapman, “Restricted diffusion in binary solutions,” *AIChE J.*, vol. 19, no. 2, pp. 343–348, Mar. 1973.

[97] S. G. Stewart and J. Newman, “The Use of UV/vis Absorption to Measure Diffusion Coefficients in LiPF6 Electrolytic Solutions,” *J. Electrochem. Soc.*, vol. 155, no. 1, pp. F13–F16, Jan. 2008.

[98] K. Nishikawa, Y. Fukunaka, T. Sakka, Y. H. Ogata, and J. R. Selman, “Measurement of Concentration Profiles during Electrodeposition of Li Metal from LiPF6-PC Electrolyte Solution The Role of SEI Dynamics,” *J. Electrochem. Soc.*, vol. 154, no. 10, pp. A943–A948, Oct. 2007.

[99] T. Ohzuku, Y. Iwakoshi, and K. Sawai, “Formation of Lithium-Graphite Intercalation Compounds in Nonaqueous Electrolytes and Their Application as a Negative Electrode for a Lithium Ion (Shuttlecock) Cell,” *J. Electrochem. Soc.*, vol. 140, no. 9, pp. 2490–2498, Sep. 1993.

[100] J. E. Fischer, J. M. Bloch, C. C. Shieh, M. E. Preil, and K. Jelley, “Reflectivity spectra and dielectric function of stage-1 donor intercalation compounds of graphite,” *Phys. Rev. B*, vol. 31, no. 8, pp. 4773–4783, Apr. 1985.

[101] A. B. Djurišić and E. H. Li, “Optical properties of graphite,” *J. Appl. Phys.*, vol. 85, no. 10, pp. 7404–7410, May 1999.

[102] C.-H. Chen, T.-C. Tsao, J.-L. Tang, and W.-T. Wu, “A Multi-D-Shaped Optical Fiber for Refractive Index Sensing,” *Sensors*, vol. 10, no. 5, pp. 4794–4804, May 2010.

[103] P. Polynkin, A. Polynkin, N. Peyghambarian, and M. Mansuripur, “Evanescent field-based optical fiber sensing device for measuring the refractive index of liquids in microfluidic channels,” *Opt. Lett.*, vol. 30, no. 11, pp. 1273–1275, Jun. 2005.

Appendix A

Transfer Matrix Method

The reflection and transmission fields for an incident plane wave on a general multilayer film stack are derived using the transfer matrix method following the theory laid out in Macleod [73].

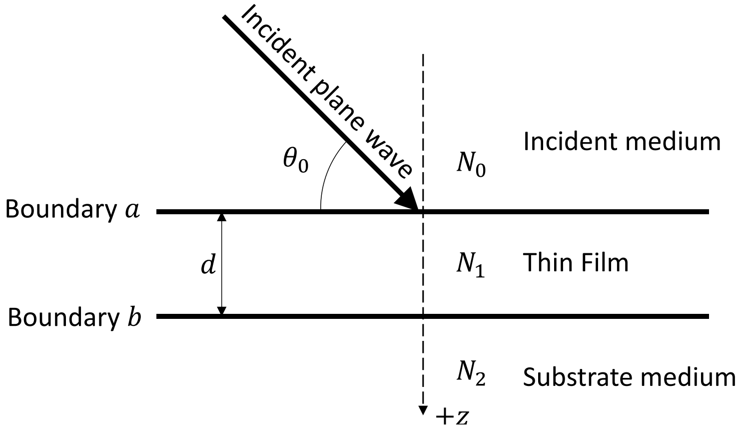

Figure A1: Plane wave incident on a thin film at an incident angle θ_0.

We begin with the analysis of a plane wave of free space wavelength λ that is obliquely incident on a thin film at an angle θ_0 as shown in Figure A1. The tangential components of the magnetic and electric fields within the thin film at the boundary b can be expressed as a sum of both a wave travelling the in positive and negative z directions. Therefore, at interface b the magnitude of the tangential components of the $\boldsymbol{E}$ and $\boldsymbol{H}$ fields are

$$\begin{aligned} E_b &= E_{1b}^{+} + E_{1b}^{-} \\ H_b &= \eta_1 E_{1b}^{+} - \eta_1 E_{1b}^{-} \end{aligned} \tag{A.1}$$

Where η_1 the tilted admittance of the thin film layer is defined by $\eta_1 = n_1\sqrt{\frac{\epsilon_0}{\mu_0}}\cos\theta_1$ and $\eta_{1_p} = \frac{n_1\sqrt{\frac{\epsilon_0}{\mu_0}}}{\cos\theta_1}$, for s and p polarizations, and E_b and H_b represent the resulting fields. Rearranging we obtain:

$$\begin{aligned}
E_{1b}^{+} &= \frac{1}{2}\left(\frac{H_b}{\eta_1} + E_b\right)\\
E_{1b}^{-} &= \frac{1}{2}\left(-\frac{H_b}{\eta_1} + E_b\right)\\
H_{1b}^{+} &= \eta_1 E_{1b}^{+} = \frac{1}{2}\left(\frac{H_b}{\eta_1} + E_b\right)\\
H_{1b}^{-} &= \eta_1 E_{1b}^{-} = \frac{1}{2}\left(-\frac{H_b}{\eta_1} + E_b\right).
\end{aligned} \tag{A.2}$$

The fields at the previous boundary a at the same moment in time and the same x and y coordinates can be determined by computing the phase shift along the z-axis from 0 to $-d$. The phase factor of the positive going wave will be multiplied by $e^{i\delta}$ where:

$$\delta = \frac{2\pi N_1 d \cos\theta_1}{\lambda}. \tag{A.3}$$

Therefore, the fields at the boundary a are defined by:

$$\begin{aligned}
E_{1a}^{+} &= E_{1b}^{+} e^{i\delta} = \frac{1}{2}\left(\frac{H_b}{\eta_1} + E_b\right) e^{i\delta}\\
E_{1a}^{-} &= E_{1be^{i\delta}}^{-} = \frac{1}{2}\left(-\frac{H_b}{\eta_1} + E_b\right) e^{i\delta}\\
H_{1a}^{+} &= H_{1b}^{+} = \frac{1}{2}\left(\frac{H_b}{\eta_1} + E_b\right) e^{i\delta}\\
H_{1a}^{-} &= H_{1b}^{-} = \frac{1}{2}\left(-\frac{H_b}{\eta_1} + E_b\right) e^{i\delta}.
\end{aligned} \tag{A.4}$$

The full field at the boundary a in terms of the fields at boundary b can now be expressed as:

$$\begin{aligned}
E_a &= E_{1a}^{+} + E_{1a}^{-}\\
&= \mathrm{E_b} \frac{\left(e^{i\delta} + e^{-i\delta}\right)}{2} + \mathrm{H_b} \frac{\left(e^{i\delta} - e^{-i\delta}\right)}{2\eta_1}\\
&= E_b \cos\delta + H_b \frac{i \sin\delta}{\eta_1}
\end{aligned} \tag{A.5}$$

$$\begin{aligned}
H_a &= H_{1a}^{+} + H_{1a}^{-}\\
&= \mathrm{E_b}\eta_1 \frac{\left(e^{i\delta} - e^{-i\delta}\right)}{2} + \mathrm{H_b} \frac{\left(e^{i\delta} + e^{-i\delta}\right)}{2}\\
&= E_b i\eta_1 \sin\delta + H_b \cos\delta\,.
\end{aligned} \tag{A.6}$$

The above equations written in matrix form become:

$$\begin{bmatrix} E_a \\ H_a \end{bmatrix} = \begin{bmatrix} \cos\delta & \dfrac{i\sin\delta}{\eta_1} \\ i\eta_1 \sin\delta & \cos\delta \end{bmatrix} \begin{bmatrix} E_b \\ H_b \end{bmatrix}. \qquad \text{(A.7)}$$

The 2×2 matrix is known as the characteristic matrix of the thin film. The optical admittance of the thin film assembly is defined as:

$$Y = \frac{H_a}{E_a}. \qquad \text{(A.8)}$$

Therefore the reflection R of a simple interface medium of admittance η_0 and a medium of admittance Y is:

$$R = \left(\frac{\eta_0 - Y}{\eta_0 + Y}\right)\left(\frac{\eta_0 - Y}{\eta_0 + Y}\right)^* . \qquad \text{(A.9)}$$

Where $*$ is the complex conjugate. Normalizing Eq.(A.7) by dividing by E_b we obtain

$$\begin{bmatrix} E_a/E_b \\ H_a/E_b \end{bmatrix} = \begin{bmatrix} \mathrm{B} \\ \mathrm{C} \end{bmatrix} = \begin{bmatrix} \cos\delta & \dfrac{i\sin\delta}{\eta_1} \\ i\eta_1 \sin\delta & \cos\delta \end{bmatrix} \begin{bmatrix} 1 \\ \eta_2 \end{bmatrix}. \qquad \text{(A.10)}$$

We can now define

$$Y = \frac{H_a}{E_a} = \frac{\mathrm{C}}{\mathrm{B}} = \frac{\eta_2 \cos\delta + i\eta_1 \sin\delta}{\cos\delta + i(\eta_2/\eta_1)\sin\delta}. \qquad \text{(A.11)}$$

Thus the reflection of the thin film assembly can be calculated using Eq.(A9) where

$$\begin{bmatrix} \mathrm{B} \\ \mathrm{C} \end{bmatrix} \qquad \text{(A.12)}$$

is the characteristic matrix of the assembly.

By adding another thin film to the single film of Figure A1 as seen in Figure A2, we can find the new reflection coefficient which will allow us to immediately see how to extend the analysis to the general case of an assembly of q layers.

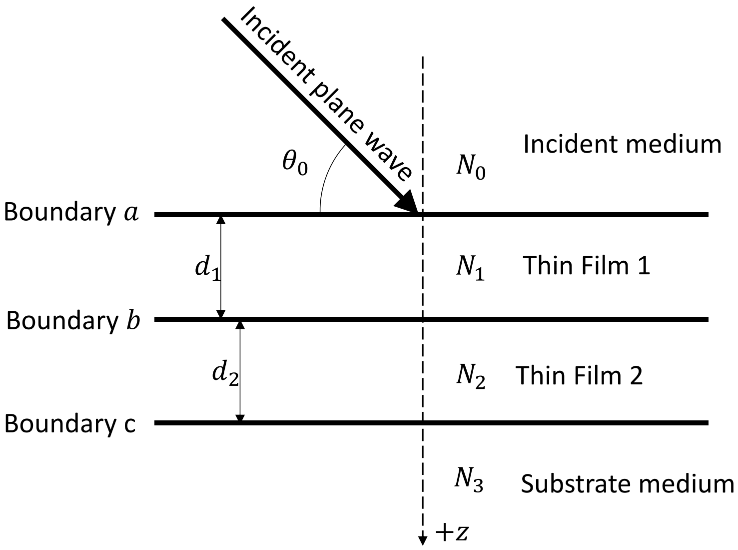

Figure A2: Schematic and notation for the two layer assembly

The characteristic matrix of thin film 2 is:

$$\begin{bmatrix} \cos\delta_2 & \dfrac{i\sin\delta_2}{\eta_2} \\ i\eta_2\sin\delta_2 & \cos\delta_2 \end{bmatrix}, \tag{A.13}$$

so that

$$\begin{bmatrix} E_b \\ H_b \end{bmatrix} = \begin{bmatrix} \cos\delta_2 & \dfrac{i\sin\delta_2}{\eta_2} \\ i\eta_2\sin\delta_2 & \cos\delta_2 \end{bmatrix} \begin{bmatrix} E_c \\ H_c \end{bmatrix}. \tag{A.14}$$

Combining with the previous definition of the fields at boundary a we have:

$$\begin{bmatrix} E_a \\ H_a \end{bmatrix} = \begin{bmatrix} \cos\delta_1 & \dfrac{i\sin\delta_1}{\eta_1} \\ i\eta_1\sin\delta_1 & \cos\delta_1 \end{bmatrix} \begin{bmatrix} \cos\delta_2 & \dfrac{i\sin\delta_2}{\eta_2} \\ i\eta_2\sin\delta_2 & \cos\delta_2 \end{bmatrix} \begin{bmatrix} E_c \\ H_c \end{bmatrix}. \tag{A.15}$$

The characteristic matrix of the assembly of Figure A.2 is the defined by:

$$\begin{bmatrix} \mathrm{B} \\ \mathrm{C} \end{bmatrix} = \begin{bmatrix} \cos\delta_1 & \dfrac{i\sin\delta_1}{\eta_1} \\ i\eta_1\sin\delta_1 & \cos\delta_1 \end{bmatrix} \begin{bmatrix} \cos\delta_2 & \dfrac{i\sin\delta_2}{\eta_2} \\ i\eta_2\sin\delta_2 & \cos\delta_2 \end{bmatrix} \begin{bmatrix} 1 \\ \eta_3 \end{bmatrix}. \tag{A.16}$$

The optical admittance of the assembly is as before, $C/B,$ and the reflectance is, as in Eq. (A.9)

$$R = \left(\frac{B\eta_0 - C}{B\eta_0 + C}\right)\left(\frac{B\eta_0 - C}{B\eta_0 + C}\right)^*.$$

This result can be immediately extended to the general case, so that the characteristic matrix of the assembly of q layers becomes:

$$\begin{bmatrix} \mathrm{B} \\ \mathrm{C} \end{bmatrix} = \left\{ \prod_{r=1}^{q} \begin{bmatrix} \cos\delta_\mathrm{r} & \dfrac{i\sin\delta_r}{\eta_r} \\ i\eta_r\sin\delta_\mathrm{r} & \cos\delta_r \end{bmatrix} \right\} \begin{bmatrix} 1 \\ \eta_m \end{bmatrix}. \tag{A.17}$$

where the suffix m denotes the substrate media and the values of θ_r can be found from Snell's Law:

$$N_0\sin\theta_0 = N_r\sin\theta_r = N_m\sin\theta_m. \tag{A.18}$$

Appendix B
Sensitivity Analysis

In this appendix, an analysis is performed to determine the theoretical sensitivity of the FOEWS under measurement from an 18 bit analog to digital converter. The following analysis assumes a noiseless optical signal from the FOEWS. The circuit diagram shown in Figure B.1 outlines the readout circuit design which will be used to analyze the output optical signal from the FOEWS.

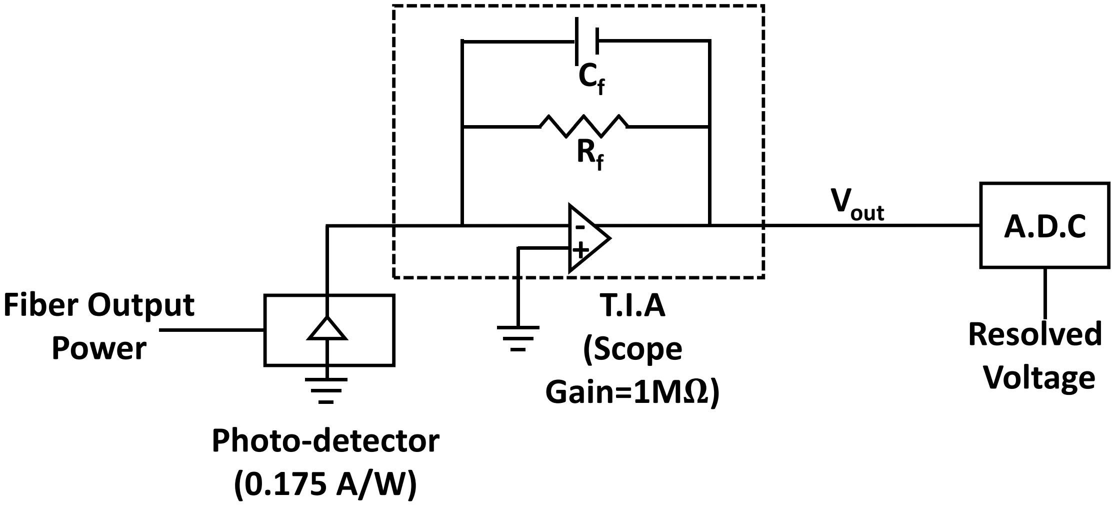

Figure B.67: Circuit diagram of the FOEWS readout system.

The analysis of the output optical signal from the FOEWS is read by a photo-detector obtained from Thorlabs, model DET 10C, which has a stated responsivity of 0.175 A/W. The output current of the photo-detector is then read using an Agilent Oscilloscope, model A3631A, which acts as a transimpedance amplifier with gain of 1 MΩ. The resulting output voltage V_{out} is then sent to a high quality 18-bit analog to digital controller where the signal can be read by computer.

Experiments conducted in Chapter 4, determined the output voltage from the oscilloscope resulting from the output transmitted power from the FOEWS exposed to an external environment of refractive index 1.33 to be 400 mV. Thus, the normalized transmission response curves of the FOEWS shown in Figure 30, are assumed to have a gain of 400 mV resulting from the photo-detector and oscilloscope elements. Therefore, the predicted voltage response of the FOEWS exposed to analyte index of refractions ranging from 1.42 to 1.6 with cladding thicknesses from 0.1 to 1.4 µm are described by the graphs of Figure B.2.

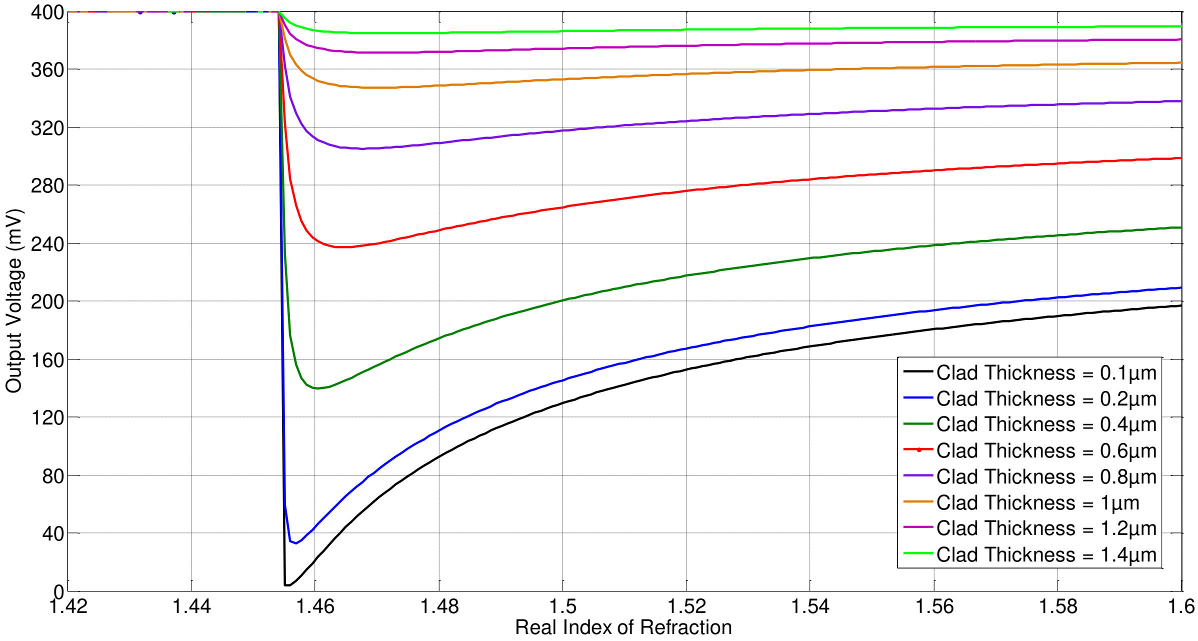

Figure B.68: Predicted voltage output of the FOEWS for cladding thicknesses from 0.1 to 1.4 µm with an empirically determined gain of 400 mV.

The sensitivity of the FOEWS as determined by the output voltage response curves of Figure B.2, can be determined using the definition of sensitivity given by:

$$S = \frac{dV_{out}}{dn}. \qquad \text{(B.1)}$$

Using the definition of sensitivity of Eq. B.1 and applying it to the predicted output voltage curves of Figure B.2 to sensitivity curves of the FOEWS are shown in Figure B.3.

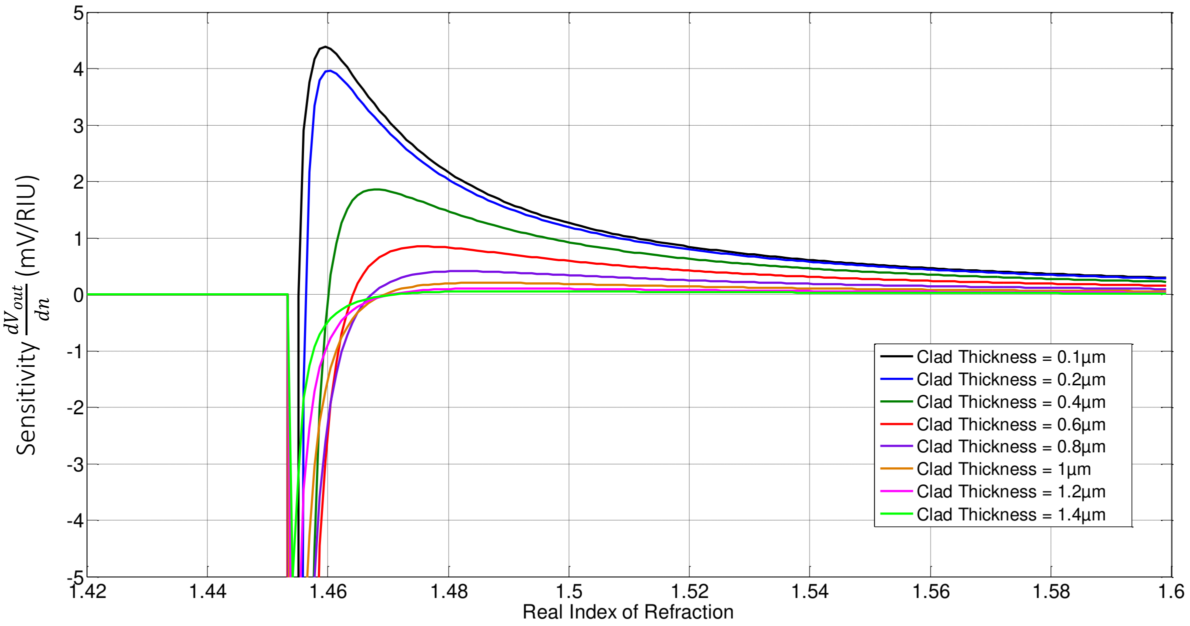

Figure B.69: Predicted sensitivity of the FOEWS output voltage as measured at the output of the oscilloscope shown in Figure B.1.

From the predicted sensitivity curves of Figure B.3, the sensitivity of the FOEWS regardless of cladding thickness occurs at the index of refraction corresponding to the fiber core index of 1.451 due to the non-smooth behavior of the voltage response curve. Due to the asymptotic behavior of the sensitivity near the index of refraction of the core, the bounds on sensitivity are investigated between ± 5 mV/RIU, where RIU are refractive index units.

As shown in Figure B.1, the output voltage from the oscilloscope can be analyzed using an 18 bit analog to digital controller (ADC) from Microchip Technology Inc. model MCP3421. The ADC is programed for a voltage input range of ± 2.048 V so that theoretical minimum resolvable voltage is given by:

$$\Delta V_{max} = \frac{2.048}{2^{17}} = 1.562 \text{ e-3 mV.} \qquad \text{(B.2)}$$

The resulting minimum detectable refractive index change using the ADC, photo detector and transimpedance amplifier configuration of Figure B.1 can be found by dividing the minimum resolvable voltage of Eq. B.2 by the predicted sensitivity curve of Figure B.3. For clarity, only the refractive index sensitivity for a FOEWS of cladding thickness 0.1 μm is shown in Figure B.4 for refractive indices from 1.46 to 1.6.

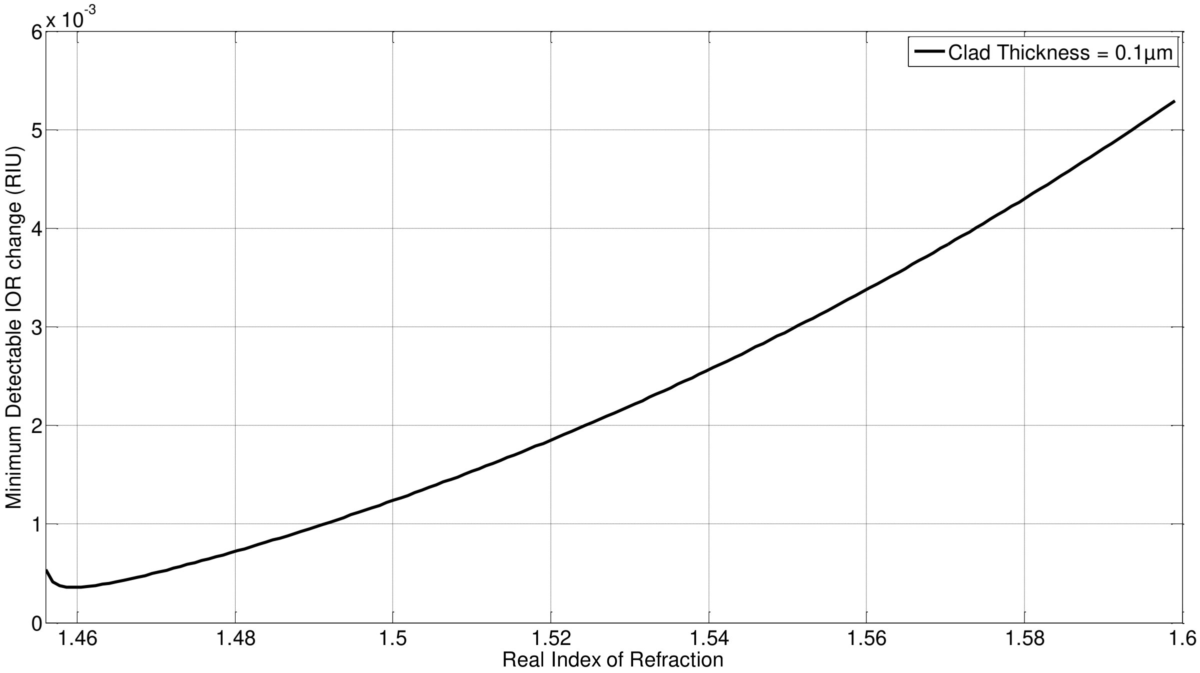

Figure B.70: Minimum detectible index of refraction change for a FOEWS read by the circuit of Figure B.1 for a FOEWS of cladding thickness 0.1 μm. The highest sensitivity is 3.56e-4 RIU in around an analyte IOR value of 1.46 and an average sensitivity of 2.2e-3 over the entire range from 1.46 to 1.6.

The predicted detectible index of refraction change shown in Figure B.4 varies from 3.56e-4 to 5.5e-3 RIU in the sample range of 1.46 to 1.6. In Chapter 5, the response behavior of the FOEWS under exposure to an assumed battery electrode changing index of refraction from that of pure graphite to pure LiC_6. The predicted output voltage of a FOEWS with cladding thickness of 0.1 μm is given in Figure B.5. below.

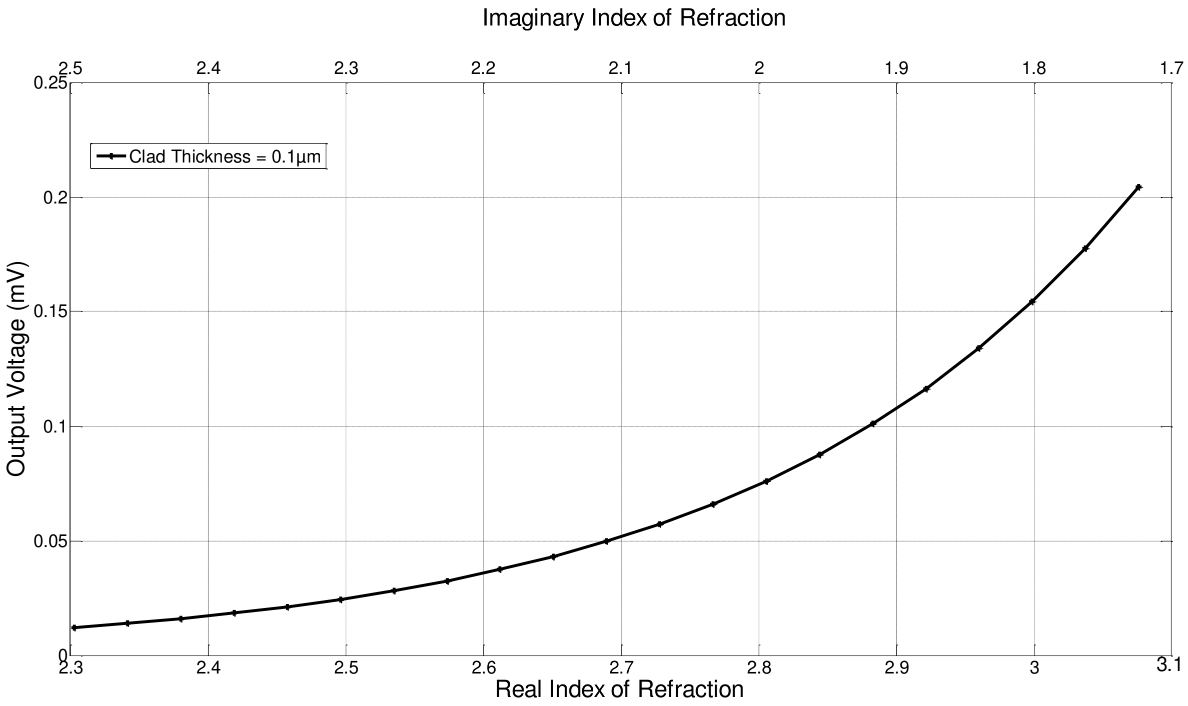

Figure B.71: Predicted voltage output of the FOEWS for a cladding thickness of 0.1 µm with an empirically determined gain of 400 mV subject to a change in analyte refractive index equal to that of the battery electrode outlined in Chapter 5.

Similar to the derivation of Figure B.4, the resulting minimum detectable refractive index change using the ADC, photo detector and transimpedance amplifier configuration of Figure B.1 can be found by dividing the minimum resolvable voltage of Eq. B.2 by the predicted sensitivity curve of corresponding to Figure B.5. The resulting curve of minimum detectible index of refraction change in the range of the battery electrode is shown in Figure B.6.

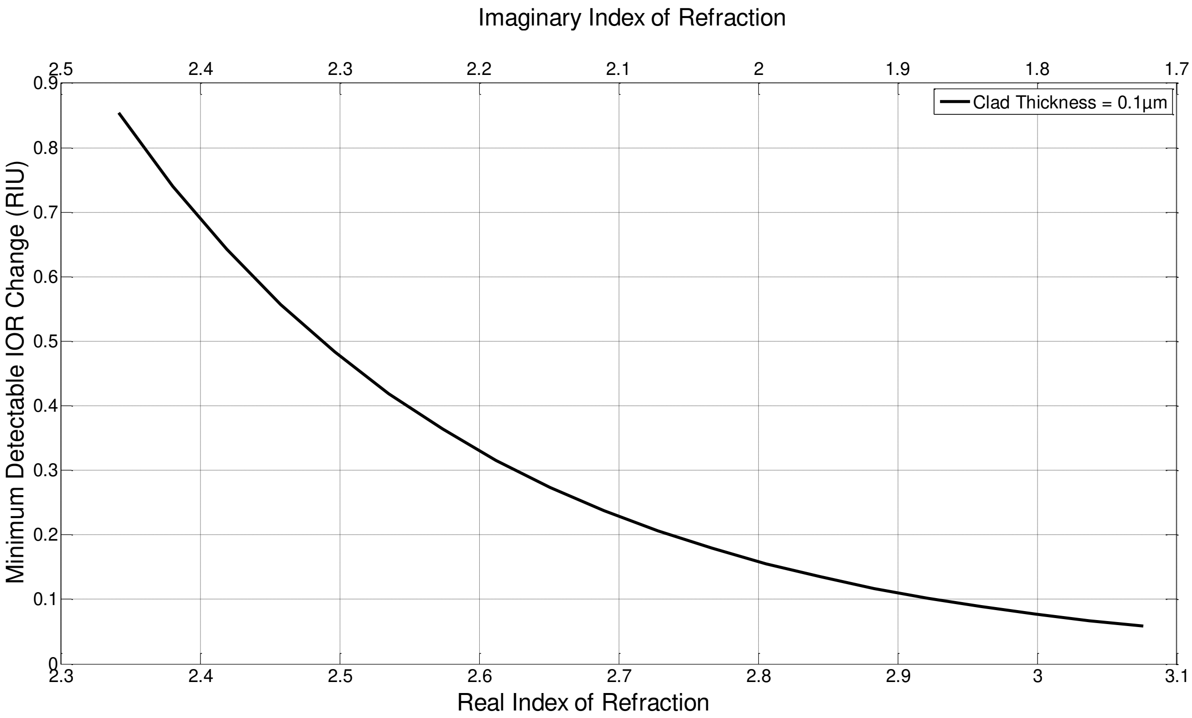

Figure B.72: Minimum detectible index of refraction change for a FOEWS read by the circuit of Figure B.1 for a FOEWS of cladding thickness 0.1 µm in the range of the battery electrode. The highest sensitivity is 5.83e-2 RIU in around an analyte IOR value of $3.07 + i1.7$.

From the graph in Figure B.6 the minimum detectible index of refraction change for a FOEWS of cladding thickness 0.1 µm in exposed to the index of refraction range of the battery electrode is 5.83e-2 RIU.

The sensitivity of in the range of 1.46 to 1.6 presented in Figure B.3 is comparable to the calculated sensitivity of the FOEWS considered by several other authors of fiber optic refractive index sensors. Table B.1 below summarizes the reported sensitivities.

Table B.1: Summary of several reported sensitivities of fiber optic intensity based refractive index sensors.

Reference	Sensitivity [mW/RIU]	Minimum Detectible Index of Refraction Change [RIU]	Refractive Index Range
Zhong et al. (2013) [67]	-6.7 to -11.5	Not reported	1.332 to 1.353
Chen et al. (2010) [102]	Not reported	1.27e-3 to 3.13e-4	1.333 to 1.403
Polynkin et al.(2005) [103]	Not reported	5e-4	1.31 to 1.44
Nath et al. (2008) [10]	Not reported	2e-3	1.32 to 1.42
This Work	4 to 0.2	3.56e-4 to 5.5e-3	1.46 to 1.6

The minimum detectable refractive index change for the system outlined in Figure B.1, can be improved by modifying and calibrating the elements of the system. By cascading a secondary transimpedance amplifier onto the oscilloscope signal, the output voltage of gain can be increased in order to better fill the voltage range of the ADC. Additionally, a stronger LED can be used to illuminate the FOEWS increasing the signal output onto the photo detector. In respect to the sensitivity of the FOEWS in the range of the battery electrode refractive indices, the voltage range caused by the index of refraction change from $2.342 + i2.45$ to $3.07 + i1.7$, would require an additional gain in order to fill the input range of the ADC.

Appendix C
Model Code

The full Matlab® code developed in this thesis is available by email request to:

Jeremy R. Godin
jrgodin@uwaterloo.ca

or

Patricia Nieva
pnieva@uwaterloo.ca